Evaluation of the atmospheric performance of HadGAM/GEM1

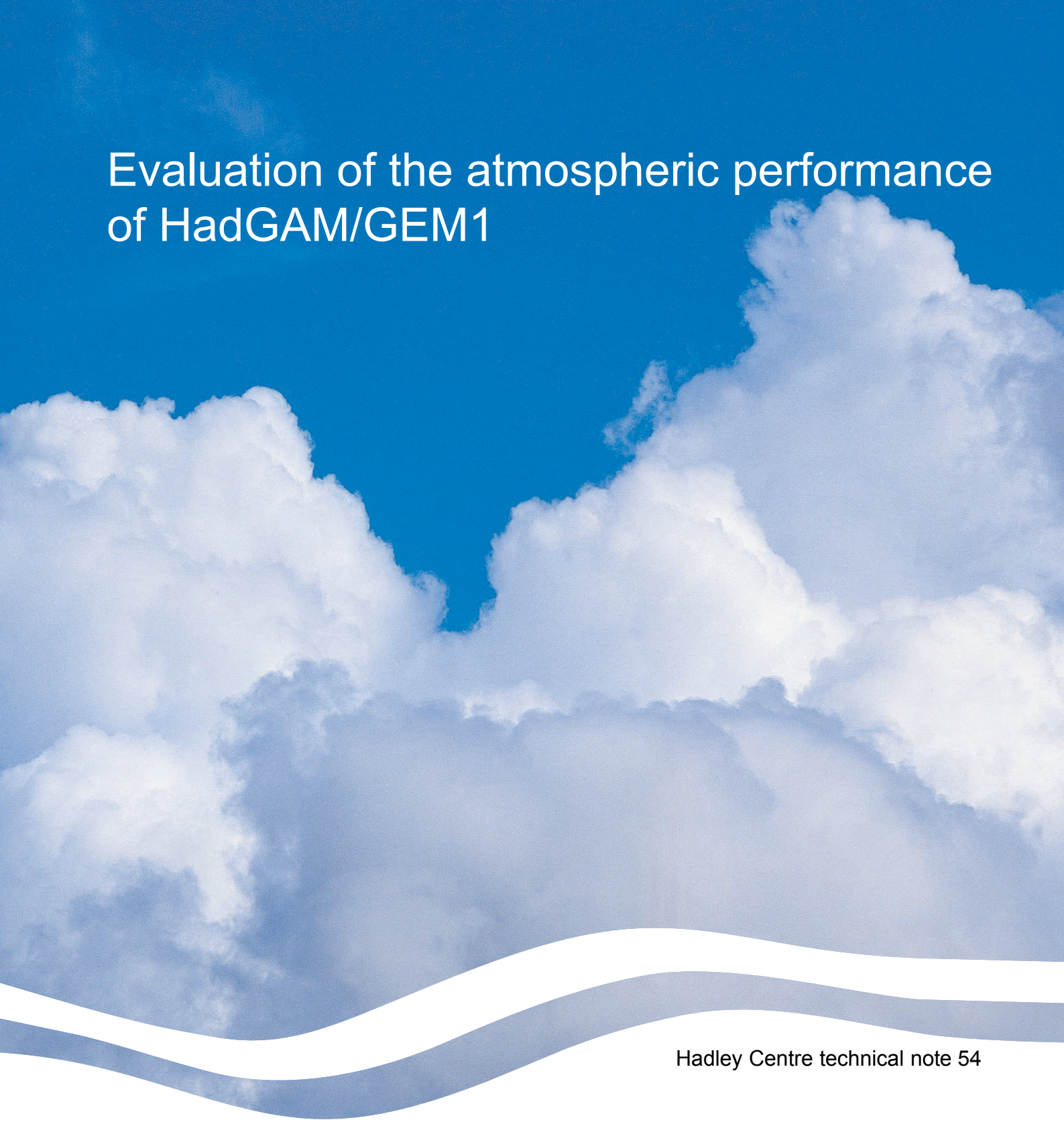

Hadley Centre technical note 54

Gill Martin, Chris Dearden, Christina Greeves, Tim Hinton, Pete Inness, Paul James, Vicky Pope, Mark Ringer, Julia Slingo, Rachel Stratton and Gui-Ying Yang

23 September 2004

Met Office

Evaluation of the atmospheric performance of HadGAM/GEM1

Gill Martin[1], Chris Dearden[1], Christina Greeves[1], Tim Hinton[1], Pete Inness[2], Paul James[1], Vicky Pope[1], Mark Ringer[1], Julia Slingo[2], Rachel Stratton[1] and Gui-Ying Yang[2]

[1]Hadley Centre for Climate Prediction and Research,
Met Office, Fitzroy Road, Exeter EX1 3PB
[2]Centre for Global Atmospheric Modelling, University of Reading, Earley Gate, Reading

Abstract

The atmospheric component of the new Hadley Centre climate model, HadGEM1, has been evaluated against its predecessor, HadAM/CM3, and observed climatologies. The model performs well, and in many aspects it improves upon the previous version. The improvements can be attributed to the increased horizontal and vertical resolution, the new dynamics and the improvements to the physical parametrisations and how they are coupled with the dynamics. Coupling the atmosphere model to an ocean model has a small detrimental impact on the precipitation and mean sea level pressure, but has a broadly neutral impact on the other climatological fields. The impacts on precipitation are related to the development of SST errors in the tropics, particularly around the equatorial Pacific and the maritime continent. The tropics remain an area of concern in the new model.

Several aspects of variability have been assessed. Intraseasonal variability of convection near the equator is generally stronger and closer to observations in HadGAM1/GEM1. However, as in HadAM3, there is limited convective variance coincident with the equatorial wave modes. At N48 resolution, there is less transient eddy activity in the new model. The storm tracks are weaker (except at the surface) and the blocking frequency in the Atlantic region is reduced. This is due to the change to semi-Lagrangian dynamics, which are not designed to work well at such poor resolution. At N96 the transient eddy activity is increased and the storm tracks strengthened. Many other aspects of the simulation are also improved with increased resolution. Simulation of the Madden-Julian Oscillation is improved in the coupled model: HadGEM1 produces several eastward-propagating events with comparable magnitude to observations. However, as in HadCM3, there is limited extent of eastward propagation due to a systematic error in low-level winds along the equator.

There are considerable improvements in the representation of cloud in HadGAM1 compared with HadAM3. Perhaps the most significant development is the much greater consistency between the cloud and radiation budget fields in HadGAM1 – comparisons with satellite observations demonstrate that the developments included in the new model lead to a much better representation of the different ISCCP cloud types, while at the same time providing a generally more reliable simulation of the top-of-atmosphere radiation budget and the cloud radiative forcing.

Contents

1. Introduction

The development of models used for climate predictions carries with it the need for continuing evaluation of all aspects of the climate simulation (mean climate, spatial and temporal variability, extreme events), along with the investigation of any systematic errors. The atmospheric component, HadGAM1, of the new climate model includes semi-Lagrangian dynamics and increased model horizontal and vertical resolution, combined with an almost completely new suite of physical parametrisations, and includes additional processes such as the sulphur cycle and cloud aerosol effects. The ocean model includes several new parametrisation and its resolution is improved, especially around the equator (see Johns et al. (2004) for details). Thus, both the coupled model and its atmosphere-only version, HadGAM1, are very different from the previous versions, HadCM3 and HadAM3, and they represent the state-of-the-art in general circulation modelling.

The previous model version, HadAM/CM3, used a resolution typically adopted in other climate models, namely 2.5 degrees latitude by 3.75 degrees longitude (termed "N48"). HadGAM/GEM1 uses double this resolution in the atmosphere (termed "N96"), ie 1.25 degrees latitude by 1.875 degrees longitude. The higher resolution has been shown in previous model versions to improve some aspects of the model's climatology and its variability by resolving smaller-scale features and improving the representation of dynamics (Pope and Stratton, 2002). However, it can also reveal compensating errors in the model and may lead to degradation in some model fields while others improve. It is, therefore, important to evaluate the benefits of higher resolution against the increased cost of the simulations. In this study, therefore, we compare HadGAM1 runs at both resolutions with those from HadAM3.

The new model runs on a Charney-Phillips vertical grid and the vertical resolution is twice that of HadAM3/CM3. The impact of the increased vertical resolution alone is not investigated here. Experience with past versions of the climate model (e.g. Pope et al. 1999, Martin et al. 2000, Bushell and Martin, 1999) has shown that the model physics is particularly sensitive to the vertical resolution, to the extent that some schemes (e.g. boundary layer, convection, cloud) behave very differently at different resolution. This is particularly the case for changes in the lower tropospheric resolution. Martin et al. (2000) showed that increasing the resolution in the lowest 2.5 km of the atmosphere resulted in major changes to the precipitation distribution. Large decreases in equatorial precipitation, particularly over Indonesia, and increases in precipitation to the north and south, especially over the Arabian Sea, South China Sea and western Pacific Ocean, resulted from the same increase in lower tropospheric resolution as is made between HadAM3 and HadGAM1. Bushell and Martin (1999) showed that the representation of the amount and vertical distribution of stratocumulus cloud was improved with increased resolution in the lower troposphere. However, both of those studies suggested that the changes observed were a result of an underlying sensitivity to vertical resolution in model interactions between boundary layer and convective processes. Although many of the changes to the boundary layer and convection schemes in HadGAM1 are designed to address such sensitivities, the nature of the new schemes is such that a certain minimum level of resolution is required, higher than that of HadAM3. Thus,

we consider the increased vertical resolution in HadGAM/GEM1 as part of the change in the model formulation.

In this report we evaluate a range of different aspects of the simulation as follows:

- zonal mean climatologies of temperature, moisture, winds
- climatologies of surface variables (pressure, temperature, precipitation)
- radiation budget and cloud distributions
- modes of variability (storm tracks, blocking, European weather regimes, tropical intraseasonal variability)

This document provides an overall evaluation of the HadGAM/GEM1 atmosphere. Where appropriate, comparisons are made with the previous model version, HadAM/CM3. Other relevant documents include Pope et al. (2000), Pope et al (2001), Pope and Stratton (2002) and Martin et al. (2004). A companion report (Johns et al., 2004) focuses on aspects of the coupled model such as sea surface temperatures and salinity, ocean circulation, heat and freshwater transports, sea-ice distributions, El Nino-Southern Oscillation, cloud-climate interactions and climate sensitivity, as well as considering the overall skill of the model against HadCM3.

2. Experimental details

The evaluation of the atmosphere component of HadGEM1 is made mainly using atmosphere-only (HadGAM1) runs forced by observed sea surface temperatures (SSTs) and sea-ice concentrations. This eliminates feedbacks from any developing SST errors in the coupled model, but also prevents any coupled atmosphere-ocean processes from operating. It is, therefore, important to examine the performance of the atmosphere in the coupled model in comparison with the atmosphere-only runs.

HadGAM1 runs at N48 and N96 resolution are forced with SSTs and sea-ice from the second Atmosphere Model Intercomparison Project (AMIP-II) from 1979-1996. Comparisons are made with the ECMWF (European Centre for Medium Range Weather Forecasts) re-analysis climatology (ERA; Gibson et al., 1997) for the same period, and also with similar runs of the previous model versions, HadAM3.

The climatology of the HadGAM1 atmosphere at N96 is also compared with that from HadGEM1 at N96. This allows us to identify the impacts and feedbacks of coupled processes and developing sea surface temperature errors on the atmospheric performance. Reference is made to similar comparisons of HadAM3 and HadCM3 (but at N48 resolution).

The differences between HadGAM/GEM1 and HadAM/CM3 are too numerous to describe in detail. They are summarised in Table 1. The scope of the changes made to the model is so great that it is, in most cases, impossible to analyse the direct impact of each individual change on the model results. Instead, we evaluate the model as a whole against its predecessor and the observations. However, in some cases, sensitivity tests have allowed us to attribute certain improvements or detriments to (a) particular model change(s).

	HadAM3/CM3	HadGAM1/GEM1
Atmospheric grid	Arakawa-B grid	Arakawa-C grid
Hydrostatic	yes	no
Vertical resolution (atmosphere)	19 levels; hybrid pressure; Lorenz grid	38 levels; hybrid height; terrain-following near bottom boundary; Charney-Phillips grid
Physics-dynamics coupling	Sequential	Parallel-split (slow processes), sequential-split (fast processes). (Dubal et al., 2004)
Dynamics	Eulerian advection, split-explicit time integration (Cullen 1993)	Semi-Lagrangian advection, conservative monotone treatment of tracers; semi-implicit time integration (Staniforth et al., 2003, Davies et al., 2004)
Radiation	Edwards and Slingo (1996); Cusack et al. (1999a)	Edwards and Slingo (1996); Cusack et al. (1999a)
Boundary layer	Local Richardson number mixing scheme (Smith 1990,1993)	Non-local mixing scheme for unstable BLs (Lock et al. 2000). Local Richardson number scheme for stable layers (Smith 1990, 1993)
Microphysics	Senior and Mitchell (1993); evaporation of precipitation as in Gregory (1995).	Mixed phase scheme including prognostic ice content; solves physical equations for microphysical processes using particle size information (Wilson and Ballard,1999)
Convection	Mass flux scheme (Gregory and Rowntree,1990); convective downdraughts (Gregory and Allen, 1991); convective momentum transport (Gregory et al., 1997)	Revised scheme including diagnosed deep and shallow convection; new thermodynamic closures at lifting condensation level; new CMT parametrisation based on flux-gradient relationships; parametrised entrainment /detrainment rates for shallow convection. Based on ideas in Grant and Brown (1999), Grant (2001). Convective anvil scheme (Gregory, 1999)
Gravity wave drag	Gregory et al. (1998)	GWD scheme with low-level flow blocking Webster et al. (2003)
Orography	Derived from US Navy 10' dataset	Derived from GLOBE dataset at 1' resolution
Hydrology	MOSES-I (Cox et al., 1999)	MOSES-II (Essery et al., 2001); 9 surface tile types plus coastal tiling; seasonally-varying vegetation (Lawrence and Slingo, 2004)
Clouds	Smith (1990); prescribed critical relative humidity for cloud formation (RH-crit)	Smith (1990); parametrised RH-crit (Cusack et al., 1999b); vertical gradient area cloud scheme (Smith et al., 1999)
River routing	Simple basin aggregate output instantaneously to ocean	Embedded 1x1 degree river transport/hydrology sub-model (Oki and Sud, 1998)
Sulphur cycle and aerosols	prescribed	Interactive; sulphate and sea-salt aerosol schemes, DMS, biomass burning aerosols, black carbon; direct/indirect radiative forcing (Jones et al., 2001; Roberts and Jones, 2004; Jones and Roberts 2004; Woodage et al., 2003)
Ocean horizontal resolution	1.25 by 1.25 degrees	1 x 1 degree except in tropics where increases smoothly to 1/3 degree in latitude at equator
Ocean vertical resolution	20 levels	40 levels
Ocean model	Gordon et al. (2000)	HadGOM1 (Johns et al., 2004): EVP sea ice dynamics; multiple-category ice thickness distribution; linear free-surface scheme; high resolution coast/bathymetry; 4^{th}-order advection of active tracers

Table 1: Summary of HadAM/CM3 and HadGAM/GEM1 configurations

3. Taylor Diagrams

Taylor diagrams (Gates et al 1999, Taylor 2001) compare the global distribution of multi-annual mean fields from the models with corresponding monthly means from observations or analyses. The distance from the origin is the standard deviation of the field normalised by the standard deviation of the observationally-based climatology, i.e. if the standard deviation of the model is the same as that of the climatology then the radius is 1. The root mean square difference (model minus climatology) minus the difference in the global mean averages is the distance from the reference point to the plotted point. The correlation between the model and the climatology is the cosine of the polar angle, i.e. if the correlation between the model and the climatology is 1 then the point will lie on the horizontal axis. In the plots which follow, the results for all four seasons are combined, so that any errors in the seasonal variation are also included.

Figure 1(a) shows the errors in the thermodynamic variables for HadGAM1 and HadAM3. In general, the new model improves on the previous version at upper levels and is similar or slightly worse at mid/low levels. The improvements at upper levels can be attributed to the increased upper-tropospheric vertical resolution, the new dynamics and changes in the microphysical parametrisation (discussed further in the next section). Figure 1(b) shows that the zonal wind errors are similar in the two models but the meridional winds are worse in HadGAM1. Figure 1(c) shows that the impact of the new model on radiative parameters is broadly neutral, with the exception of detriments to the longwave cloud forcing and outgoing longwave radiation (OLR). These are associated with a worsening of the precipitation climatology. Figure 1(d) shows that the transient eddy fields are generally worse in HadGAM1 at N48 resolution. This is because the semi-Lagrangian dynamics was not designed for such poor horizontal resolution. This points is discussed further in Sections 4 and 6.

Figure 2 shows similar diagrams for HadGAM1 at N48 and N96 resolution, and also for HadGEM1 (N96). The main impact of increasing resolution is on the transients (Fig. 2(d)), although there are also improvements in nearly all of the other fields, particularly the mid- and lower-tropospheric temperatures and humidities and the meridional winds. Coupling the atmosphere model to the ocean model has a small detrimental impact on the precipitation and OLR, mid- to lower-tropospheric humidities and meridional winds but has a broadly neutral impact on the other fields. Some of these changes are related to the forcing used in the HadGEM1 control run which was appropriate for 1860, and some (e.g. precipitation, OLR, meridional winds) are related to the development of equatorial SST errors (see Section 5).

Comparison of the coupled model HadGEM1 (at N96 resolution) with HadCM3 (N48 resolution) confirms the improvements in upper level temperatures and humidities, while the impact on the low-level temperatures and humidities is broadly neutral (Fig. 3(a)). Precipitation and related cloud fields remain worse in the new model, but total cloud amount is improved (Fig. 3(b)). The transients are also improved in new (higher resolution) model version (not shown). Overall, the impact on the winds is neutral compared with HadCM3 (not shown).

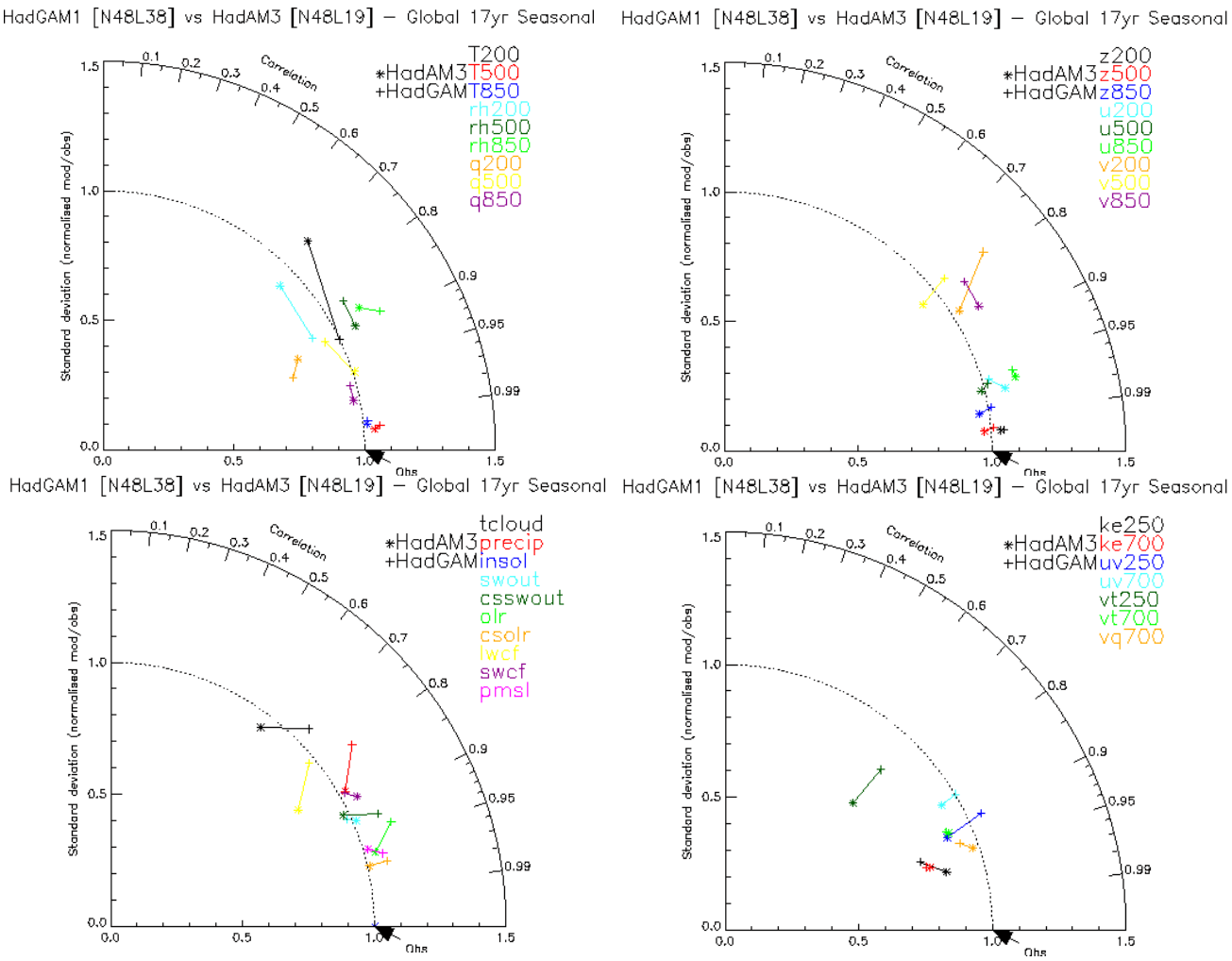

Figure 1: Taylor diagrams (see text) summarising comparison of HadGAM1 and HadAM3 (both at N48 resolution)

Key to Taylor diagrams (Fig.s 1 and 2)

T, temperature; *q,* water vapour; *rh,* relative humidity; *q,* water vapour; *z,* geopotential height; *u,v,* horizontal wind components; *numbers* refer to the pressure level of the field; *tcloud,* total cloud; *precip,* precipitation; *swout,* outgoing shortwave radiation; *csswout,* clear-sky outgoing shortwave radiation; *olr,* outgoing longwave radiation; *csolr,* clear-sky outgoing longwave radiation; *lwcl,* longwave cloud forcing; *swcf,* shortwave cloud forcing; *pmsl,* pressure at mean sea level; *ke,* transient eddy kinetic energy; *uv ,vt, vq,* other transient eddy fields.

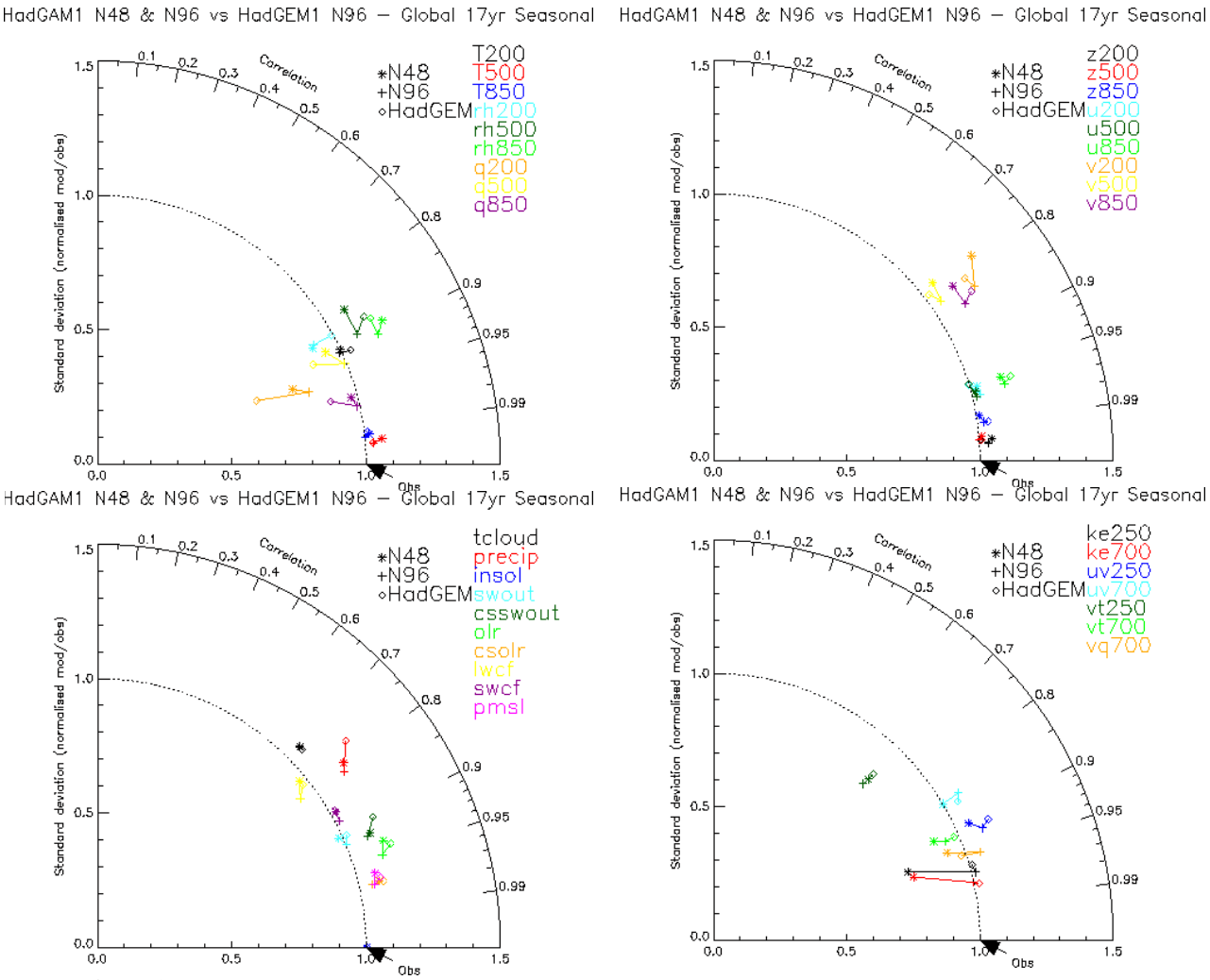

Figure 2: Taylor diagrams comparing HadGAM1 at N96 and N48 resolution with HadGEM1 (N96)

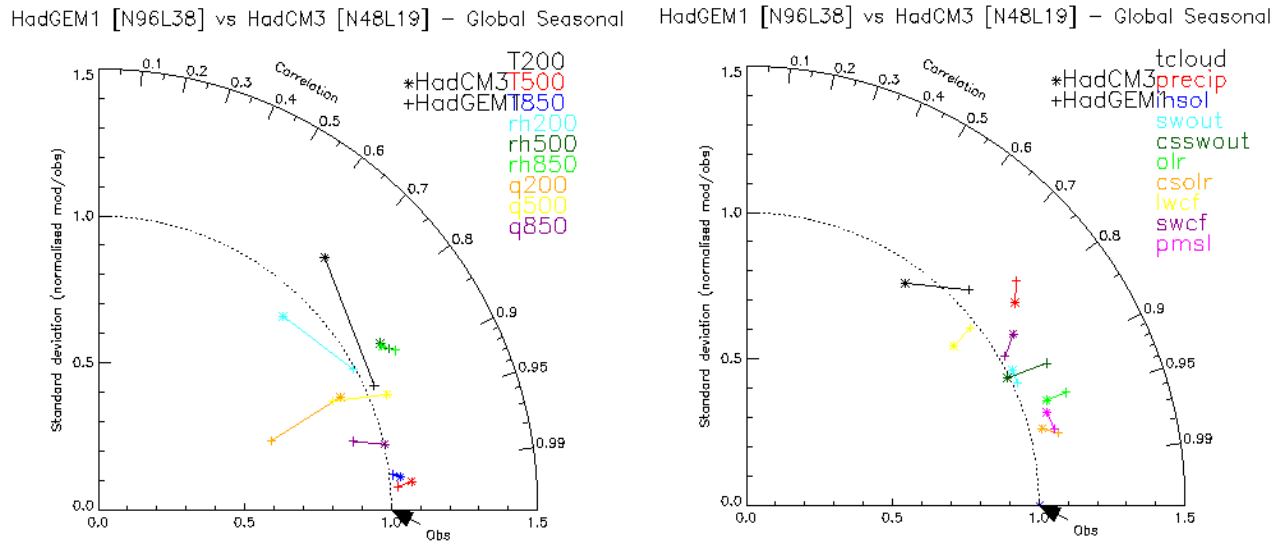

Figure 3: Taylor diagrams comparing HadGEM1 (N96) with HadCM3 (N48)

4. Zonal mean climatologies

4.1 Temperature, humidity and cloud

Figures 3 and 4 show the zonal mean temperature and relative humidity cross sections in December-February (DJF) from HadGAM1 at N48 resolution compared with HadAM3 and ERA. In the previous model version, large cold and moist errors are seen in the upper troposphere, which are associated with incorrect positioning of the tropopause. This error is greatly reduced in HadGAM1, although the basic pattern of errors is similar. The mid-troposphere remains rather cold and the tropical troposphere is now slightly too warm and dry.

The substantial improvement in the upper tropospheric temperatures and moisture in HadGAM1 can be attributed partly to increased vertical resolution around the tropopause (Pope et al., 2001), partly to the more accurate semi-Lagrangian advection scheme and partly to a modification to the microphysics which allows more efficient conversion of vapour to ice, thus restricting the amount of vapour that reaches high levels. In the mid- and lower-troposphere, however, layer cloud water and ice contents are reduced in HadGAM1 compared with HadAM3 (not shown). A new microphysics scheme which includes prognostic ice contents was introduced in HadGAM1. The direct impact of this scheme is to increase the cloud water paths, mainly due (in mid-latitudes) to a decrease in fall speeds and (in convective regions) to the sub-grid-scale model changes. The decreases in cloud water and ice contents seen in HadGAM1 must, therefore, be due to less efficient vertical moisture transport.

There is also evidence of a change in the balance between large-scale and convective cloud in HadGAM1. Layer cloud amounts in the tropical upper troposphere are lower in HadGAM1 than HadAM3, but convective cloud amounts here are much larger (not shown). This is a result of the inclusion of a convective anvil parametrisation in HadGAM1. At lower levels, convective cloud amounts are reduced in the tropics and mid-latitudes, but increased in the sub-tropics where shallow convection dominates. These changes are largely a result of improved diagnosis and treatment of shallow convection in HadGAM1.

Figures 5 and 6 show the impact of increased horizontal resolution on the temperature and relative humidity fields in HadGAM1. There is an overall warming throughout the troposphere but particularly in the southern hemisphere mid- and high-latitudes. This reduces the cold biases seen at N48, although the tropical warm bias is increased. It can also be seen that the subtropical cold/moist bias in the mid-troposphere is reduced in the high resolution run. This is partly associated with changes in the hydrological cycle through the increased transient vertical velocities which promote more rapid condensation and less rapid evaporation of precipitation. It is also partly associated with a poleward movement of the westerly jets (see section 4.2). Both of these effects were seen in HadAM3 (Pope and Stratton, 2002).

The coupled model HadGEM1 (at N96 resolution) shows an overall cooling (and a small overall moistening) of the troposphere which is related to the 1860 forcings used in this control run (not shown). There are also increases in layer cloud amount in the subtropics. These are related to the development of colder SSTs in

these regions (see Johns et al., 2004). Changes in cloud distribution and properties between the different model versions are discussed further in Section 5.3.

4.2 Winds

Figure 7 shows the zonal mean zonal wind cross-section in DJF from HadGAM1 (N48) compared with HadAM3 and ERA. The large westerly bias at upper levels in the southern hemisphere is reduced significantly, and the stratospheric jet in the northern hemisphere has moved poleward, in better agreement with ERA. The easterly bias around the tropical tropopause is also reduced. These improvements are in the same direction as those seen between HadAM2b and HadAM3 (Pope and Stratton, 2002), which were there attributed to the inclusion of convective momentum transports. The revisions to the convection scheme in HadGAM1 include a new parametrisation of convective momentum transports based on flux-gradient relationships. Comparisons of HadGAM1 with and without the revised convection scheme suggest that at least some of the additional improvement in the zonal winds in HadGAM1 comes from improving the representation of CMT.

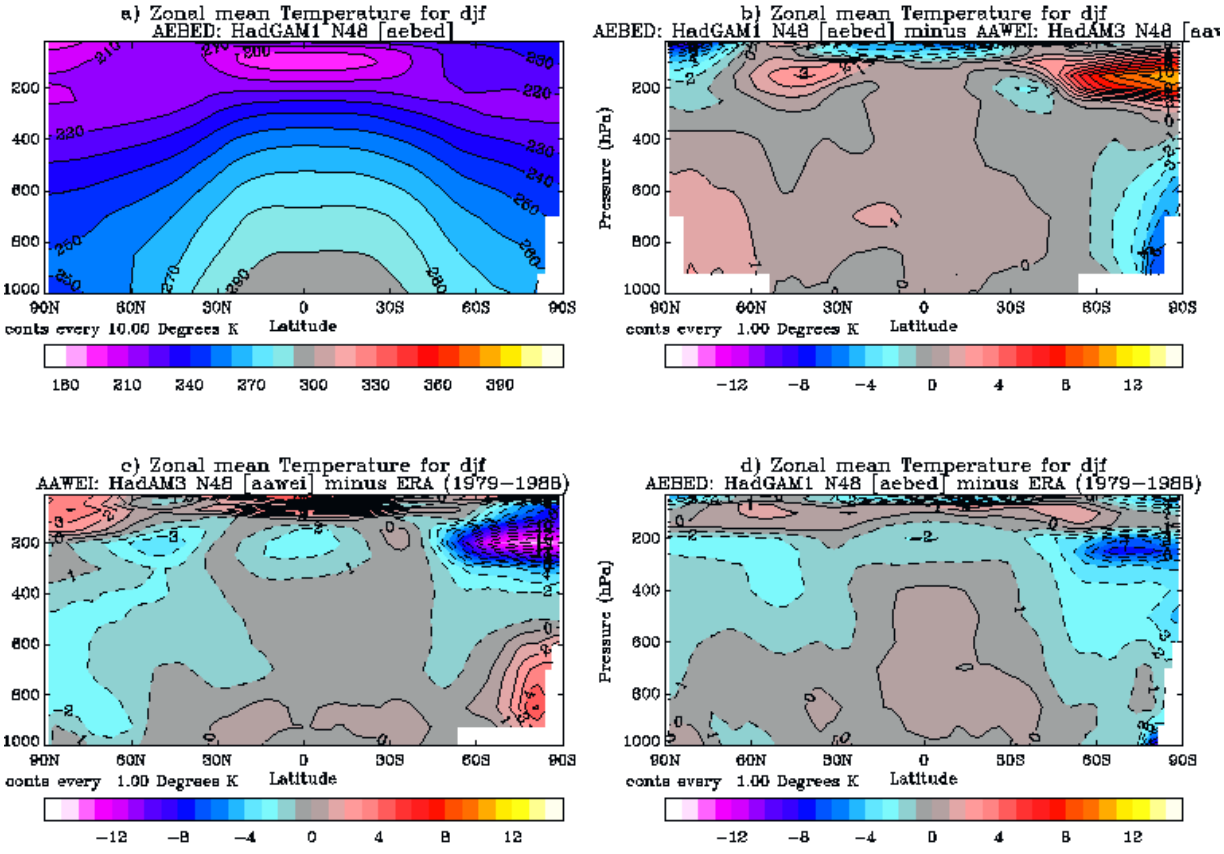

Figure 3: Zonal mean temperature in HadGAM1 and differences from HadAM3 and ERA

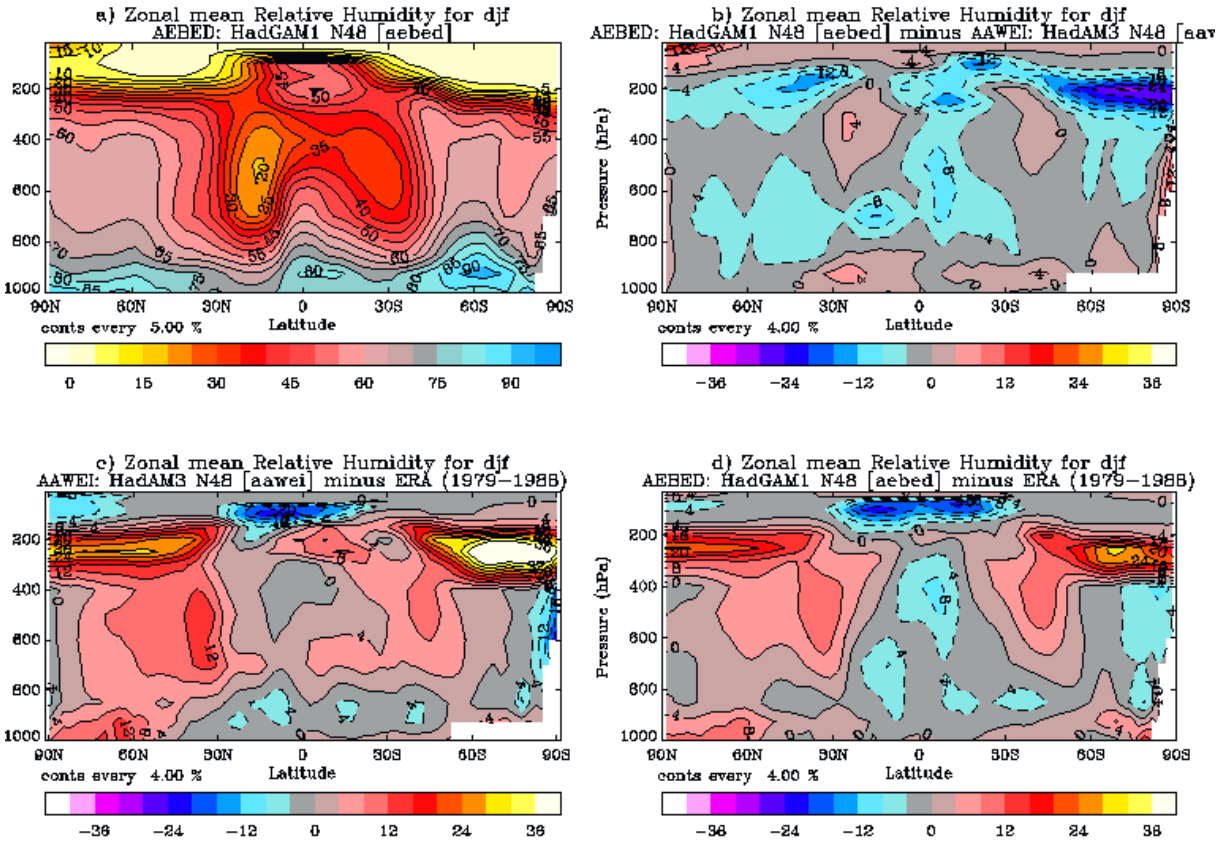

Figure 4: Zonal mean relative humidity in HadGAM1 and differences from HadAM3 and ERA

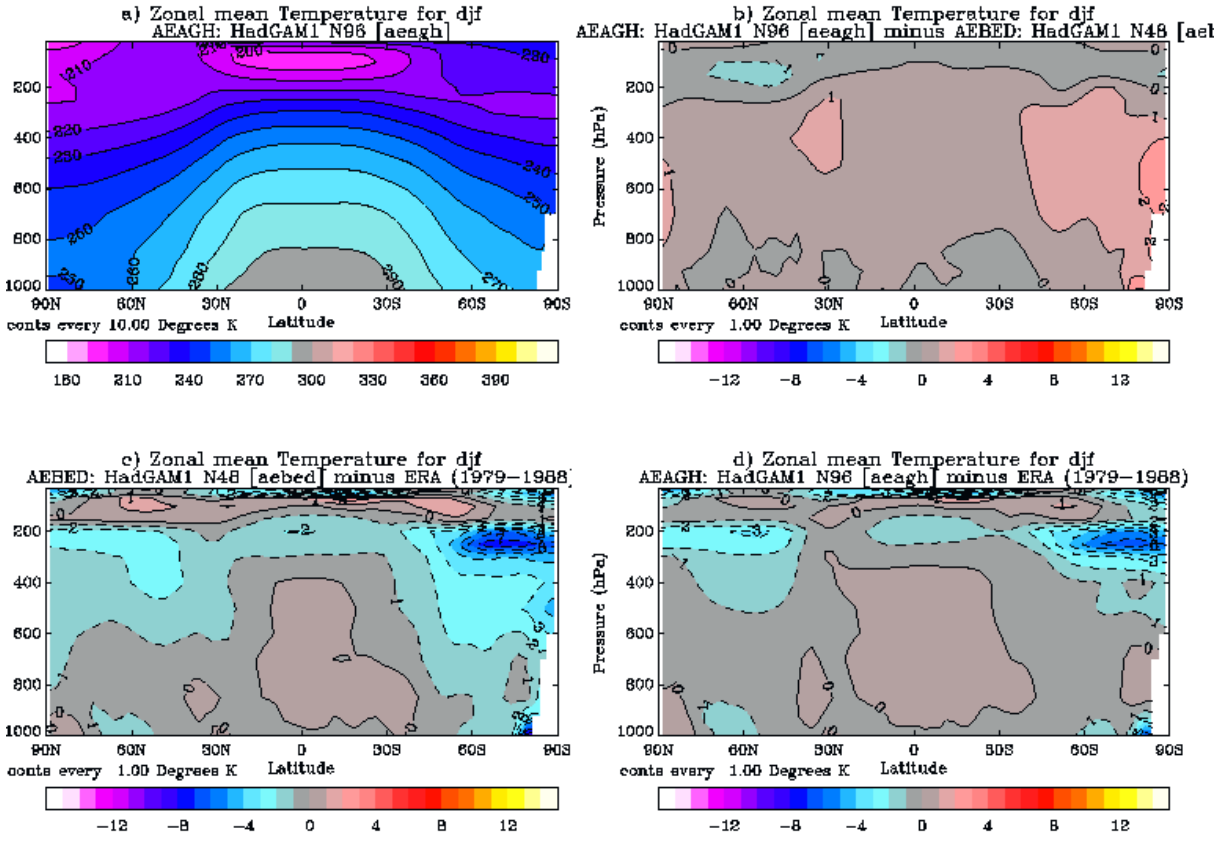

Figure 5: Zonal mean temperatures in HadGAM1 at N96 resolution and differences from N48 and ERA

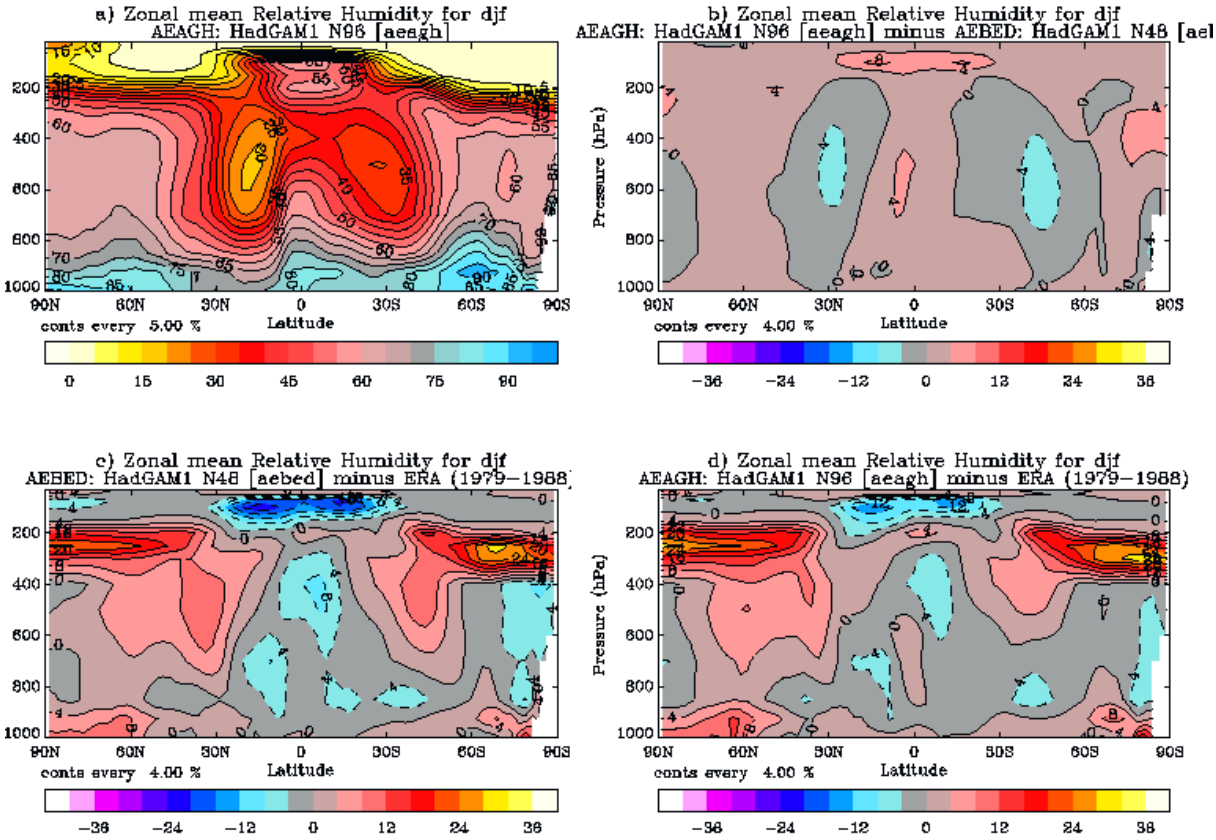

Figure 6: As Figure 5 but for relative humidity

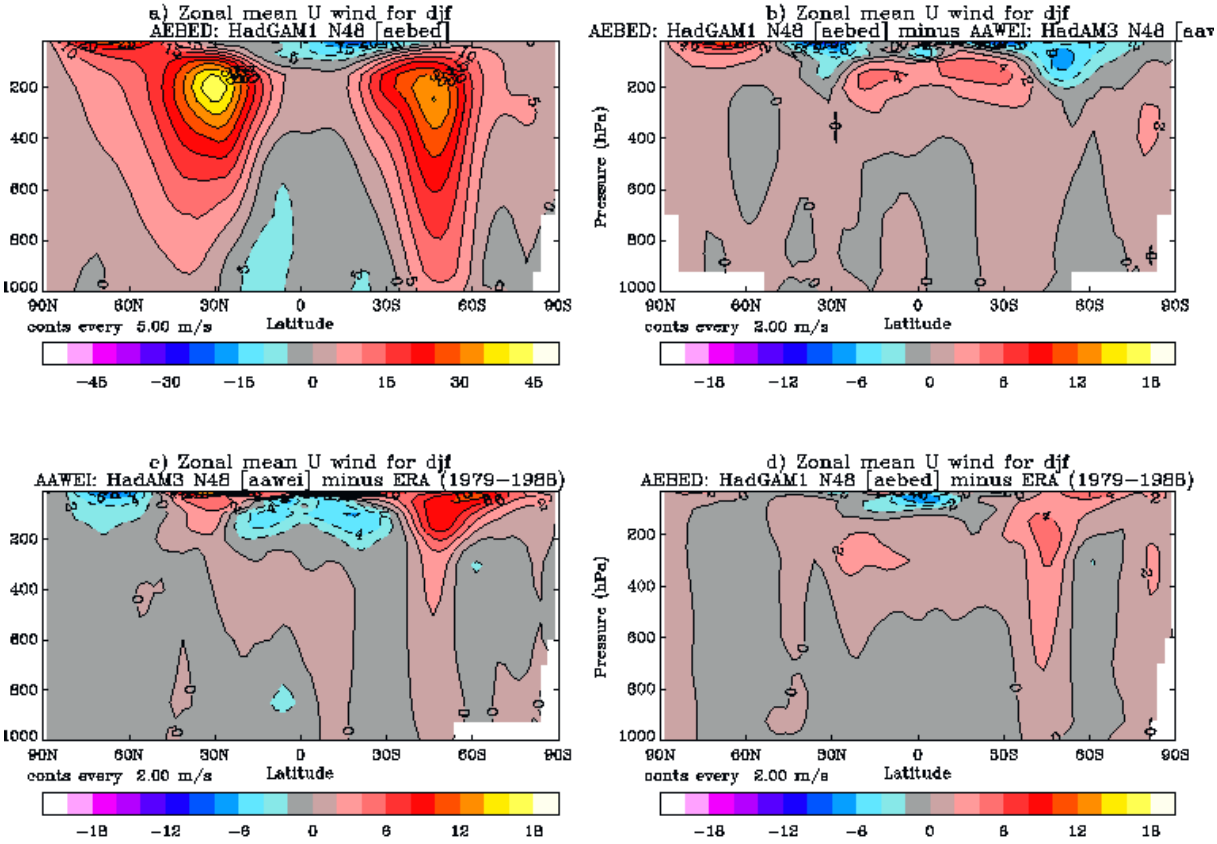

Figure 7: Zonal mean zonal wind in HadGAM1 and differences from HadAM3 and ERA

The only detrimental impact on the zonal winds in HadGAM1 is the reappearance of a westerly bias in the tropical mid- to upper-troposphere, which was removed in HadAM3. Increased tropical westerly winds at 200 hPa are seen mainly in the eastern Pacific and Atlantic and the northern Indian Ocean in DJF (see Section 5.2) and in a band between 235W and 90E in JJA (not shown). In both seasons these are in marked contrast with ERA, and are thought to be associated with the new convection scheme in HadGAM1, in which the occurrence of and transports due to convection are different. Figure 8 compares the meridional circulation in the two models. Although this is still too strong in the new model, in DJF it has decreased relative to HadAM3 and shows better agreement with ERA. In JJA (not shown) the circulation is narrowed and more concentrated at the equator. This is, once again, thought to be associated with the new convection scheme.

Figure 9 shows the changes in zonal winds between HadGAM1 at N48 and N96 resolution. As in HadAM3 (Pope and Stratton, 2002), the westerly jets move poleward with increasing resolution, but unlike HadAM3, agreement with ERA is mainly improved in the southern hemisphere, and the comparison is rather worse in the northern hemisphere. However, the tropical westerly bias in HadGAM1 is reduced by increasing resolution. Figure 10 shows that the increased resolution has a small detrimental impact on the meridional circulation in DJF. However, similar analysis of JJA (not shown) shows that the meridional circulation is improved in that season.

Comparison of HadGEM1 and HadGAM1 (both at N96 resolution) shows only small impacts on the zonal mean zonal winds, but there is a strengthening of the meridional circulation which increases the existing bias.

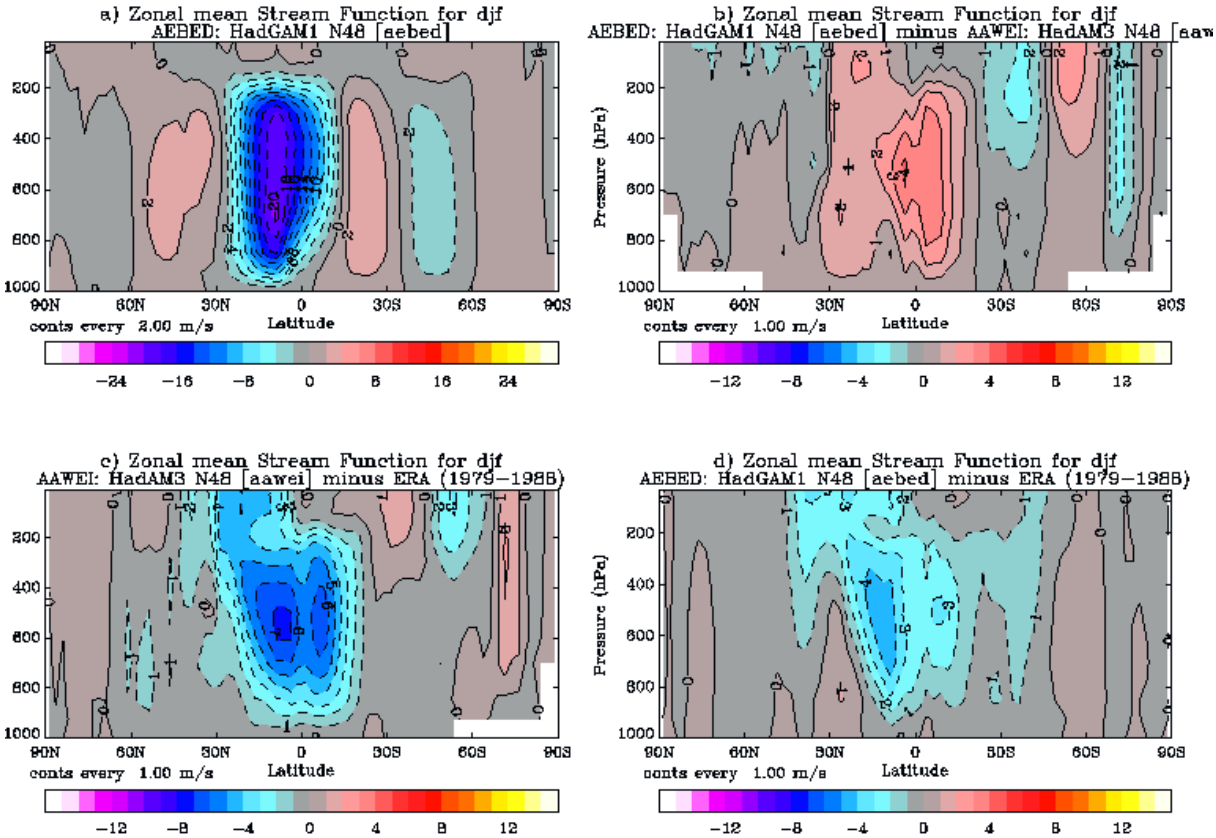

Figure 8: Zonal mean meridional streamfunction in HadGAM1 and differences from HadAM3 and ERA

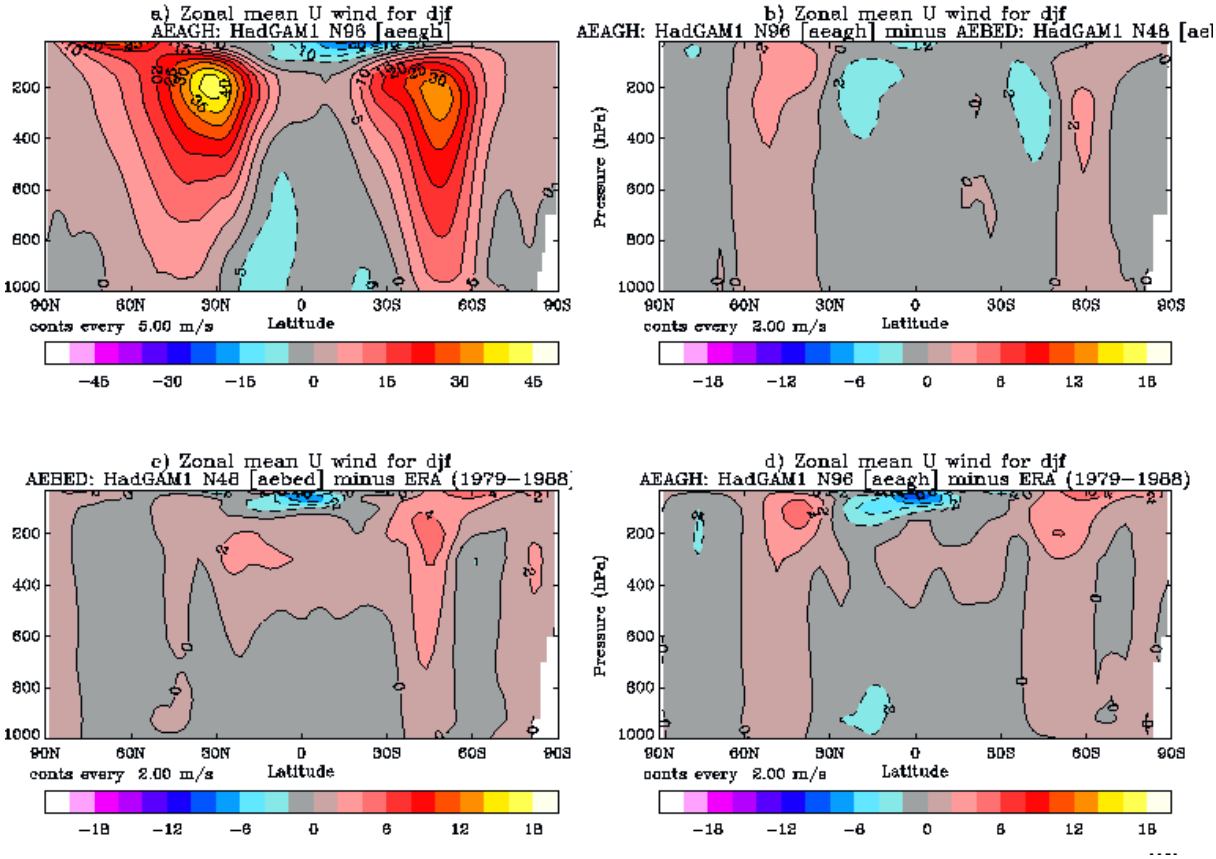

Figure 9: Zonal mean zonal wind in HadGAM1 at N96 resolution and differences from N48 and ERA

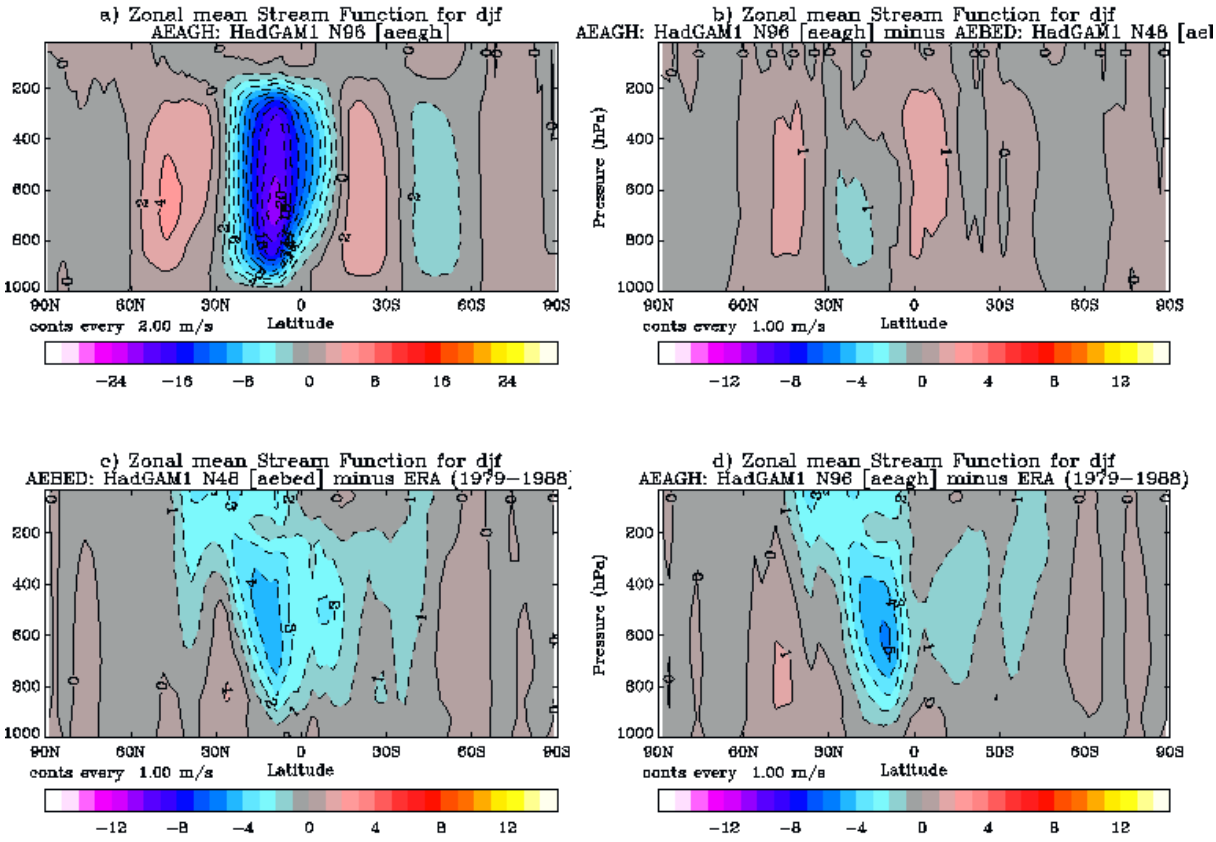

Figure 10: As Figure 9 but for meridional streamfunction

4.3 Transient eddy kinetic energy

Figure 11 shows the zonal mean transient eddy kinetic energy (EKE) in HadGAM1 and HadAM3 at N48 resolution. This is underestimated in both models at this resolution, although the error is larger in HadGAM1 as a result of the change to semi-Lagrangian dynamics which are not designed for such poor horizontal resolution. Figure 12 shows that increasing the horizontal resolution of HadGAM1 reduces the transient EKE errors considerably. This was also found to be the case in HadAM3 (Pope and Stratton, 2002). Stratton (2004a) demonstrated that the energetics of the semi-Lagrangian dynamical core used in HadGAM/GEM1 are highly sensitive to horizontal resolution. At N48 resolution, the eddy kinetic energy is less than that of the Eulerian dynamical core, demonstrating once again that the semi-Lagrangian dynamics are not designed for such poor resolution. At N96, Stratton (2004a) found that the eddy kinetic energy of the two dynamical cores was similar, and the semi-Lagrangian dynamics were closer to convergence.

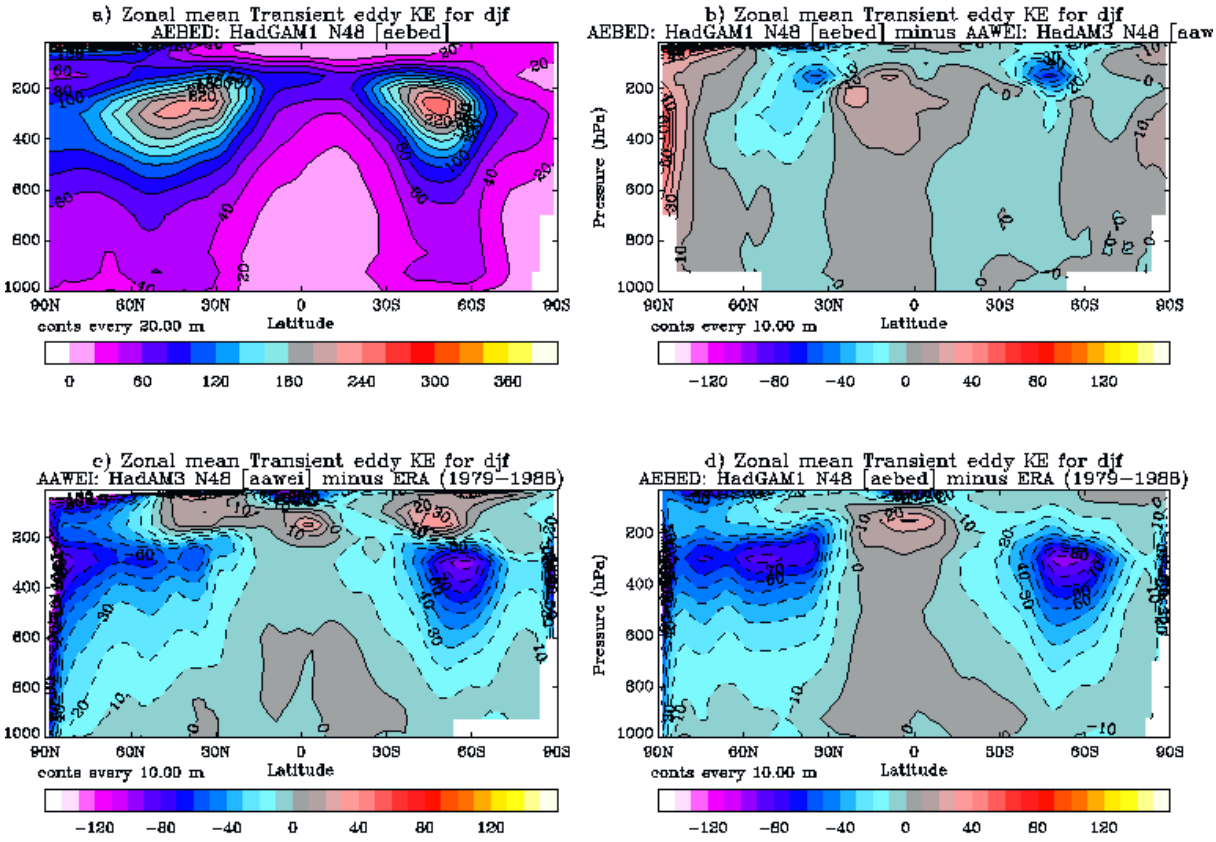

Figure 11: Zonal mean transient kinetic energy in HadGAM1 and differences from HadAM3 and ERA

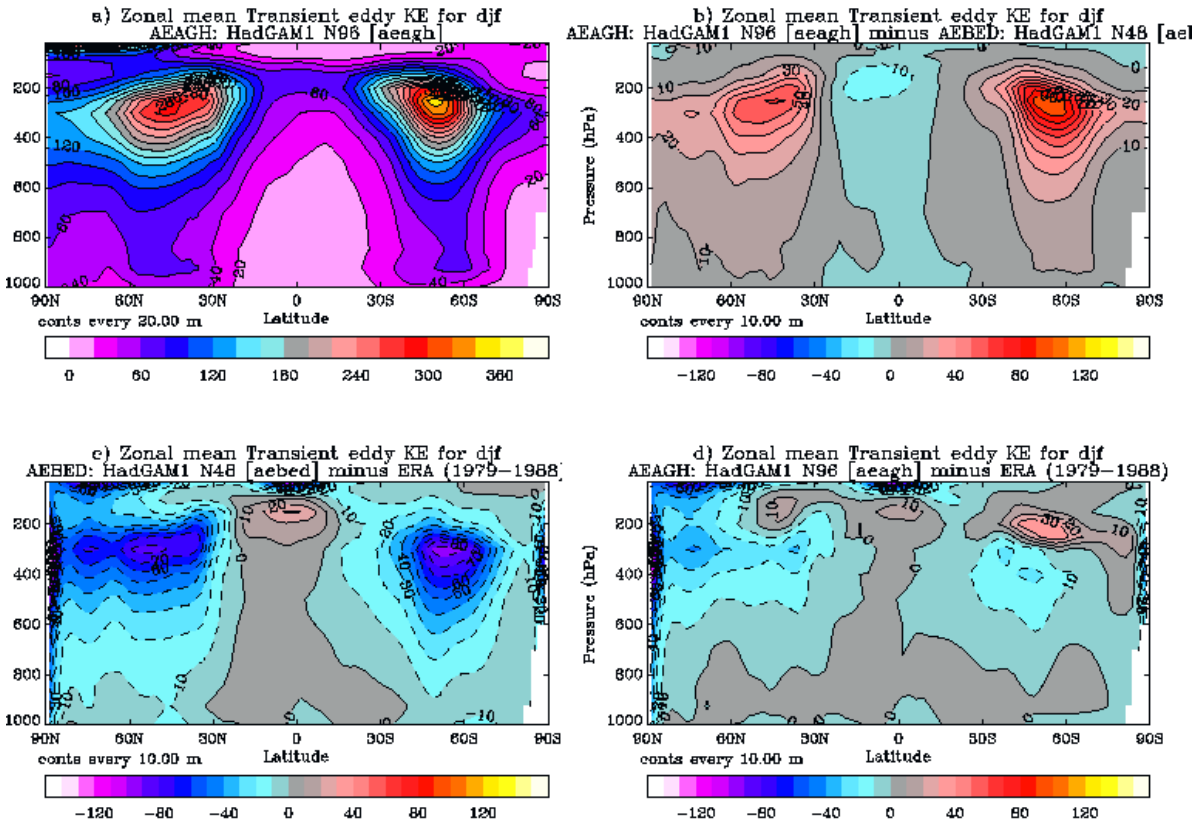

Figure 12: Zonal mean transient kinetic energy in HadGAM1 at N96 resolution in DJF and differences from N48 and ERA

5. Global climatologies

5.1 PMSL

There are improvements in a number of global mean fields in HadGAM1 compared with HadAM3. Some of these, e.g. mean sea-level pressure (Fig. 13) are mainly due to the change in dynamical core from Eulerian to semi-Lagrangian, which improves the advection. Fig. 13 shows a decrease in the high pressure bias at the winter pole (also seen near the south pole in JJA). There is also a reduction in the low pressure bias near the south pole in DJF. Positive pressure biases in winter (DJF) over the North Pacific and Atlantic are reduced, suggesting a reduction in blocking and/or an increase in strength of low pressure systems in the new model. This is discussed further in Section 6.

Increasing horizontal resolution in HadGAM1 improves some aspects of the surface pressures (Fig. 14). The remaining high pressure bias at high northern latitudes in DJF is reduced, although the low pressure bias over the south pole is increased. The polar pressure biases are also reduced slightly in JJA (not shown). The reduction in pressure biases is associated with improvements in the storm tracks at high resolution (see Section 6).

Figure 15 shows that there is an increase in the southern polar low pressure bias and a smaller increase in the northern polar high pressure bias in DJF in the coupled model HadGEM1. The high pressure biases in the north Pacific and Atlantic are also increased although that over Japan is reduced. The increase in high pressure bias in

the north Pacific and Atlantic is associated with weakening of the northern hemisphere storm track in the coupled model.

5.2 Winds

The Taylor diagrams in Fig. 2 indicate that the zonal wind errors are generally similar and the meridional winds worse in HadGAM1 compared with HadAM3. However, examination of the global fields suggests that, in many respects, the low-level winds are improved in HadGAM1 while the upper level winds are rather worse. This is reflected in Fig.s 16 and 17. At 850 hPa, the mid-latitude westerlies in the winter hemispheres are strengthened in HadGAM1 in both DJF and JJA, improving agreement with ERA. This is related to the reduction in high pressure bias near the pole, which is associated with the improved dynamics in the new model. Also at 850 hPa, the tropical winds are generally weaker, again improving agreement with ERA. At 200 hPa the situation is almost reversed, with existing errors in HadAM3 exacerbated in HadGAM1 and westerly biases appearing in the tropics. As mentioned in Section 4, both the improvements at low-levels and the detriments at upper levels in the tropics are thought to be associated with the change to the new convection scheme in HadGAM1.

Increasing the horizontal resolution of HadGAM1 results in small improvements in the 200 hPa winds but little overall impact at 850 hPa. In contrast, the changes in HadGEM1 compared with HadGAM1 are much larger, particularly at 200 hPa (Fig. 18). A large westerly bias appears over the equatorial Pacific, with a corresponding subtropical easterly bias on either side, in both DJF and JJA. This is associated with the development of cold equatorial SST anomalies in HadGEM1 (Johns et al., 2004).

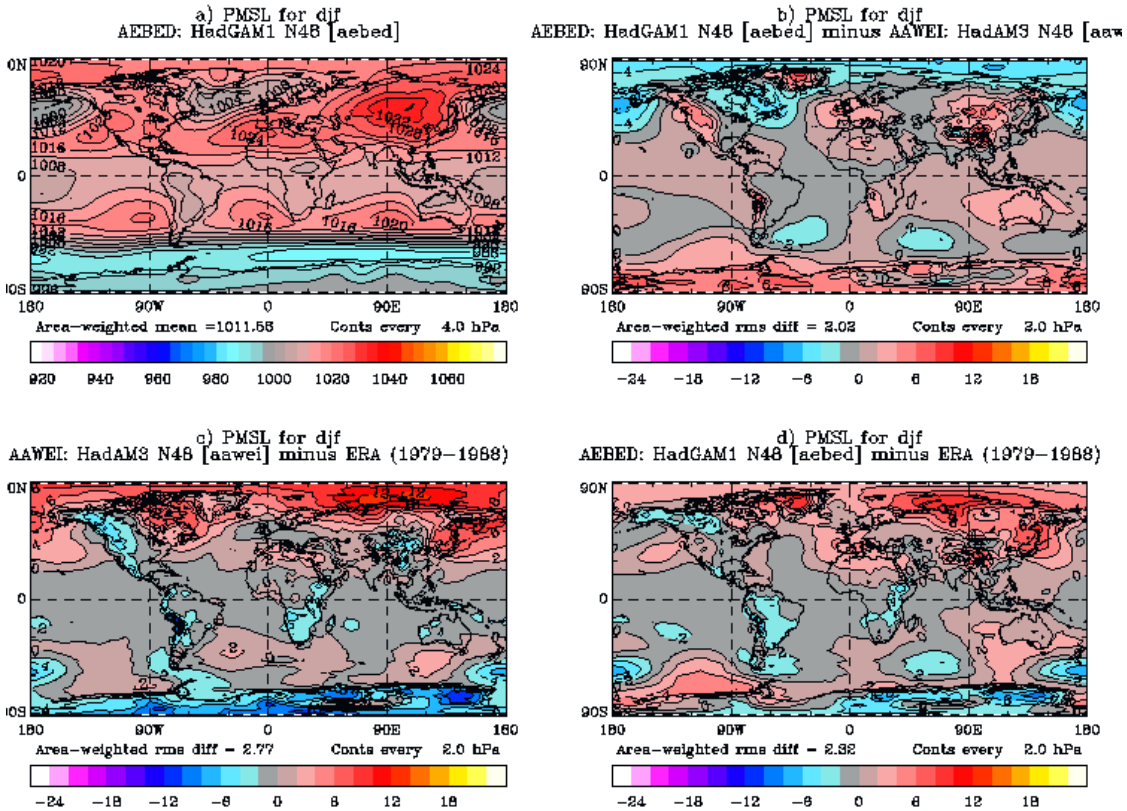

Figure 13: Mean sea level pressure in HadGAM1 in DJF and differences from HadAM3 and ERA

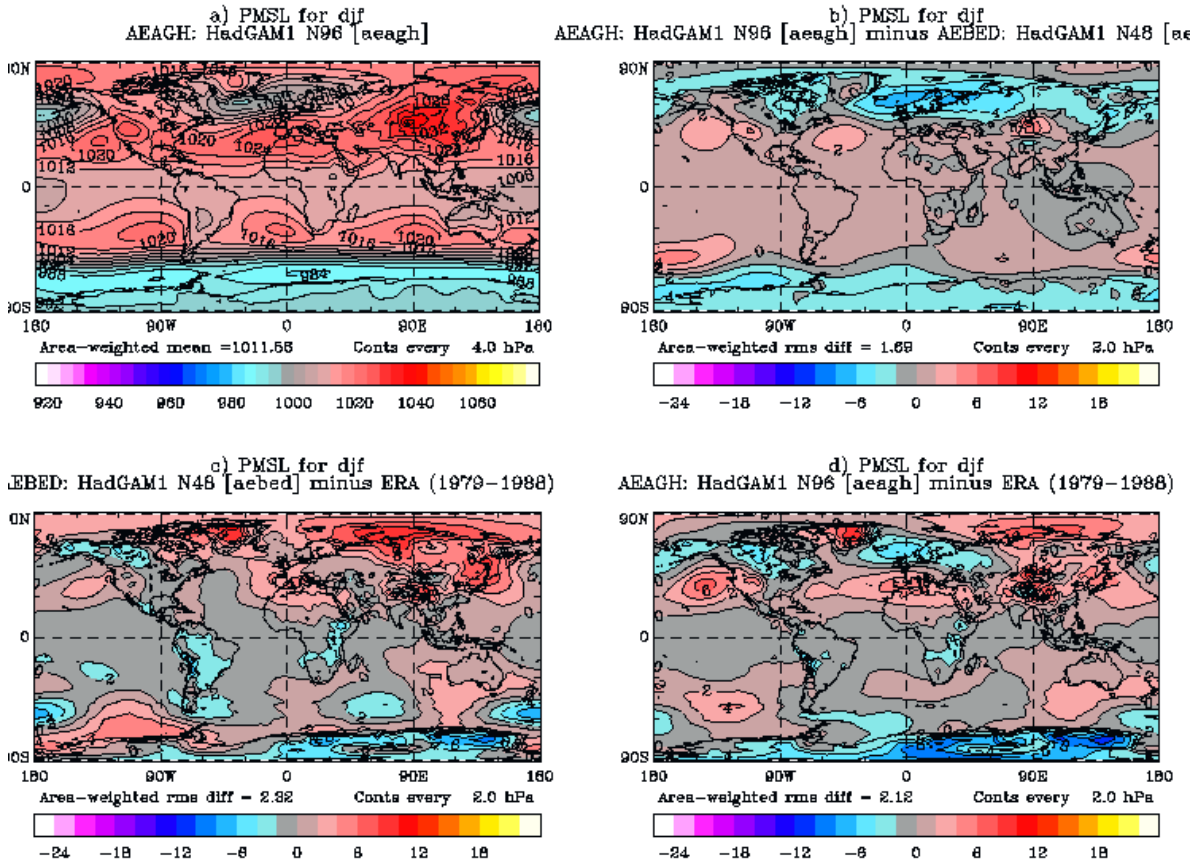

Figure 14: Mean sea level pressure in HadGAM1 at N96 resolution and differences from N48 and ERA

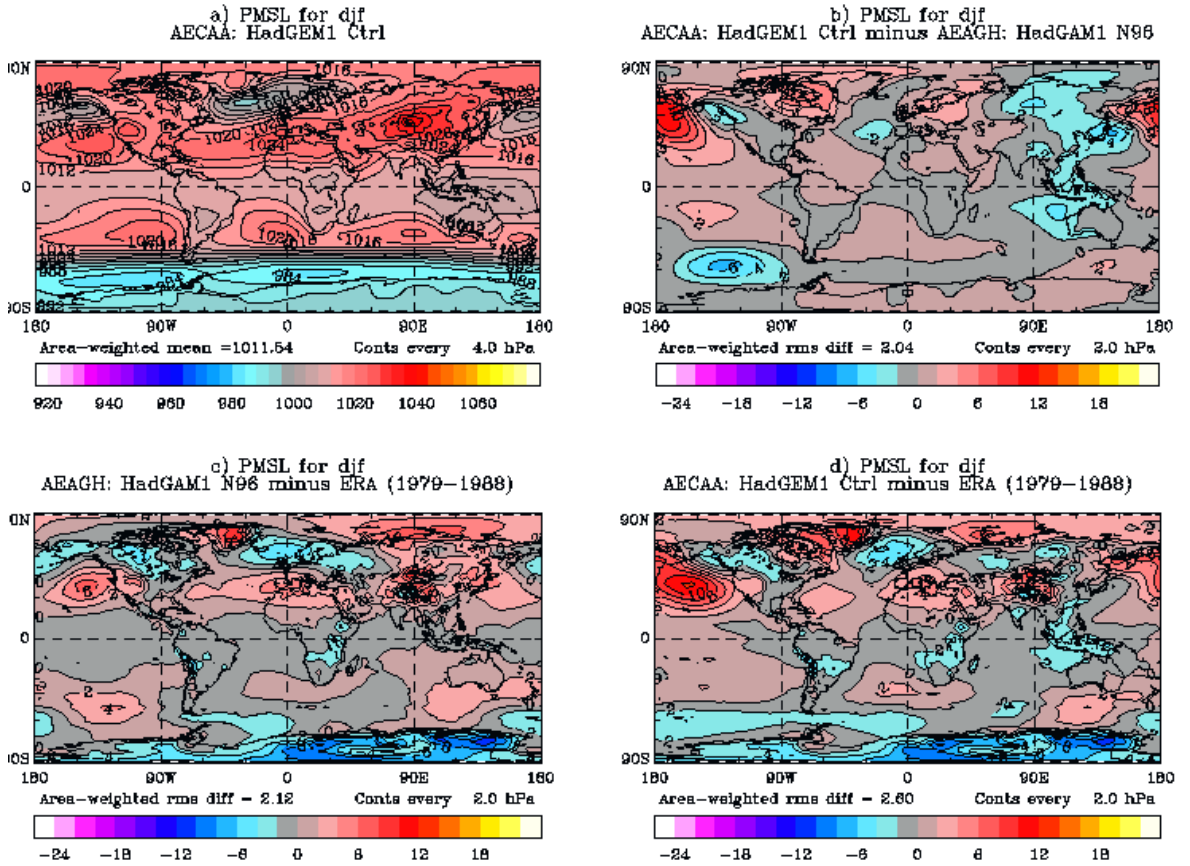

Figure 15: Mean sea level pressure in HadGEM1 (N96) and differences from HadGAM1 (N96) and ERA

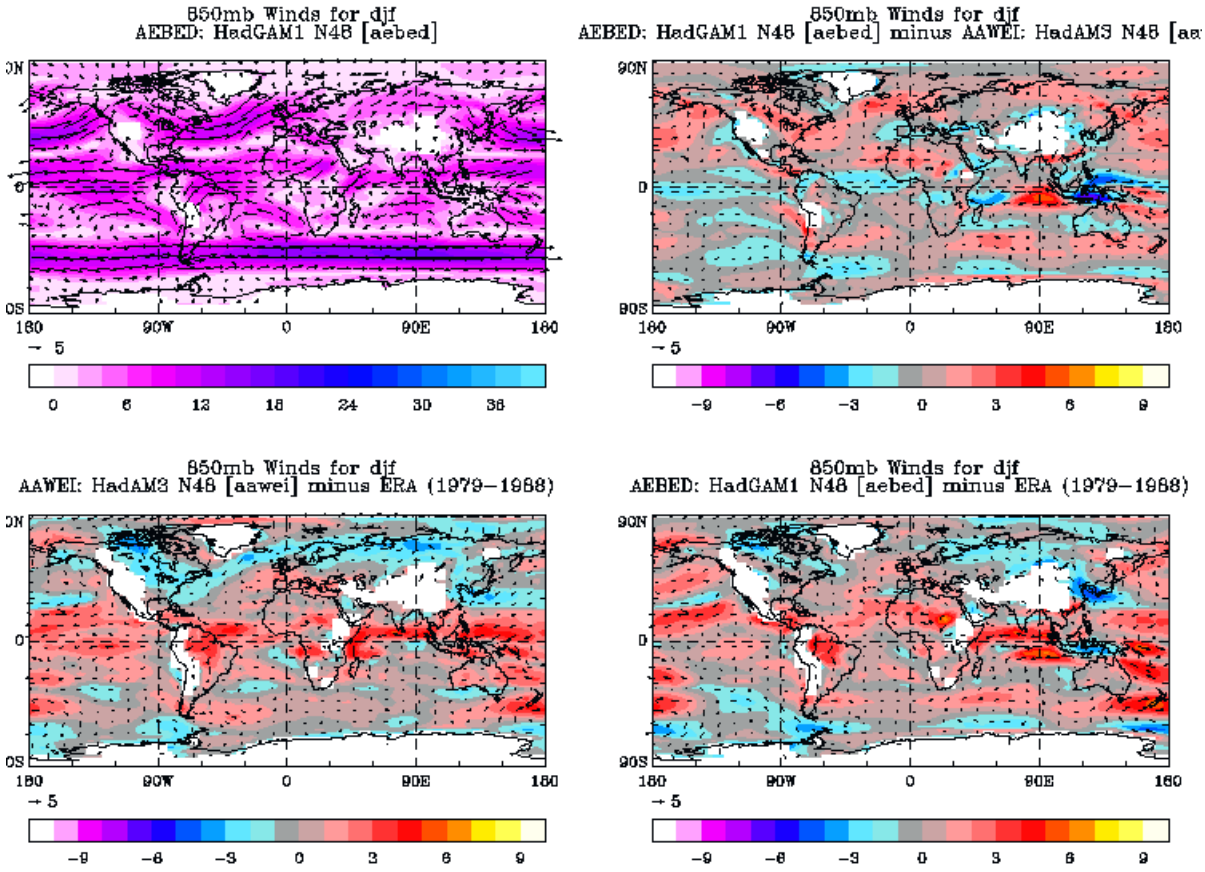

Figure 16: 850 hPa winds in HadGAM1 in DJF and differences from HadAM3 and ERA

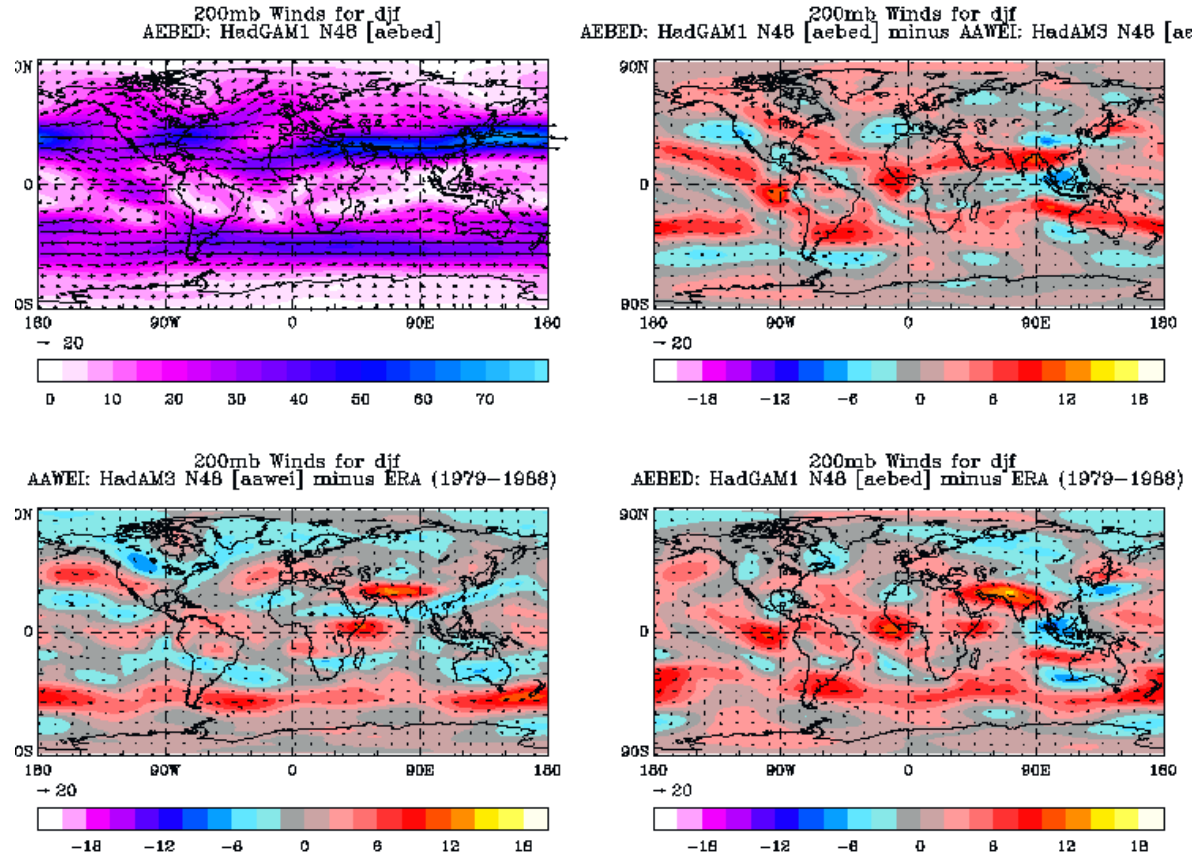

Figure 17: 200 hPa winds in HadGAM1 in DJF and differences from HadAM3 and ERA

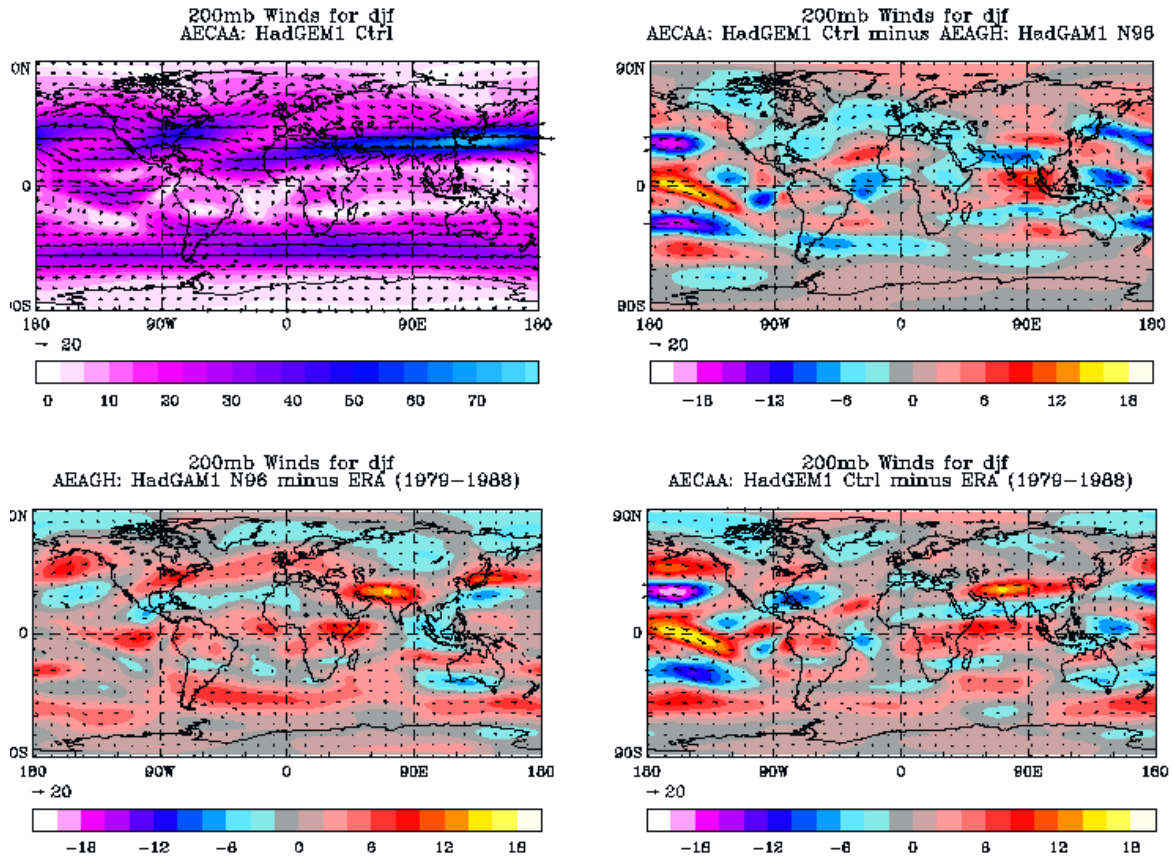

Figure 18: 200 hPa winds in HadGEM1 (N96) in DJF and differences from HadGAM1 (N96) and ERA

5.3 Radiation budget and clouds

This section presents an evaluation of the cloud and radiation budget climatologies in HadGAM1 (N96) against satellite observations. The representation of clouds and cloud feedbacks continues to provide a major source of uncertainty in climate modelling and climate change studies (Cubasch et al. 2001). It is thus desirable to compare a model's cloud and radiation fields with observations as this provides information on the simulation of cloud processes which is useful for improving the simulation of the present-day climate and may also help increase our confidence in predictions of climate change.

The radiation budget data are from ERBE (Harrison et al. 1990) and cover the period January 1985 to December 1989. The data are the continuous record from the ERBS satellite and provide information on both the total and clear-sky top-of-atmosphere (TOA) fluxes, allowing calculation of the cloud radiative forcing (CRF). We combine these with ISCCP-D2 data (Rossow and Schiffer 1999) for the same period. The ISCCP data provide information on clouds classified according to cloud top pressure (CTP) and visible optical depth (TAU). The model results used from HadAM3 and HadGAM1 correspond to this same five-year period. These include diagnostics which are directly comparable with the ISCCP data, derived using the ISCCP simulator (Klein and Jacob 1999; Webb et al. 2001). Here we consider the nine basic ISCCP cloud types (Table 2) – the full ISCCP data set (and the ISCCP

simulator) provides information on forty-two CTP-TAU categories. The analysis is restricted to 60°N-60°S as the satellite data are less reliable at higher latitudes.

CTP < 440 hPa (High)	Cirrus	Cirrostratus	Deep Convective
440 < CTP < 680 hPa (Middle)	Altocumulus	Altostratus	Nimbostratus
CTP > 680 hPa (Low)	Cumulus	Stratocumulus	Stratus
	0.3 < TAU < 3.6 (Thin)	**3.6 < TAU < 23 (Intermediate)**	**TAU > 23 (Thick)**

Table 2: Definition of the nine basic ISCCP cloud types.

5.3.1 Radiation budget and cloud radiative forcing

(a) Top-of-atmosphere radiation budget

Figure 19 compares the HadAM3 and HadGAM1 simulations of the five-year annual mean TOA radiation budget with ERBE. Note that the radiation budget components depend not just on the cloud simulations but also on the atmospheric temperature and water vapour distributions, the surface reflectivity, and other atmospheric constituents such as aerosols. Generally, it is reasonable to say that the HadGAM1 simulation compares either as well or better with the observations than HadAM3. Note that although the horizontal resolution of the HadGAM1 (N96) simulation is double that of HadAM3 (N48), we find that the increase in resolution alone makes little difference to the results presented here.

The most notable improvements in the reflected shortwave radiation (RSW) are found over areas of widespread marine stratocumulus cloud (off the west coasts of Peru, California, Southern Africa and Australia), over the tropical Indian and Pacific Oceans, over the Southern Hemisphere mid-latitude oceans, and over the major desert regions, most clearly over the Sahara. In all cases there is an increase in the shortwave reflected flux in HadGAM1 compared to HadAM3. The OLR distribution is broadly similar in the two models, with some improvement being seen over the tropical warm pool and the SPCZ. The OLR is overestimated in the sub-tropical subsidence areas, particularly in the Southern Hemisphere. As with HadAM3 (see Pope et al. 2000), this may well be indicative of an over vigorous Hadley Circulation leading to excessive drying in these regions. The distribution of the annual mean net TOA flux in both models compares well with ERBE.

(b) Cloud radiative forcing and total cloud amount

Further insight on the model cloud simulations can be gained by looking at the cloud radiative forcing (CRF) – the difference between the total (or all-sky) radiation budget fields shown above and those for cloud-free conditions. Figure 20 shows comparisons of the annual mean shortwave and longwave CRF from HadGAM1 and HadAM3 with ERBE data.

The shortwave CRF fields indicate that the improvements to the reflected shortwave radiation discussed above result primarily from an improved cloud

simulation. Note that the better simulation of the reflected shortwave radiation over the desert regions is not cloud related but is the result of a more realistic specification of the surface reflectivities. The longwave CRF shows clear improvements over the mid-latitudes (in both hemispheres) and over the tropical oceans. Over tropical land areas, however, there is no discernable improvement in the HadGAM1 simulation and the longwave CRF continues to be too low compared with ERBE.

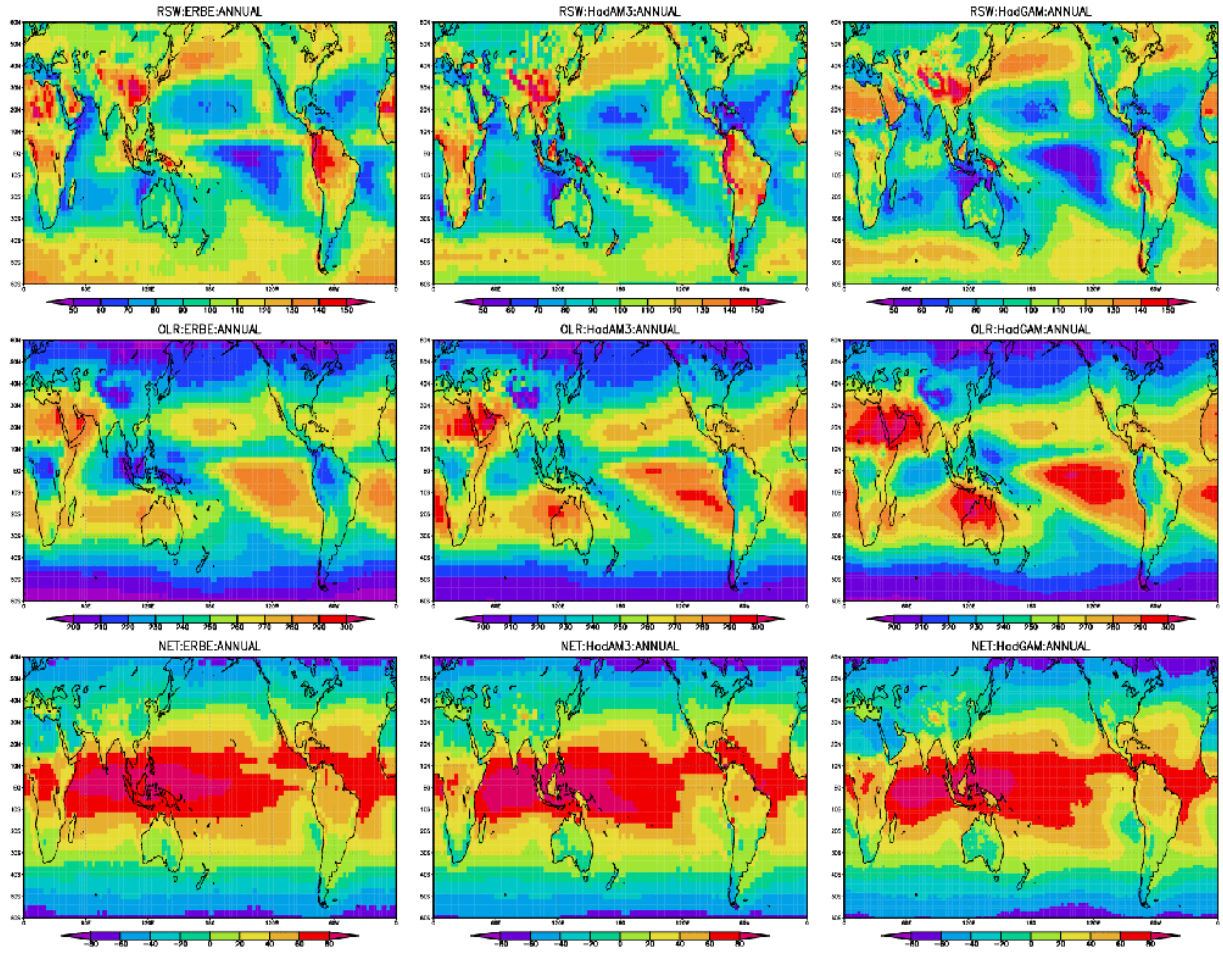

Figure 19: Comparison of the annual mean top-of-atmosphere reflected shortwave (top), outgoing longwave (centre) and net radiation (bottom) from ERBE with HadAM3 and HadGAM1 (Wm^{-2}).

Figure 21 shows comparisons with the net CRF from ERBE and the total cloud amount from ISCCP. The most marked improvement in the net CRF simulation in HadGAM1 is the representation of the near cancellation of shortwave and longwave CRF over the tropics, particularly the tropical oceans (Kiehl 1994).

The clearest improvement in the HadGAM1 simulation of the total cloud amount is the increase in cloud coverage in both the Northern and Southern Hemisphere mid-latitudes leading to a much more favourable comparison with the ISCCP data. There are also significant increases in regions of marine stratocumulus cloud – this type of cloud was largely absent in HadAM3 (see Section 5.3.3). It is still the case, however, that the cloud amount is underestimated in these areas. Indeed, it is evident that the total cloud coverage continues to be underestimated by

HadGEM1 in many areas, over both land and ocean. A good example of this are the subtropical oceanic subsidence regions, where the model generates very little cloud but the satellite observations often indicate cloud coverage of around 40% or greater.

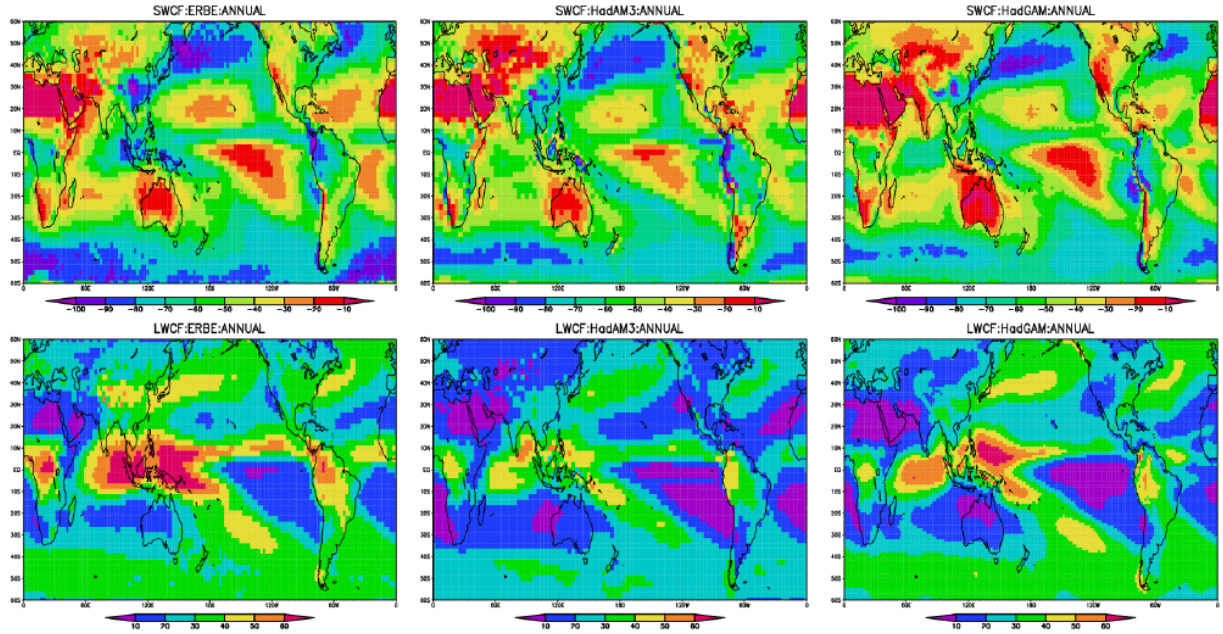

Figure 20: Comparison of annual mean shortwave (top) and longwave (bottom) cloud radiative forcing (Wm^{-2}) from ERBE with HadAM3 and HadGAM1.

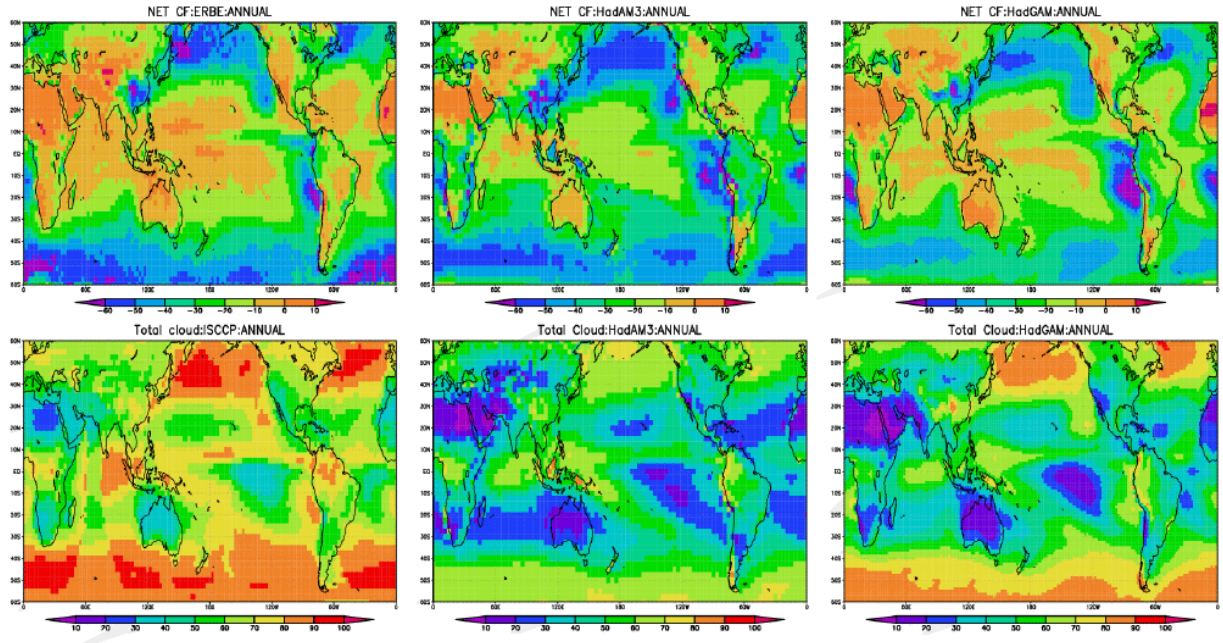

Figure 21: Comparison of annual mean ERBE net cloud radiative forcing (top) and ISCCP total cloud amount (bottom) with HadAM3 and HadGAM1.

It is possible that compensating errors (or even tuning of model cloud properties) can lead to apparently reasonable simulations of cloud radiative forcing even though the representation of clouds is in error (Webb et al. 2001). The areas of marine stratocumulus provide a good example of this – the HadAM3 and HadGAM1 shortwave and net CRF appear to be quite similar despite the fact that HadGAM1 produces significantly increased cloud amounts. A more detailed examination of the cloud properties is required in order to understand this.

5.3.2 ISCCP cloud types

Figure 22 compares the HadAM3 and HadGAM1 simulations of high-level clouds (CTP < 440 hPa) with ISCCP observations. The high cloud is divided into three broad optical depth categories: "thin" (TAU < 3.6), "intermediate" (3.6 < TAU < 23), and "thick" (TAU > 23). The most striking improvement in HadGAM1 is the simulation of cloud of intermediate optical depth. HadAM3 produces only very small amounts of this type of cloud and the improvement is primarily due to the inclusion of a parametrization for convective anvils (Ringer and Allan 2004). This increase in intermediate thickness high cloud is accompanied by a significant reduction in the optically thickest cloud that is also beneficial, although this cloud type is generally still overestimated by the model, particularly at mid-latitudes. The optically thin high cloud ("cirrus") is underestimated in general, particularly over land and over tropical oceans. Note that what is displayed here is the model cloud which has TAU > 0.3, as this is considered to be the minimum optical depth detectable by ISCCP – the model often produces significant amounts of cloud which is optically thinner than this threshold but this of course cannot be verified using ISCCP data.

Figures 23 and 24 show similar plots for middle- (440 hPa < CTP < 680 hPa) and low-level (CTP > 680 hPa) cloud. In this case only the thick and intermediate optical depth categories are shown as the ISCCP thin cloud tends to be less reliable at these levels. In both cases there are clear improvements in HadGAM1 compared with HadAM3. The middle-level cloud changes are similar to those in high cloud – generation of previously absent intermediate optical depth cloud and reduction of the optically thickest cloud, both of which lead to an improved comparison with the ISCCP data. The improvements to the low cloud are even more apparent: as noted above, HadAM3 achieved a reasonable simulation of the cloud radiative forcing in many areas by generating excessive amounts of optically thick cloud which compensated for a general lack of cloudiness. The improvements in the simulation of these low- and middle-level cloud types are particularly encouraging, as they continue to be source of difficulty for many current climate models (e.g. Lin and Zhang 2004). This aspect is discussed further in Section 5.3.3.

5.3.3 Stratocumulus regions

The persistent stratocumulus clouds which exist on the eastern margins of the oceans can strongly influence the global climate. Underestimates of stratocumulus cloud amount lead to excessive solar heating of the ocean surface and significant local surface temperature departures from observed climatologies when atmosphere and ocean GCMs are coupled. HadCM3 showed warm SST errors of around 3-4K in these areas (Gordon et al. 2000, Johns et al. 2004).

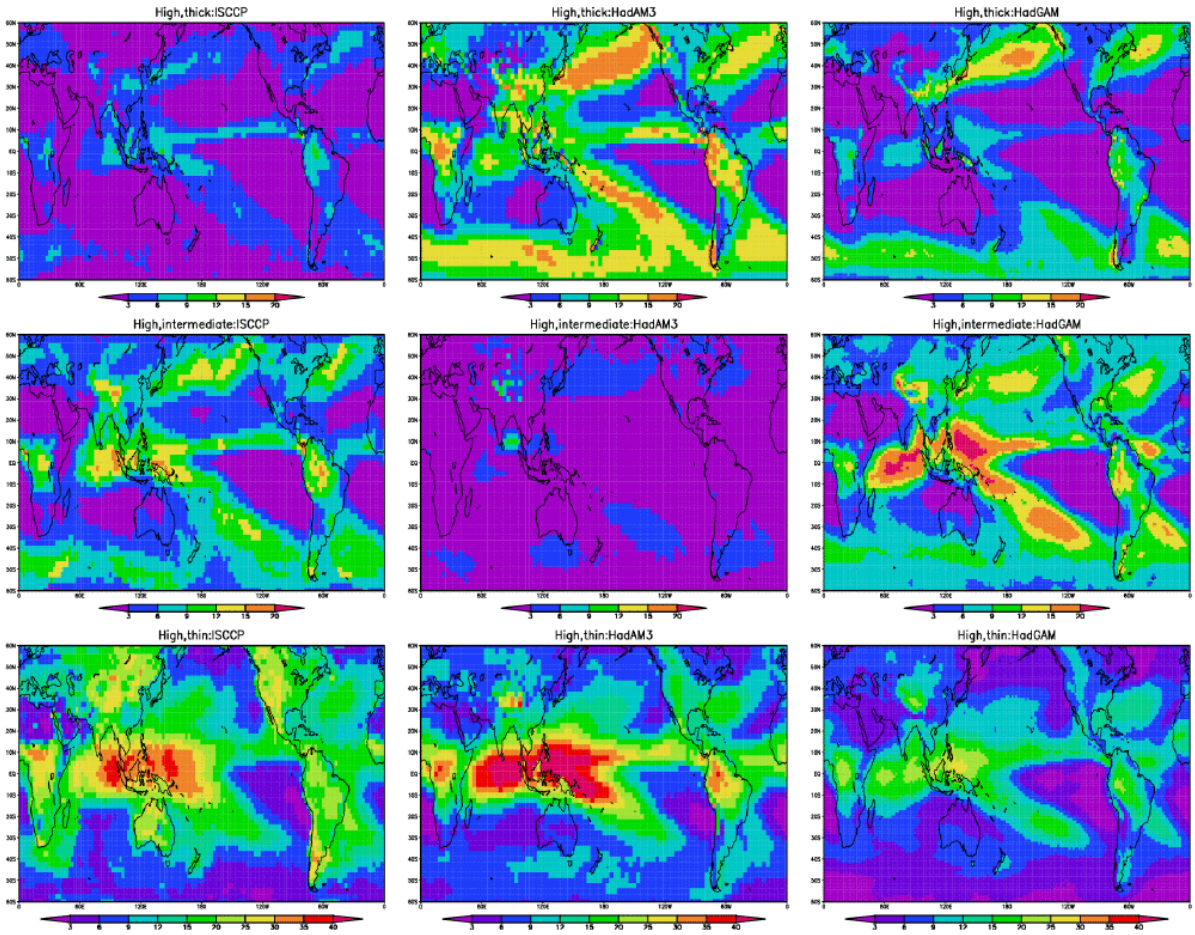

Figure 22: Comparison of annual mean ISCCP high-level thick (top), intermediate (centre) and thin (bottom) optical depth clouds (%) with HadAM3 and HadGAM1.

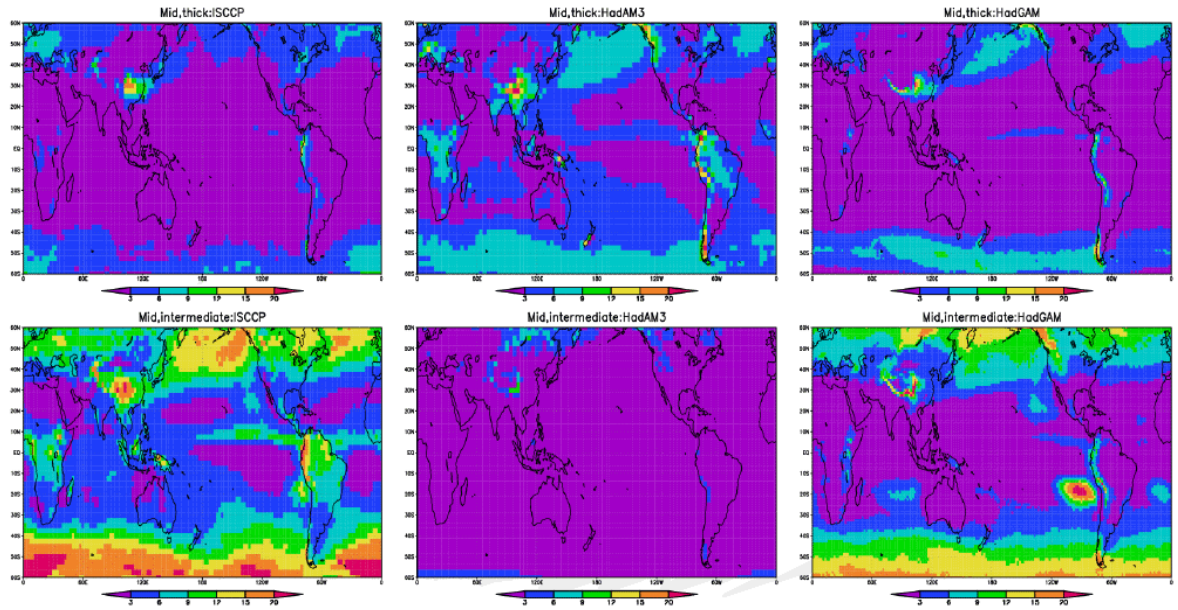

Figure 23: Comparison of annual mean ISCCP middle-level thick (top) and intermediate (bottom) optical depth clouds with HadAM3 and HadGAM1.

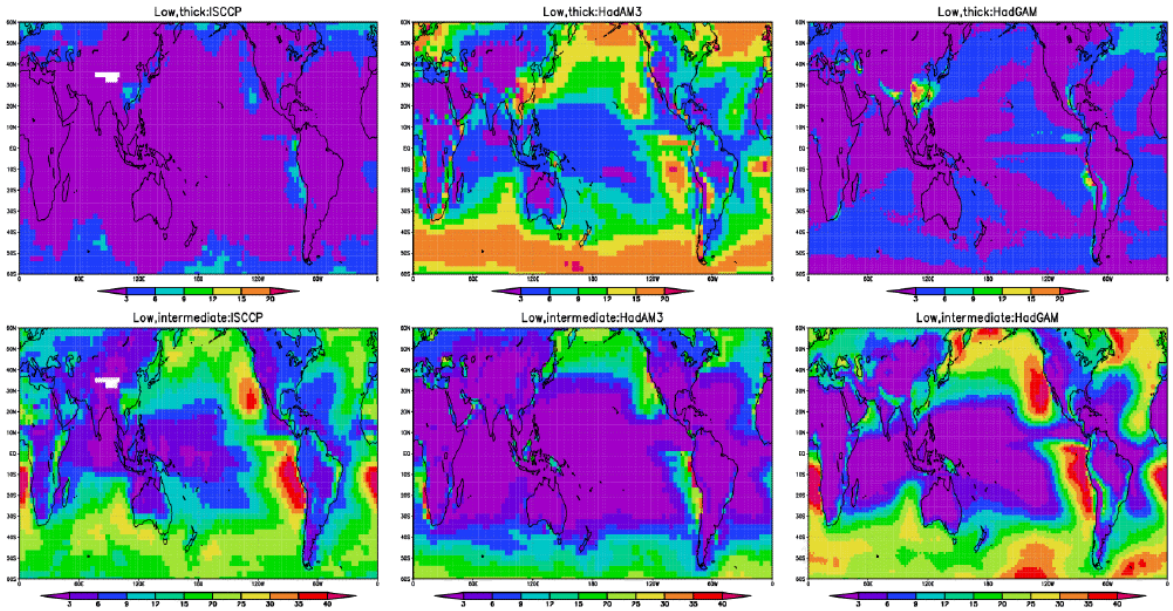

Figure 24: As Fig. 23 but for low-level cloud**.**

The tendency for marine stratocumulus clouds to occur in shallow layers beneath a marked temperature inversion makes the cloud very sensitive to the vertical temperature and moisture structure in the boundary layer. In a GCM, this structure is itself dependent on model details such as the vertical resolution and the representation of boundary layer mixing. In HadGAM1, both of these aspects have been improved. The vertical resolution has been increased threefold and a new boundary layer scheme is used. This includes a representation of non-local mixing (driven by both surface fluxes and cloud-top processes) in unstable layers, either coupled to or decoupled from the surface, and an explicit entrainment parameterization. The previous scheme, used in HadAM/CM3, used local Richardson number profiles to determine mixing coefficients, and did not represent entrainment explicitly. Without and explicit entrainment parametrisation, the model cannot achieve the balance between radiative, dynamical and turbulent processes that characterises stratocumulus-capped boundary layers. Local treatments of turbulent mixing lead to very unsatisfactory interactions with other parts of the model, particularly the convection scheme (Brown, 1995).

Lock et al. (2000) and Martin et al. (2000) described the new boundary layer scheme used by HadGAM1 and its performance in HadAM3 (with 31 vertical levels, which matches the resolution used in HadGAM1 in the mid- to lower-troposphere). They found improvements in the vertical structure of the stratocumulus-capped boundary layer, and in the transition from stratocumulus to trade cumulus. However, the cloud amounts, which were underestimated in HadAM3, were further underestimated with the new scheme. Tests of the same scheme were also made with a version of HadAM3 which incorporated the semi-Lagrangian, semi-implicit dynamical core, the Arakawa-C horizontal grid and the Charney-Phillips vertical grid, and the same changes to the way the physics is coupled to the dynamics as are used

in HadGAM1. These tests showed that deeper cloud-capped boundary layers and more realistic cloud amounts could be achieved in this model.

Figure 24 showed that low-level cloud amounts are increased everywhere in HadGAM1, but there are particularly large increases in the persistent stratocumulus regions off the coast of California, Peru, Namibia and Africa. These are regions where cloud amounts were consistently underestimated in HadAM3 but they are far more realistic in the new model. Consequently, there is far less warming of SSTs in these regions in the coupled model, HadGEM1 (see Johns et al, 2004), although a warming of 1-2K still occurs close to the coasts, where the boundary layer structure is affected by having mixed land/sea gridboxes.

The reasons behind the substantial improvement in stratocumulus cloud amounts in HadGAM1 are still not clear. One of the largest contributors to the balance of forcing on stratocumulus clouds is subsidence. The way in which the boundary layer scheme interacts with the model dynamics is crucial for the correct contribution of subsidence to this balance. It is thought that both the use of vertical diffusion coefficients which are calculated from balanced fields (rather than ones which have been sequentially updated during the time-step, as in HadAM3), and the Charney-Phillips vertical staggering of the momentum and thermodynamic variables (rather than the Lorenz staggering used in HadAM3), contribute to the observed improvements. The Charney-Phillips staggering in the vertical not only avoids having undesirable computational modes (which are present when using Lorenz staggering) but also has more accurate normal modes. The removal of computational modes avoids the possibility of oscillations between the distinct regimes above and below the subsidence inversion, which could upset the balance between the subsidence and the turbulent fluxes leading to collapse of the cloud layer. It should be emphasised that this hypothesis has not been tested rigorously and remains speculative.

5.4 Surface fields

5.4.1 1.5m temperature

Surface temperatures were found to be too cold in HadAM3 (Pope et al., 2000). Figure 25 shows that this cold bias remains in HadGAM1, although it is reduced slightly in several areas, particularly northern Siberia in DJF. The strength of the cold bias in different regions is modulated by the errors in low level advection (Figure 16). The improvement in northern Siberian surface temperatures is related to the reduction in the easterly wind bias over northern Eurasia which was tending to reduce the advection of warm air from the Atlantic. Over North America, the removal of a south-easterly wind bias associated with a strengthening of the low level westerly winds in HadGAM1 has resulted in reduced surface temperatures in the northeast of the continent and a small cold bias there. Increased cold biases are also seen over central Eurasia and over the Sahara. The reasons behind the cooling of the Sahara are not clear. Attempts have been made to address this through realistic changes to the surface vegetation and soil albedo but the problem remains.

Increasing the horizontal resolution leads to improved surface temperatures over the northern continents but little impact elsewhere (not shown).

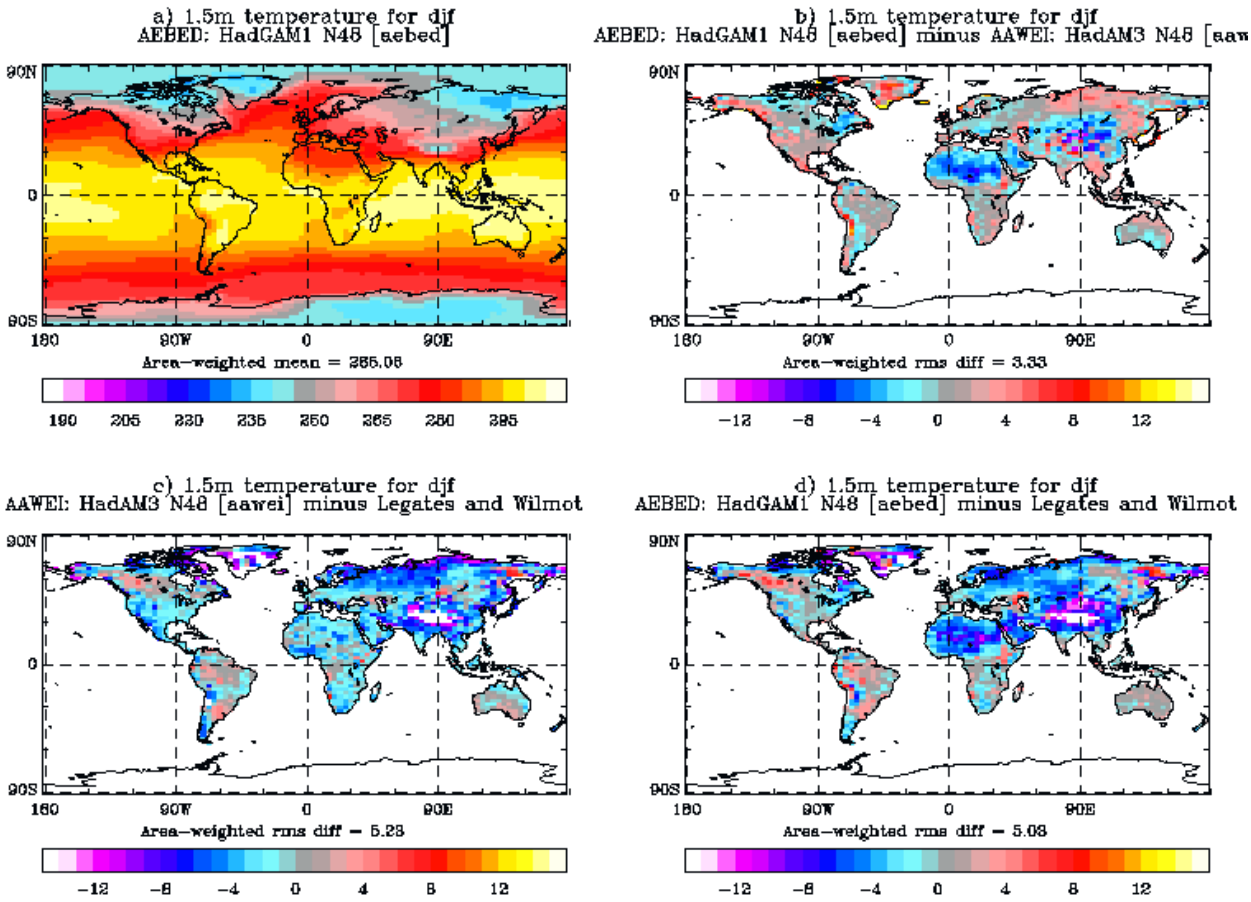

Figure 25: 1.5m temperature in HadGAM1 in DJF and differences from HadAM3 and Legates and Wilmot climatology

5.4.2 Surface wind stress

Surface wind stresses in the tropics are stronger in HadGAM1 than HadAM3, moving further from the climatology. Figure 26 shows the results for JJA, when the error is largest. Increasing the horizontal resolution has a small beneficial impact on this error, at least in the Pacific (not shown). However, this error is thought to be responsible for the development of a cold SST bias in the Pacific in HadGEM1. The coupled model results (Fig. 27) show that, after spin-up (during which the equatorial SSTs cool by 2 K), the main wind stress error has shifted to the western equatorial Pacific. This error is related to the precipitation changes in the coupled model (see below). HadGAM/GEM1 develop additional wind stress errors over the subtropical oceans, which are also related to the development of cold SST errors in HadGEM1.

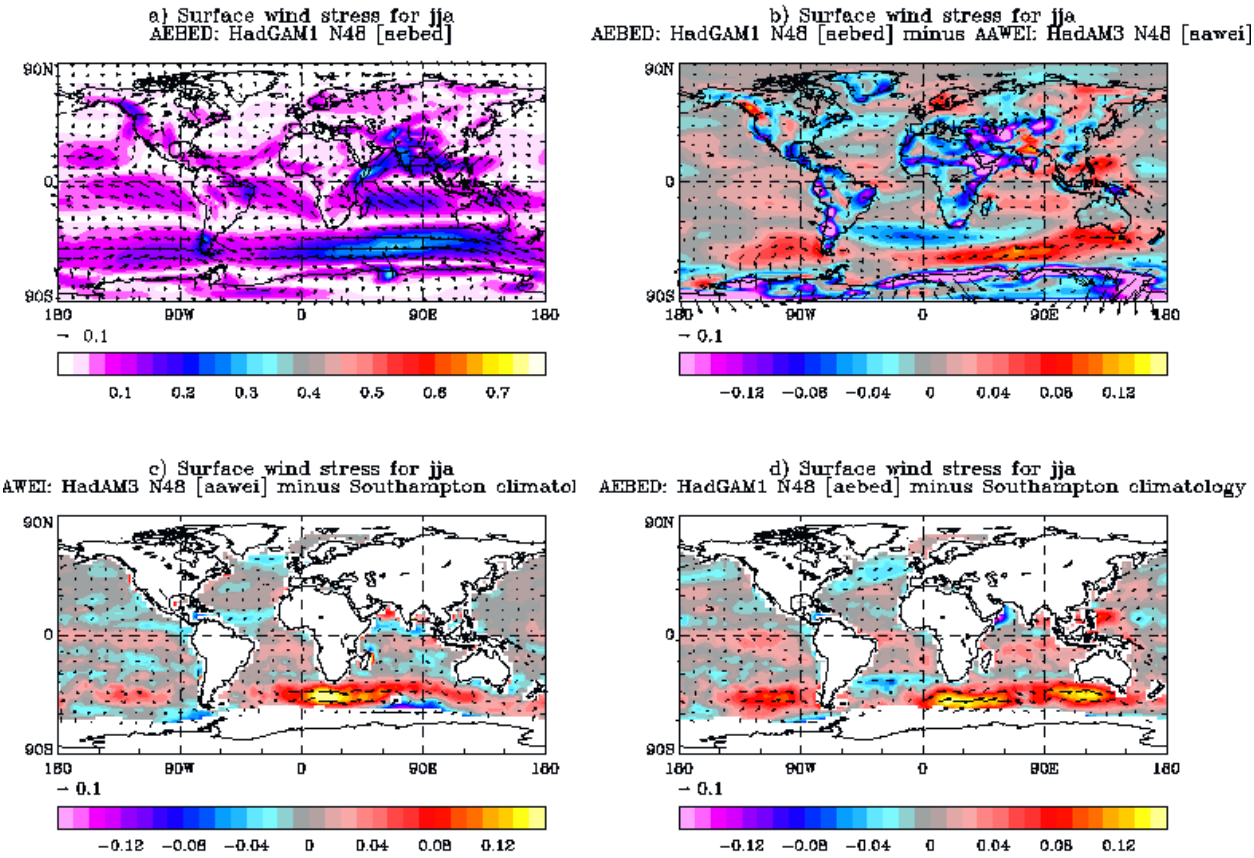

Figure 26: Surface wind stress in HadGAM1 in JJA and differences from HadAM3 and Southampton climatology

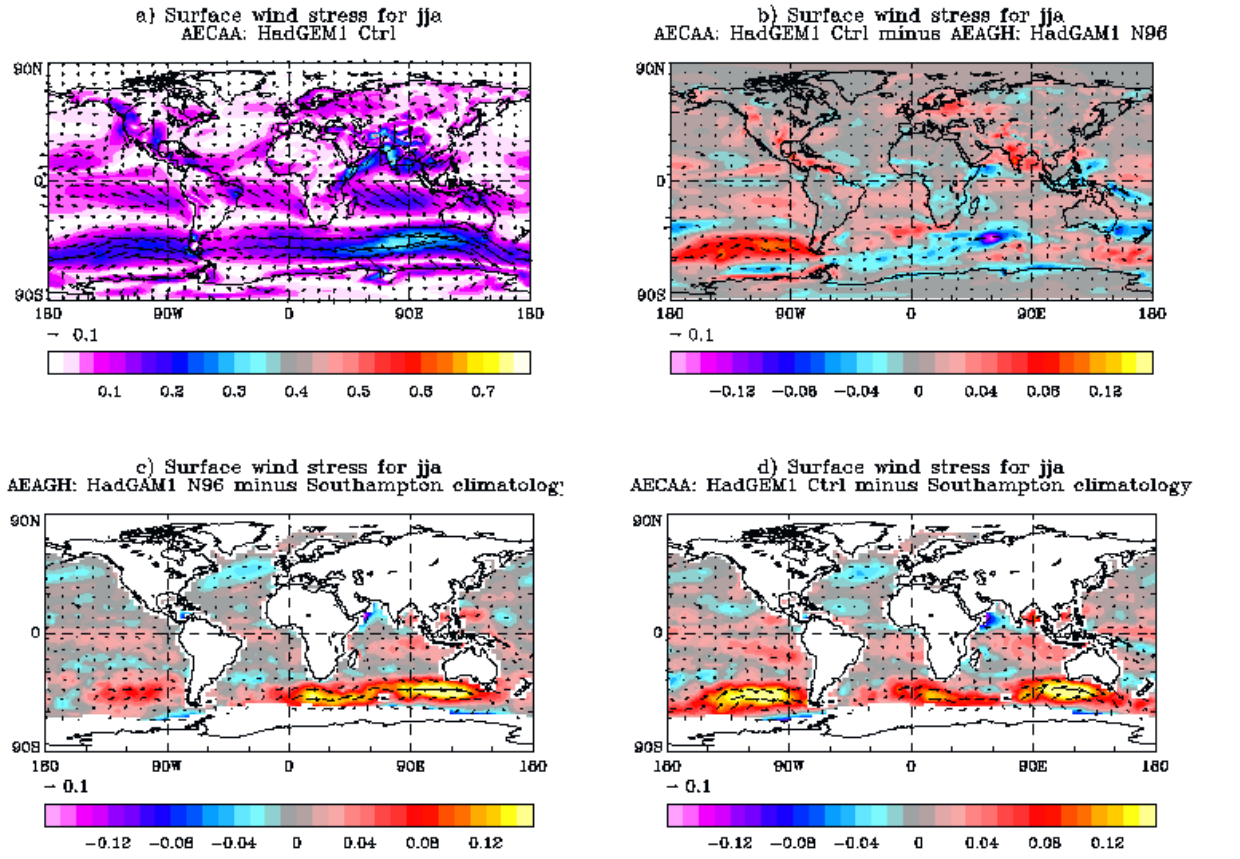

Figure 27: Surface wind stress in HadGEM1 (N96) in JJA and differences from HadGAM1 (N96) and Southampton climatology

5.5 Precipitation

Various aspects of the tropical performance of HadGAM/GEM1 were discussed by Martin et al. (2004). They found that although there are some local improvements in the precipitation climatology, there is an overall increase in the root-mean-square (rms) error compared with observations. Figure 28 shows the comparison of HadGAM1 with HadAM3 in DJF. The main region where the precipitation errors increase, in both DJf and JJA, is around the maritime continent. Convective activity over this region is a major driving force of the global atmospheric circulation. However, deficiencies in the model physics, particularly the convection scheme, contribute to a lack of convection in this region. Aspects which remain poorly-represented in HadGAM1 include the treatment of cloud anvils detraining from the top of deep convection, the diurnal cycle of convection over land and the complex circulation patterns generated by land-sea contrasts.

In addition, Pope et al. (2001) showed that the behaviour of the convection scheme is affected by changes in vertical resolution. They compared HadAM3 with the standard 19 levels against a 30 level version with enhanced resolution in the mid- to upper-troposphere. They found that the L30 model was better able to resolve the vertical structure of the stable region which occurs around the melting level. This tends to promote additional detrainment from convection in this region (largely as a result of an unrealistic dependence of the detrainment scheme on resolution), and the resulting further stabilization of the mid-troposphere means that subsequent convection is not as deep on average in these regions, consistent with reduced precipitation. Pope et al. (2001) found decreases in rainfall over the maritime continent and over South America and southern Africa in the L30 version, with corresponding increases elsewhere. The vertical resolution in HadGAM1 is greater throughout the depth of the atmosphere than in HadAM3. Martin et al. (2000) showed that the model is extremely sensitive to changes in lower tropospheric resolution, mainly through changes in the behaviour of the boundary layer and convection parametrisations. The new convection scheme used in HadGAM1 requires a certain degree of vertical resolution in the boundary layer, and many of the changes are designed to improve its interaction with the boundary layer scheme. Thus, it is not possible to separate the impacts of increased resolution at lower levels from the impacts of the changes to the parametrisation. However, it is likely that the impact of increased vertical resolution around the melting level on the detrainment from convection is contributing to the changes seen in Figure 28.

Martin et al. (2004) showed that a lack of convection over the maritime continent is associated with errors in the monsoon precipitation and unrealistic extension of the monsoon jet into the western Pacific in HadGAM1 in JJA. There is an overall increase in the hydrological cycle in HadGAM1 compared with HadAM3, although Fig. 28 illustrates that the inter-tropical convergence zone has narrowed and intensified.

Increasing horizontal resolution improves the precipitation in many areas, including in the region of the maritime continent in both DJF (Figure 29) and JJA (not shown). The improvements in JJA are associated with a small reduction in the unrealistic extension of the Asian monsoon jet into the west Pacific.

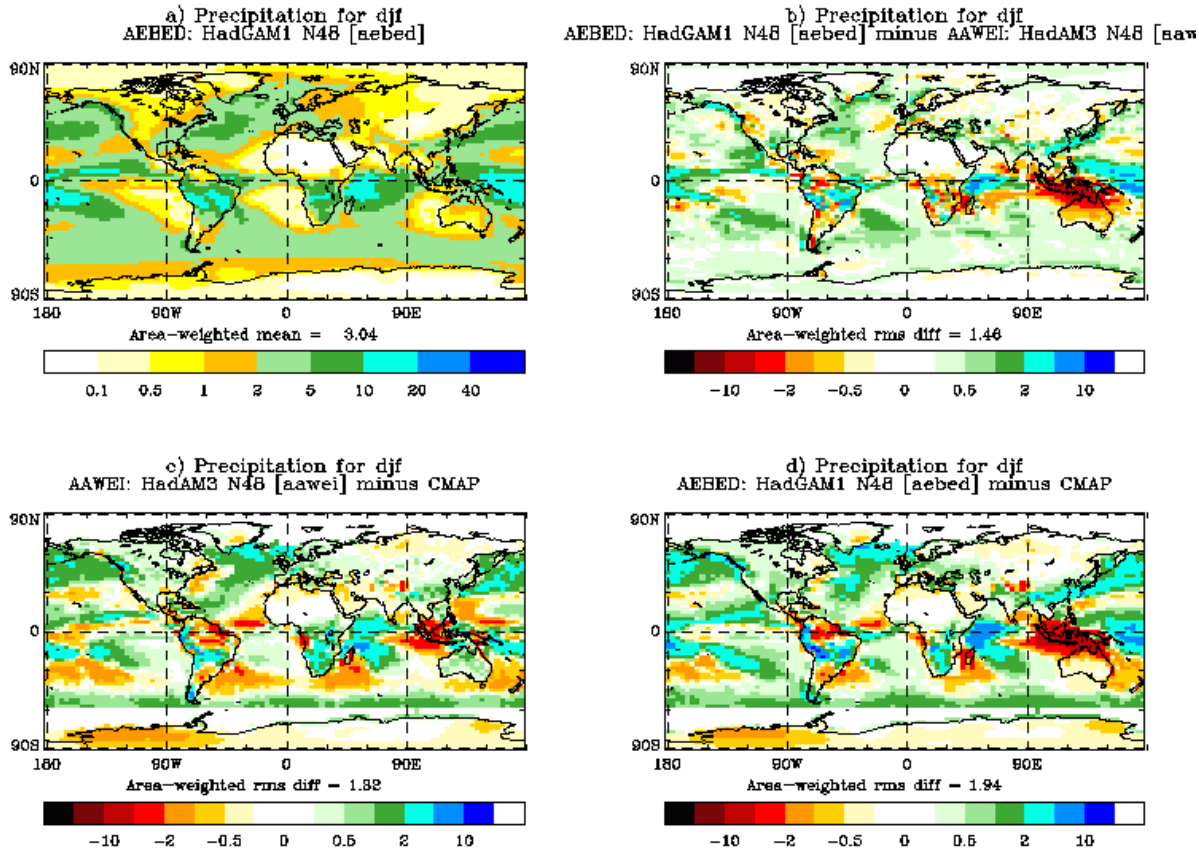

Figure 28: Precipitation in HadGAM1 in DJF and differences from HadAM3 and CMAP

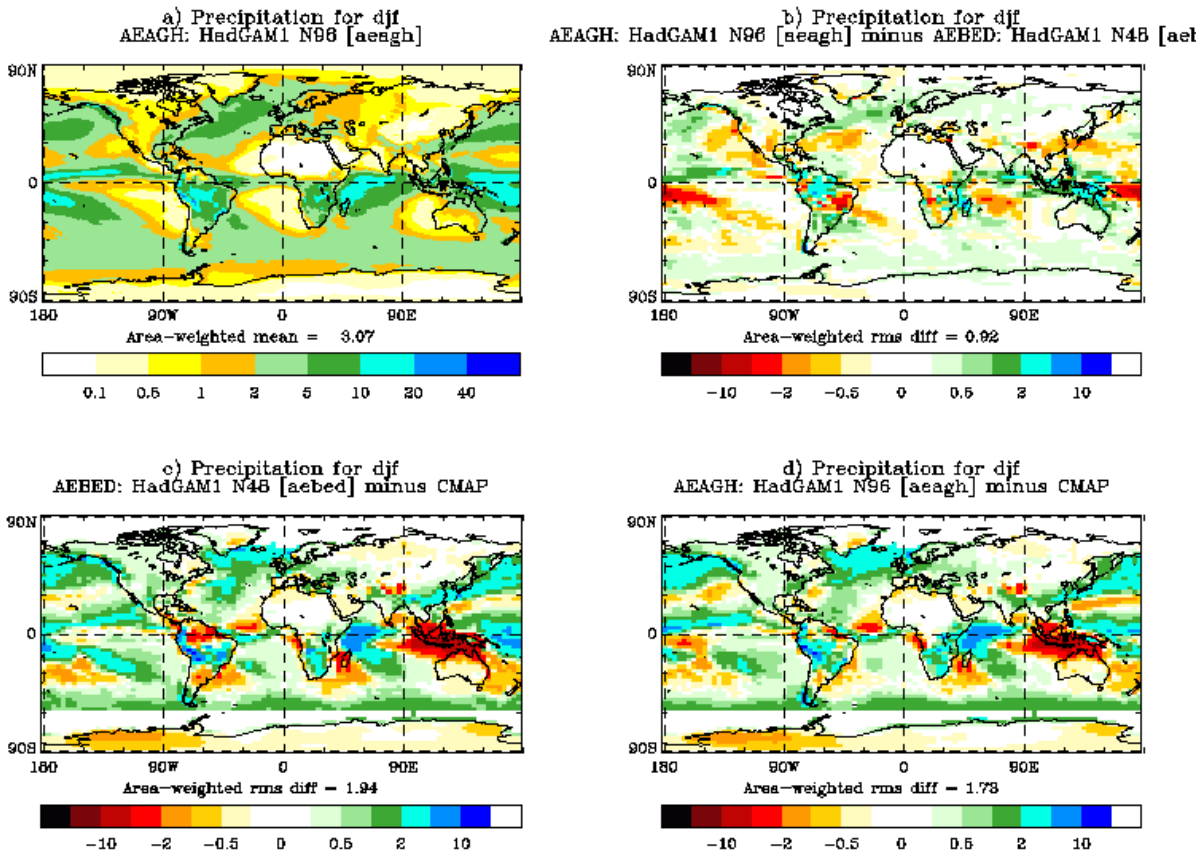

Figure 29: Precipitation in HadGAM1 at N96 resolution and differences from N48 and CMAP

Figure 30 shows precipitation differences between HadGEM1 and HadGAM1 and CMAP climatology. The error patterns are rather different between the coupled and atmosphere-only versions, particularly around Indonesia where there is a positive bias rather than a negative one, and over the western equatorial Pacific where there is a negative bias. This was also found to be the case in HadCM3, where it was associated with a warm SST error around the maritime continent and a cold equatorial Pacific (Inness and Slingo, 2003). A similar pattern of SST errors occurs in HadGEM1, although the errors around the maritime continent are smaller and the equatorial cooling is larger. The changes in the pattern of precipitation in both coupled models arise through the lack of convection over Indonesia and the excessive easterly wind stresses over the equatorial Pacific in the atmosphere components. The lack of convection over Indonesia allows warmer SSTs to develop, which then promote additional convection locally. At the same time, the excessive easterly wind stresses promote upwelling of cold water through Ekman divergence, resulting in a cold equatorial SST anomaly which helps to confine convection to the maritime continent. A new balance is reached whereby significant convection in the region can occur. This then drives a stronger Walker circulation which strengthens further the low-level easterly trade winds over the equatorial Pacific.

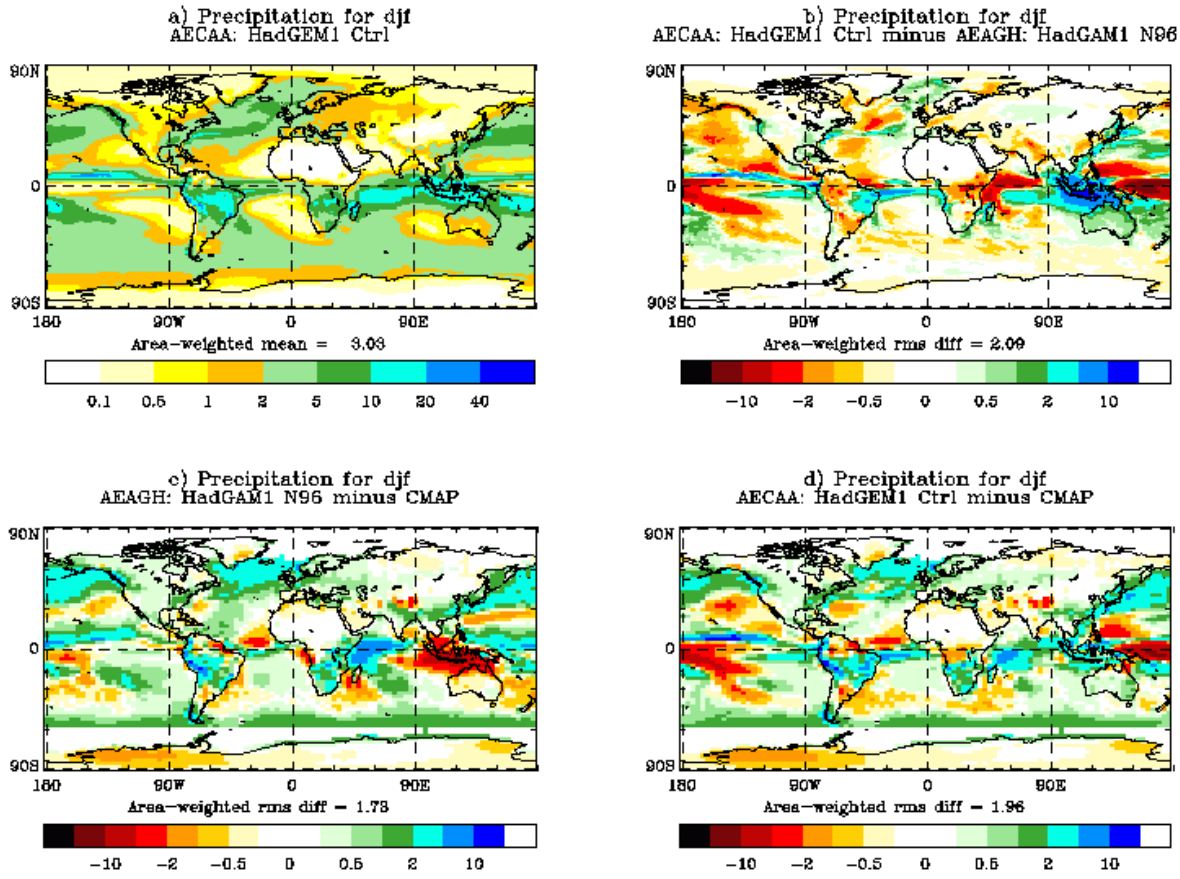

Figure 30: Precipitation in HadGEM1 (N96) and differences from HadGAM1 (N96) and CMAP

6. Aspects of variability

6.1 Analysis of Northern Hemisphere Blocking in HadGAM/GEM1

A blocking index has been used to identify blocking highs in the model simulations and ECMWF Re-Analyses. The index used is based on the Tibaldi and Molteni (TM) index (Tibaldi and Molteni, 1990), as used in an AMIP study of blocking, D'Andrea et al (1998). The TM index identifies blocking when geostrophic easterlies are identified in the region of the mid-latitude storm track, at 50N. The index used here uses a variable latitude to define the location of the mid-latitude storm track, as in Pelly & Hoskins (2003), rather than a fixed latitude. A blocking episode is diagnosed when more than 15 degrees of longitude is blocked for at least 4 days, within 10 degrees of longitude of that point.

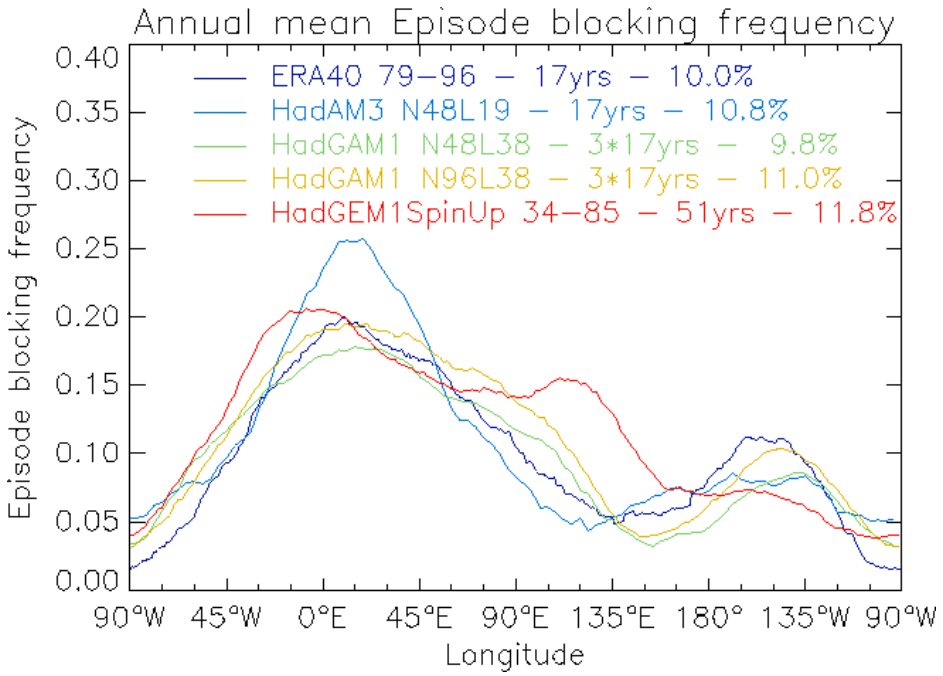

Figure 31. Annual mean episode blocking frequency for different models against ERA-40. For HadGAM1, 3 17-year ensemble members have been analysed and the results averaged.

The two preferred areas of NH blocking are clear from the annual mean blocking episode frequencies in Figure 31. Two peaks can be identified at about 0E and about 150W, corresponding to the ends of the Atlantic and Pacific storm tracks. HadAM3 correctly identifies the two regions, but produces too much blocking in the Euro-Atlantic region and the West Pacific. These inaccuracies are not present in the HadGAM1 simulations. The marked decrease in blocking in the north Atlantic region between HadAM3 and HadGAM1 is consistent with the reduction in the high PMSL bias over this region seen in Section 5.1, although a similar decrease in blocking is not seen in the Pacific region despite a reduction in the positive PMSL bias there too. HadGEM1 does not clearly identify the Pacific area of high blocking frequency. HadGEM1 also produces too much blocking in the region 75-165E.

In HadGAM1 the episode blocking frequency is increased at high resolution. This is expected, since synoptic-scale variability should increase with resolution, as

was seen with the increase in transient eddy kinetic energy shown in Section 4.3. In particular, the Pacific peak shows much better agreement with ERA in HadGAM1 at N96.

We now consider each season individually (see Figure 32):

Winter [DJF]: HadAM3 misplaces the Pacific peak to the west, but is otherwise a reasonable match to ERA. HadGAM1, at both resolutions, has too much blocking in the region 45-120E. The position of the Pacific peak is slightly to the east of ERA, and its strength is high variable between the different resolutions and ensemble members. HadGEM1 completely fails to produce a peak in blocking frequency in the Pacific region, as was seen in the annual mean blocking frequency (Fig. 31).

Spring [MAM]: All of the model generally perform rather better in this season. However, HadAM3 and HadGAM1 N48 have the Pacific peak displaced to the east, whereas HadGAM1 N96 is better. HadAM3 also produces too much blocking in both the Euro-Atlantic and Pacific regions. There is little difference between the two resolutions of HadGAM1, which both tend to produce too much blocking on the eastern flank of the Euro-Atlantic region and slightly too little in the western Pacific. This has the effect of producing a small apparent eastward shift in the HadGAM1 distributions compared with ERA. HadGEM1 has produced too much blocking between 45E and 180E, and once again produce no defined peak in the Pacific blocking frequency.

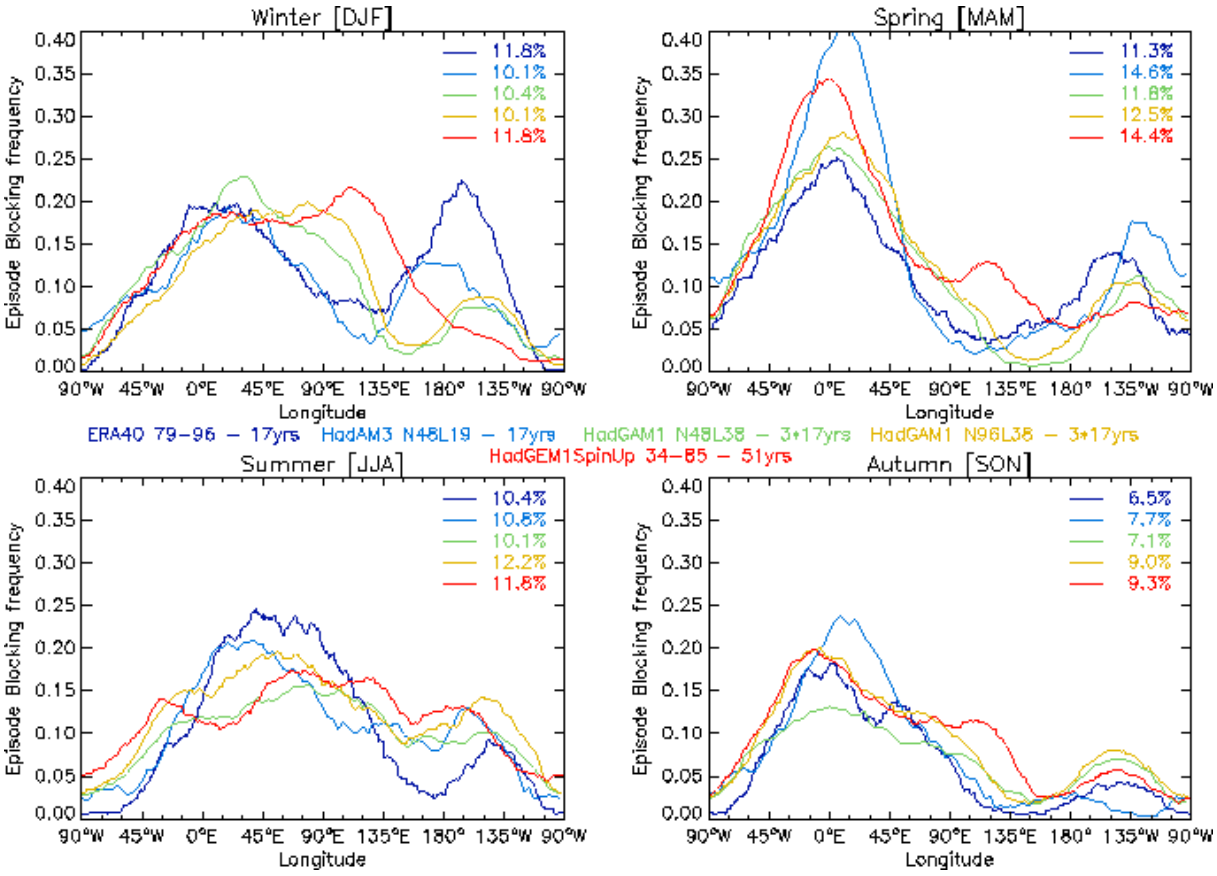

Figure 32: Seasonal mean episode blocking frequencies

Summer [JJA]: This season is the worst modeled overall. All models produce too much blocking in the Pacific region and too little over the Euro-Atlantic region, with the result that the sharp contrast between the two regions seen in ERA is not seen in the models. HadAM3 and HadGAM1 N96 are best and HadGEM1 the worst.

Autumn [SON]: In HadAM3 the Euro-Atlantic peak is overestimated and shifted to the east of that in ERA. HadGAM1/GEM1 position the Pacific blocking correctly. HadGAM1 N48 does not produce enough blocking in the Euro-Atlantic region, whereas HadGAM1 N96 and HadGEM1 represent this peak well. Both HadGAM1 and HadGEM1 produce too much blocking between 60-135E. The Pacific peak in ERA is small in this season, but is represented well by HadGAM1 and HadGEM1. It is shifted to the west in HadAM3.

The analysis thus far has used an episode definition of a block, which takes into account the spatial and temporal scales of the feature identified by the index. A simpler method that is often used is to consider the instantaneous existence of a block and not to apply any spatial or temporal definitions. This has been done in previous studies, e.g. Pelly (2001). It is useful to compare the instantaneous index with the episode blocking index. In addition, a sector blocking index can be defined which identifies block extending over at least 15 degrees of longitude. The three indices are compared in Figure 33.

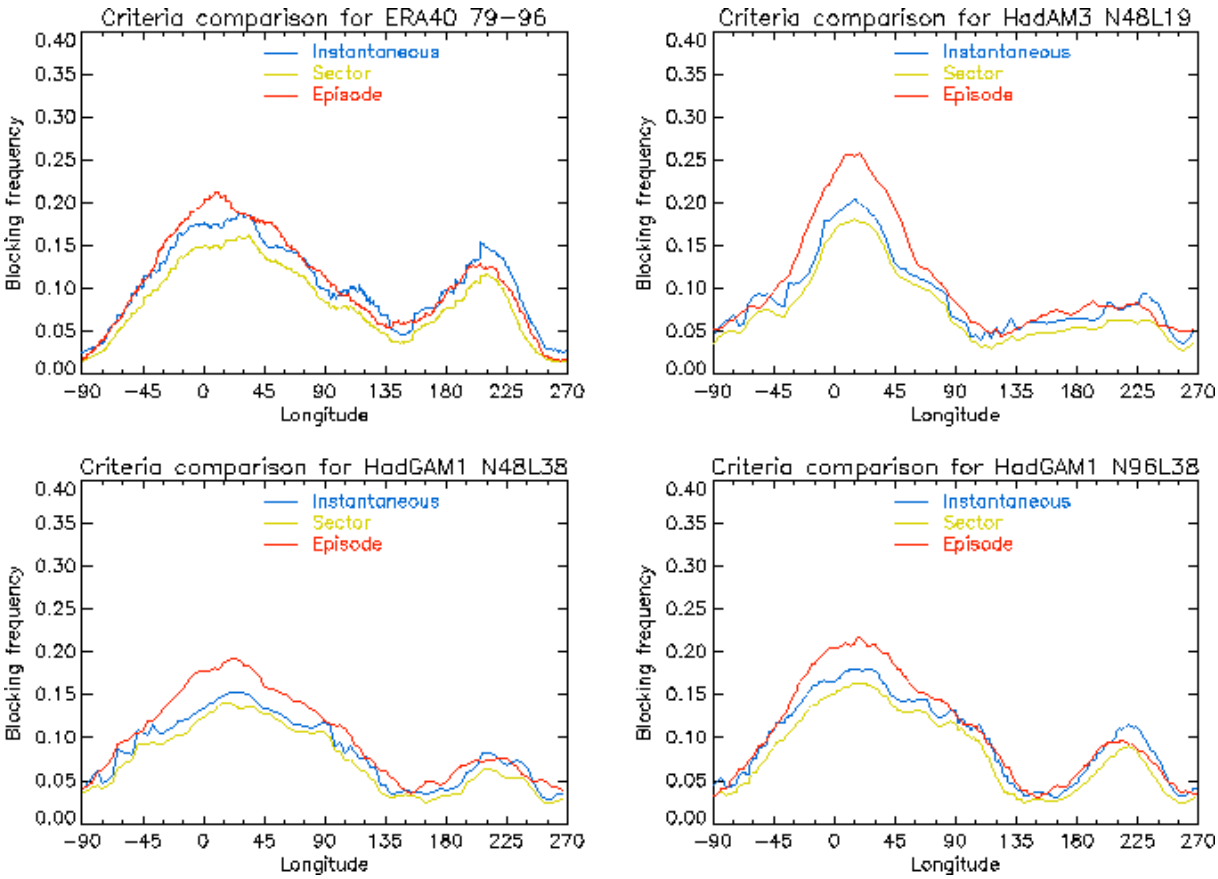

Figure 33: Blocking indices in ERA-15, HadAM3, HadGAM1 at N48 and HadGAM1 at N96 resolution: blue – instantaneous, yellow – sector, red – episode.

The difference between the blue and yellow lines is that some of the features identified by the instantaneous index have a small scale and do not extend over 15 degrees of longitude or more. They are therefore rejected as not blocking a 'sector', and are not included in the yellow line. This implies that the yellow line cannot be above the blue line.

The difference between the yellow line and the red line is that some of the spatially large features will not persist for enough time [4 days] to be considered a synoptic block. Therefore the red line only includes those features that persist for four or more days. However, since the location of the block may change, due to advection by the zonal wind, a longitude is said to be episode blocked if there is sector blocking within 10 degrees for at least four days. Therefore the red line could be above the yellow line since episode blocks may be diagnosed and counted at longitudes which themselves are not blocked at all the times.

The ERA plot shows that there is less sector blocking [yellow] than instantaneous blocking [blue] and that the amount of episode blocking [red] is greater than instantaneous blocking. Therefore, although there are some sector blocks that do not fulfill the persistence criteria to be considered blocking episodes, this is more than compensated for by the extra counting of the episode blocks for the reasons explained above.

However, something very different is seen when looking at the model data. In this case, particularly for HadAM3, there is a lot more episode blocking than either sector or instantaneous blocking over the Euro-Atlantic region. The difference between sector and instantaneous blocking is comparable to that of ERA, so the relative change in episode blocking must be explained by a difference in the persistence characteristics or the spatial movement of the blocks. If short blocks in HadAM3 were more stationary than blocks in ERA then they would affect a greater number of longitudes than if they were more mobile since a greater number of longitudes would be within 10 degrees for the qualifying period of four days. Alternatively, if long-lived blocks were more mobile, albeit at a slow pace, then they could sweep out a greater extent as being blocks. Also if HadAM3 does not create the short-lived features present in ERA then this could explain the difference.

Figure 34 shows the instantaneous, sector and episode blocking in HadGEM1 (N96). The instantaneous blocking frequency is reduced in the Atlantic and Pacific regions and increased between 90-180E compared with HadGAM1 (N96). This is consistent with a weakening of the northern hemisphere storm track in the coupled model (see Section 6.2). The difference between episode and instantaneous blocking is reduced over the Euro-Atlantic region in HadGEM1 relative to HadGAM1. All three types of blocking are reduced over the Pacific in the coupled model.

One of the most notable features found thus far is the dramatic loss of blocking in the winter Pacific in HadGEM1. Further analysis has suggested that this is connected with the cold bias in the equatorial Pacific SSTs. In particular the same loss of Pacific DJF blocking is found in the HadGAM1 runs when the individual season blocking frequencies are analysed and the season of the strong 1988/89 La Nina identified.

It can be seen in Figure 35, that, for all the HadGAM1 N96 runs, the year of the La Nina [when the equatorial Pacific SST are abnormally cold] coincides with the year when Pacific DJF blocking is at a minimum, although this is not the case when looking at ERA. This suggests that there is a mechanism in the model which is

making the Pacific storm track, and therefore blocking, sensitive to cold anomalies in the equatorial Pacific.

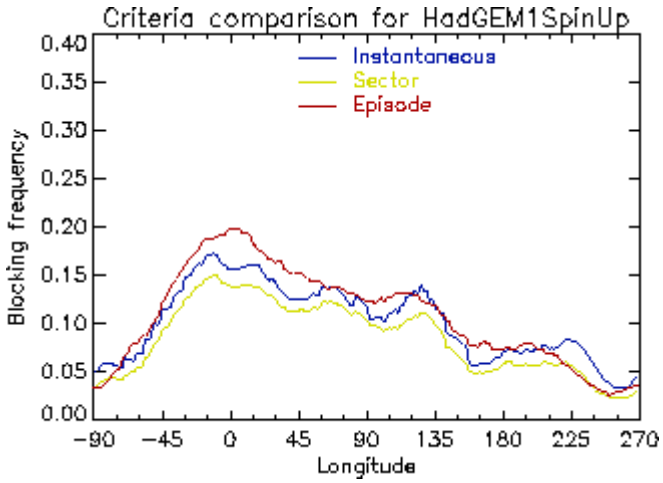

Figure 34: Blocking indices in HadGEM1: blue – instantaneous, yellow – sector, red – episode

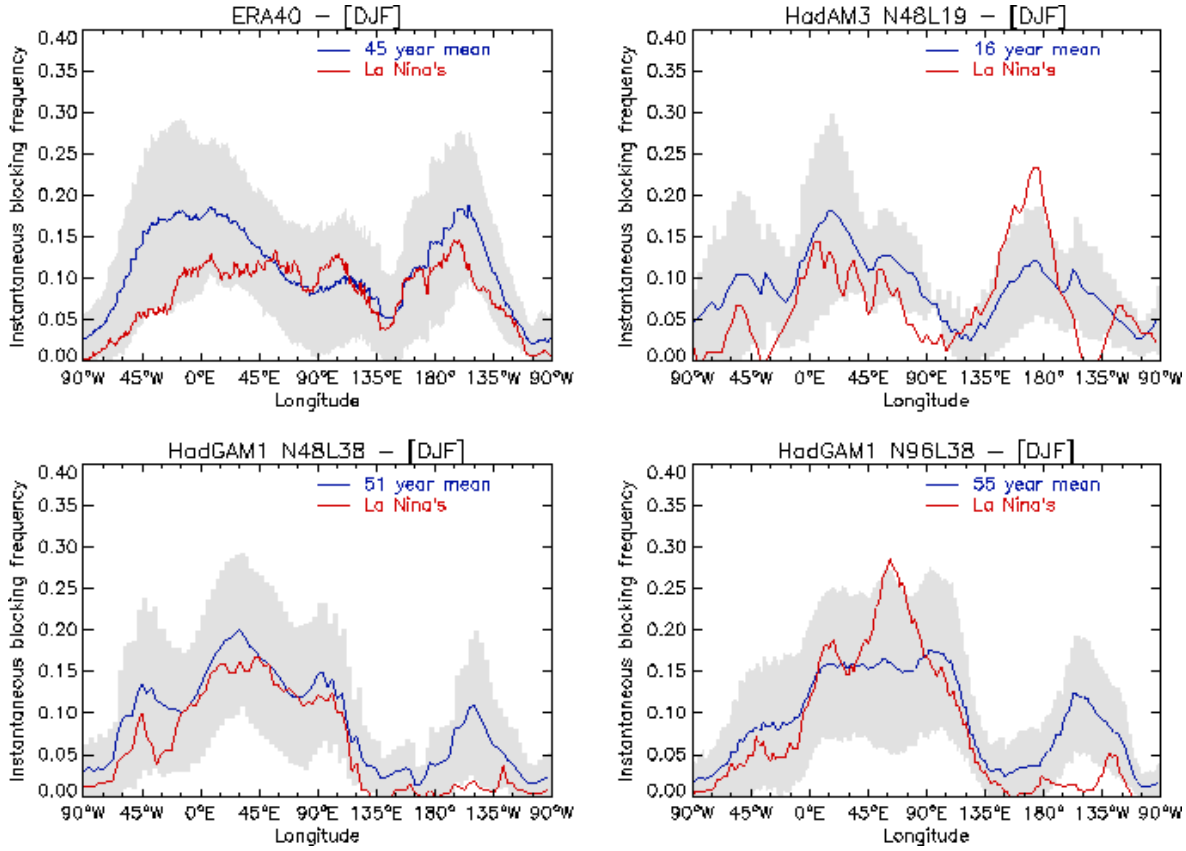

Figure 35. Plots of DJF mean blocking frequency (blue line) for HadAM3, HadGAM1 (N48 and N96) and ERA with the results from La Nina years shown in red. Grey shading indicates ± 1 standard deviation of results from each individual year against the mean over all years. Note that HadGAM1 results are taken from 3-member ensembles of 17-year runs.

6.2 Analysis of storm tracks in HadGAM/GEM1

Another important measure of variability is the storm tracks. We use two different methods to analyse storm track activity. The first is the standard deviation of

24-hourly instantaneous geopotential heights at 500 hPa which have been filtered between 2 and 6 days. This isolates the high frequency eddy activity in the mid-troposphere, which has been shown to be a good measure of the frequency and location of the passage of synoptic weather systems. The second method is that of feature-tracking. Low pressure centres are identified in 6-hourly instantaneous fields and tracked from one 6-hour period to the next. The tracks are recorded over each season and then processed further to derive information on the mean speed of cyclones, where they start, i.e. their genesis, and where they decay, i.e. lysis. The use of this method for analysing storm tracks was originated by Hoskins and Hodges (2002) and the programs used in our analyses have been provided by Kevin Hodges.

6.2.1 Results from band-pass filtering method

Figure 36 shows the standard deviation of band-pass filtered 500 hPa geopotential heights from ERA in the northern and southern hemispheres. Two major areas of activity are seen in the northern hemisphere, one over the Pacific and the other centred over the western Atlantic. The cyclogenesis regions tend to lie towards the western extremities of the eddy activity maxima, and the tracks of depressions run close to the major axes. The cyclones decay and fill mainly towards the eastern extremities where the levels of eddy activity are seen to decline. In the southern hemisphere, the storm track lies mainly over the sea and is more uniform, although maxima are seen in the southern Atlantic and Indian Oceans.

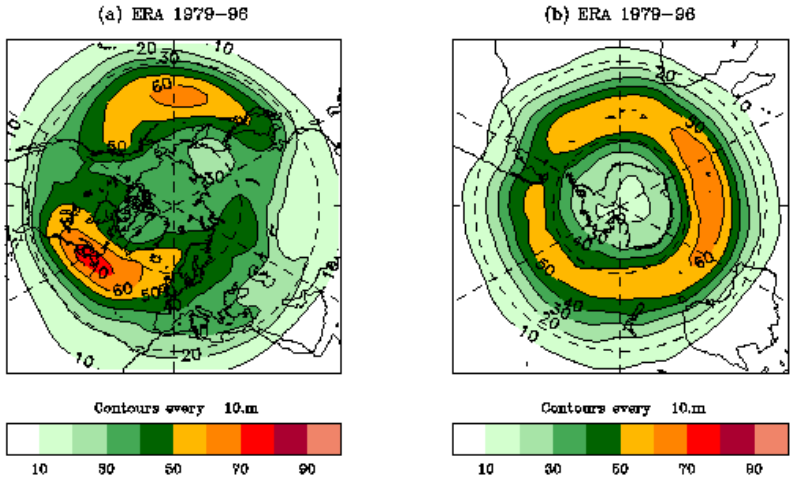

Figure 36 Standard deviation of band-pass filtered 500hPa height (m) from ERA for DJF 1979 - 1996 for Northern and Southern Hemisphere**s.**

Figure 37(a and b) shows similar analysis of HadAM3 and HadGAM1 at N48 resolution. The overall position of the tracks in both models is good in both hemispheres and in both models compared with results from ERA, although difference plots (not shown) reveal a slight equatorward bias in both models. This is consistent with the zonal wind plots shown in Figure 5. The maxima in strength occur at very similar locations to those in ERA, but in general the eddy activity is underestimated in both models, and further in HadGAM1 compared with HadAM3. In both models the Atlantic track does not extend far enough into Europe, and the

Pacific track extends too far across the East Pacific, particularly in HadAM3. In the southern hemisphere the track does not extend far enough around from both east and west south of South America.

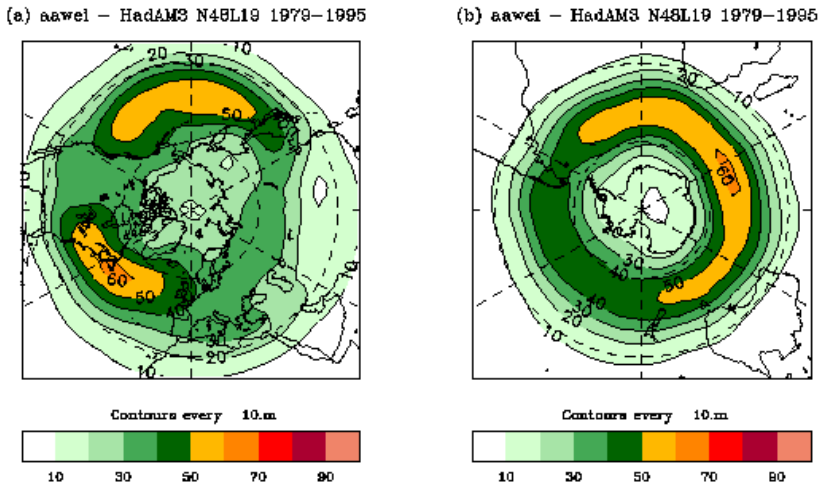

Figure 37(a): Standard deviation of band-pass filtered 500hPa height (m) from HadAM3 N48 for DJF 1979 - 1995 for Northern and Southern Hemispheres.

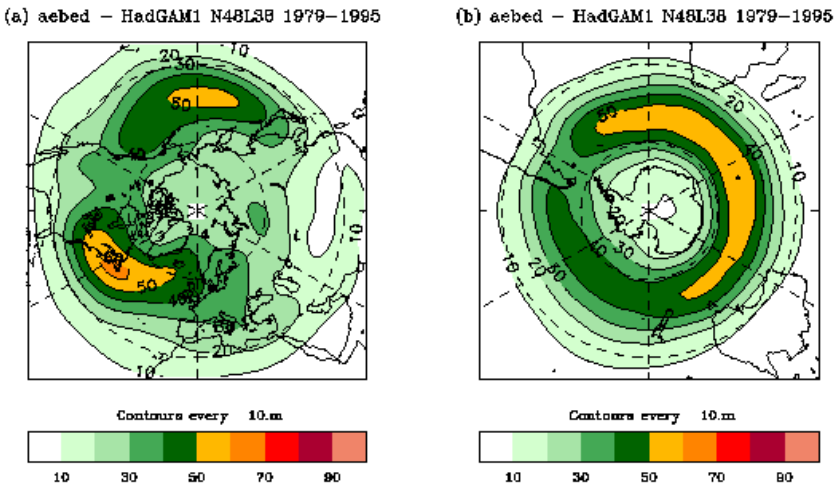

Figure 37(b): Standard deviation of band-pass filtered 500hPa height (m) from HadGAM1 N48 for DJF 1979 - 1995 for Northern and Southern Hemispheres.

Typically, mid-latitude storms are of order 1000km across, whereas at N48 resolution, the grid-length is ~300km at mid-latitudes. This means the model will attempt to model a storm using a grid of at most 4x4 points. Increasing the horizontal resolution, e.g. by doubling it to N96, allows improved dynamical representation of eddies and should allow individual storms to be modelled more realistically (although even N96 is probably not sufficient for this). Pope and Stratton (2002) showed that increasing resolution in HadAM3 from N48 to N72, N96 and N144 resulted in a marked improvement in the position and strength of the storm tracks. Storms were generally stronger and positioned closer to the pole. They also extended further into northern Europe and America. They also showed that the extension of the storm tracks, in particular, was associated with the improved resolution of orography in the higher resolution experiments.

Figure 38 shows the results of the increase from N48 to N96 resolution in HadAM3 and HadGAM1. Comparison with Figure 37 shows a poleward movement and a strengthening of the storm tracks in both models, improving agreement with ERA. The magnitude in HadGAM1 remains slightly less than HadAM3 in the northern hemisphere but greater in the southern hemisphere, and in both cases is rather closer to ERA. The north Atlantic track extends further into Europe in both models but particularly in HadAM3. It also extends further into western North America in both models, worsening agreement with ERA in this case.

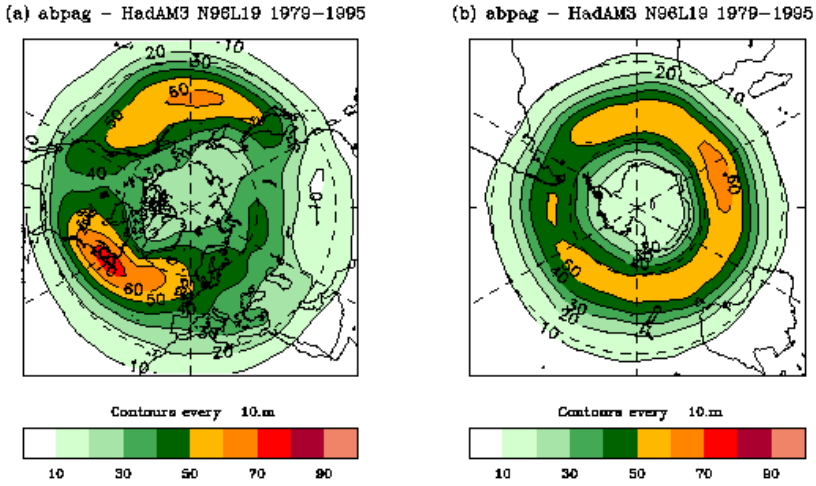

Figure 38(a): Standard deviation of band-pass filtered 500hPa height (m) from HadAM3 N96 for DJF 1979 – 1995 for Northern and Southern Hemispheres.

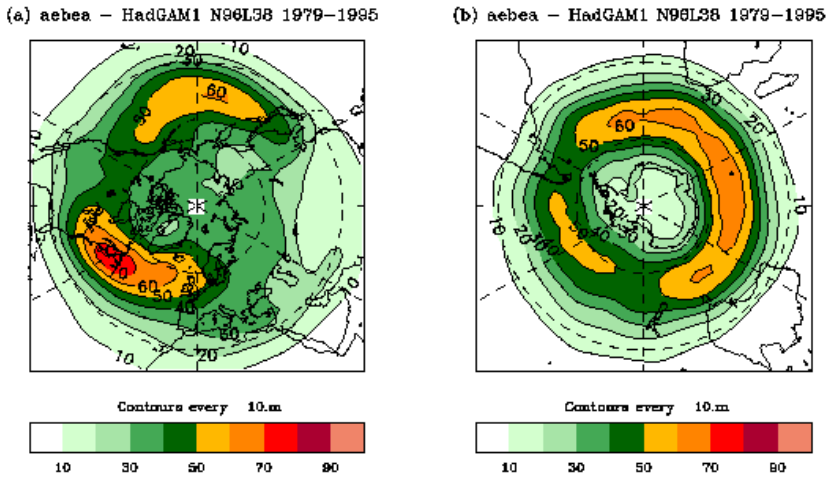

Figure 38(b): Standard deviation of band-pass filtered 500hPa height (m) from HadGAM1 N96 for DJF 1979 - 1989 for Northern and Southern Hemispheres.

Figure 39 shows the results from the coupled versions of the two models (note that HadGEM1 is at N96 resolution and HadCM3 at N48 resolution). Coupling each model to an ocean model results in a weaker north Atlantic storm track and a slightly stronger north Pacific one. The excess eastward extension of the Pacific track in HadAM3 is reduced in HadCM3 but is increased in HadGEM1. In addition, the Pacific track lies further north in HadGEM1 than in HadGAM1, worsening agreement with ERA. There is very little impact of coupling on the southern hemisphere storm track

in HadAM3/CM3, but that in HadGEM1 is stronger over the south Pacific and weaker over the south Atlantic than in HadGAM1.

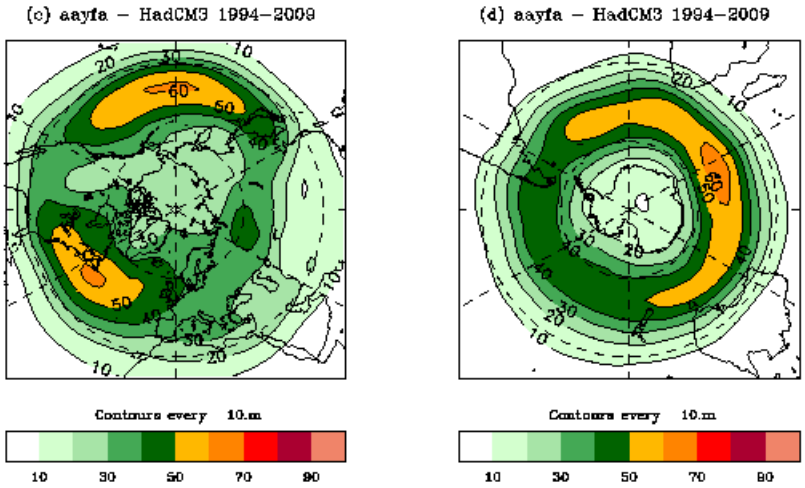

Figure 39(a): Standard deviation of band-pass filtered 500hPa height (m) from HadCM3 N48 for DJF 1994 - 2009 for Northern and Southern Hemispheres.

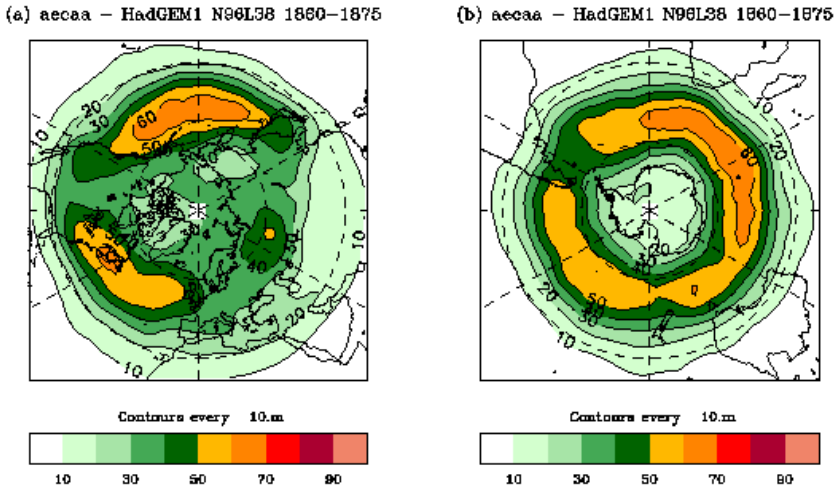

Figure 39(b): Standard deviation of band-pass filtered 500hPa height (m) from HadGEM1 N96 for DJF (15 years) for Northern and Southern Hemispheres.

6.2.2 Results from feature-tracking method

The feature tracking analysis in this study only looks at mean sea level pressure and so concentrates on the surface features of the storms. The previous sections tended to concentrate on the characteristics of the storms in the lower and mid-troposphere. This may explain why some of the results from the feature analysis differ from the band pass filtered analysis.

Figure 40 shows the mean cyclone strength obtained from tracking analysis of PMSL in the northern hemisphere in DJF from HadGAM1 and HadAM3 at N96 and N48 resolution and from ERA. Comparing first the results of this method from ERA with those from the band-pass filtering method shown in Figure 36, we see that position of the maximum cyclone strength is slightly poleward of the maximum in eddy activity. This is also the case in the southern hemisphere (not shown), though it

is more marked. This illustrates the different features of the storm track which each of these methods highlights. There is a natural tendency for centres of low pressure at the surface to be displaced poleward of the vortex centre. In the southern hemisphere, where the surface properties are more uniform and the storm track more continuous, cyclones tend to spiral polewards across the storm zone.

Figure 40 shows that both models reproduce this difference between the results from the two analysis methods. However, in this case, the results from HadGAM1 at N48 are closer to ERA than those from HadAM3, although the Pacific maximum is located too far to the west, and the Atlantic track does not extend far enough into Europe. At N96, the mean cyclone strength and the track extent in HadGAM1 is in much better agreement with ERA, although the extension of the Pacific and Atlantic tracks into North America and Europe is still limited compared with ERA. In HadAM3, although the mean cyclone strength and track extent are also improved at N96 resolution, the values remain smaller than both HadGAM1 and ERA. This is in marked contrast with the relative change in the model results with resolution using the band-pass filtering method.

Track analysis of HadGEM1 at N96 resolution has not been possible due to a lack of 6-hourly data. However, analysis of development versions of HadGEM1 reveals a similar weakening of the northern hemisphere storm track in the coupled model as was seen with the band-pass filtering method, although in this case it is weaker in both the Atlantic and Pacific regions. It is not clear why the coupled model should behave in this way, although there is a suggestion from the blocking analysis (Section 6.1) that it may be linked to the development of cold tropical SST errors. The differences in variability across a range of time and space scales in the models, and using a number of different fields, are currently under investigation.

Figure 41 shows analysis of genesis density obtained from the tracking method. As mentioned in section 6.2.1, the main cyclogenesis regions tend to lie towards the western extremities of the storm tracks. However, the ERA data show several distinct areas of high genesis density across the Pacific, North America and the western North Atlantic. The high genesis density over the central Pacific may indicate secondary cyclogenesis. The genesis densities are represented fairly well by both models, although genesis over the Pacific is underestimated, particularly at N48, indicating perhaps that secondary cyclogenesis is less frequent at this resolution. This is improved at N96 in HadGAM1 (Fig. 41c), but not in HadAM3 (not shown). In fact there is a slight reduction in cyclogenesis density over the Pacific in HadAM3 at N96 (Stratton, 2004b). HadGAM1 at N96 also captures more of the genesis observed in the Mid-Atlantic than the N48 model, but at both resolutions, and in HadAM3, the cyclogenesis over the north Atlantic and northern Eurasia is underestimated. The Mediterranean genesis regions are represented reasonably well in both model versions.

The cyclones decay and fill mainly towards the eastern extremities of the storm tracks (Figure 42). This is captured fairly well by the models, although at N48 it is generally underestimated. In HadGAM1 at N48 the lysis in the Pacific is confined unrealistically to one major region in the East Pacific. Increasing the resolution to N96 improves the lysis density and distribution in both models.

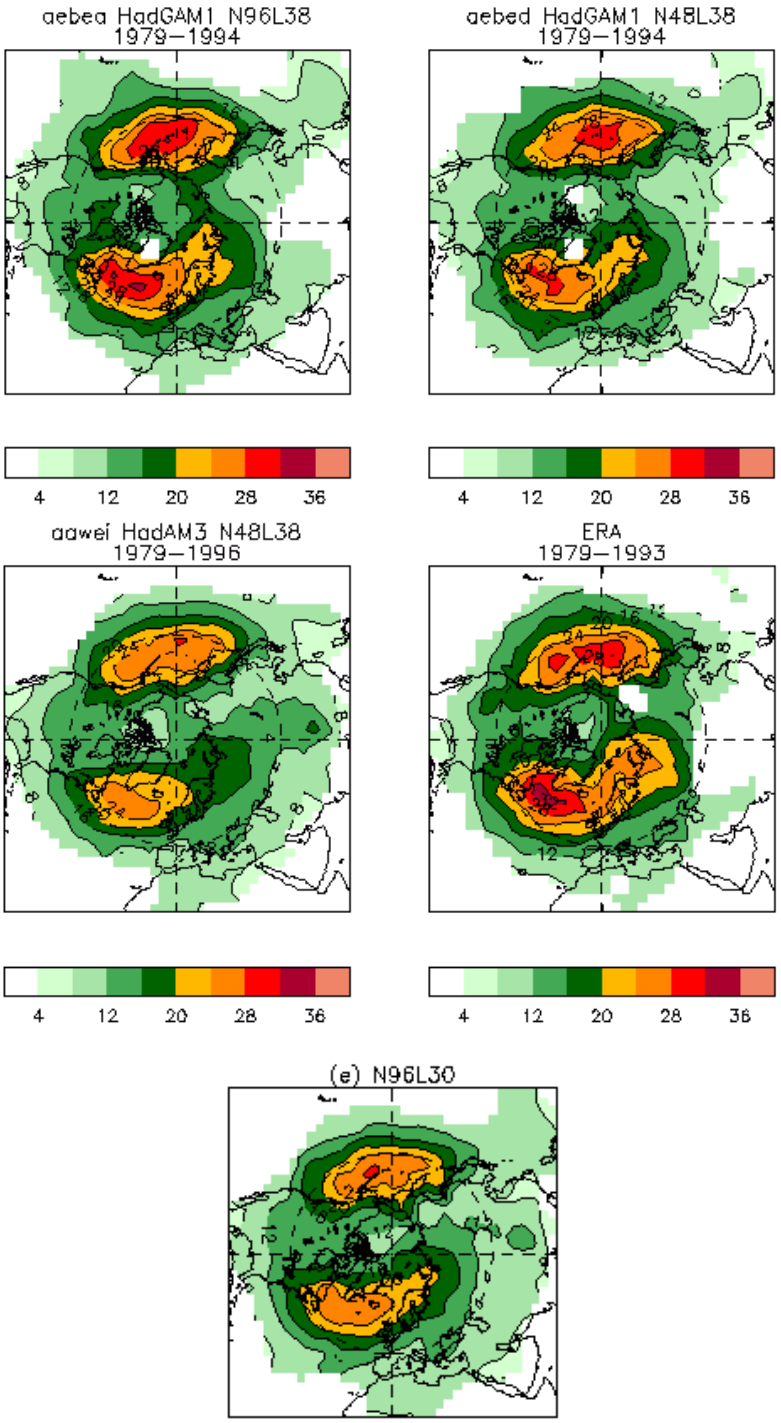

Figure 40: Cyclone Strength in hPa from TRACK analysis of MSLP for DJF for the Northern Hemisphere for HadGAM1 N96L38, HadGAM1 N48L38, HadAM3 N48L30, ERA and HadAM3 N96L30

6.3 Synoptic variability over Europe

The purpose of this work is to construct an objective method to assess the statistics of occurrence of pre-specified weather patterns over the European / North-Atlantic area in HadGAM and HadGEM climate simulations and compare the results with observed statistics based on ECMWF ERA40 re-analysis data. The 17-year HadGAM1 N96 run and 17 years of HadGEM1 (N96) will be compared with two 17-year sections of ERA40 data (1962-1978, 1979-1995).

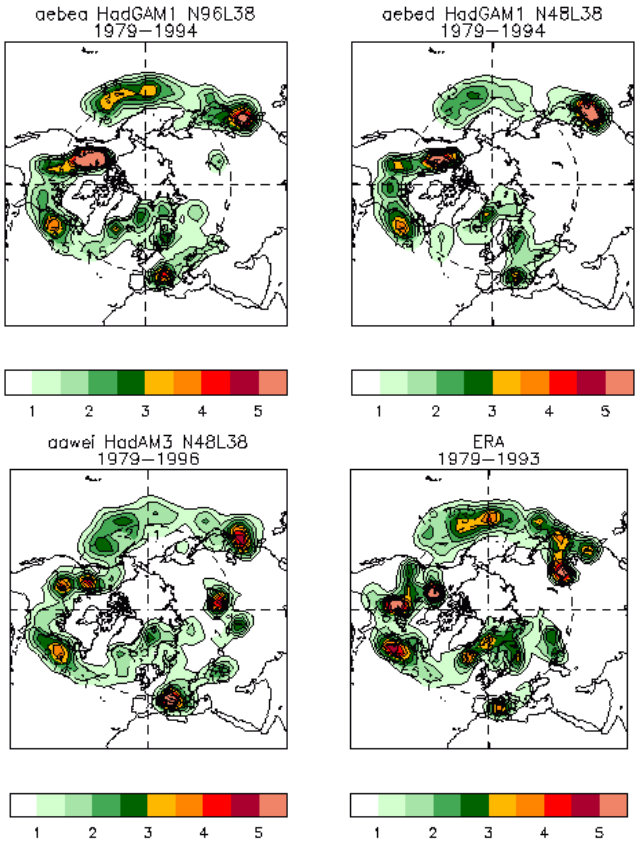

Figure 41: Genesis Density (scaled) from TRACK analysis of PMSL for DJF for the Northern Hemisphere for HadGAM1 N96L38, HadGAM1 N48L38, HadAM3 N48L30 and ERA.

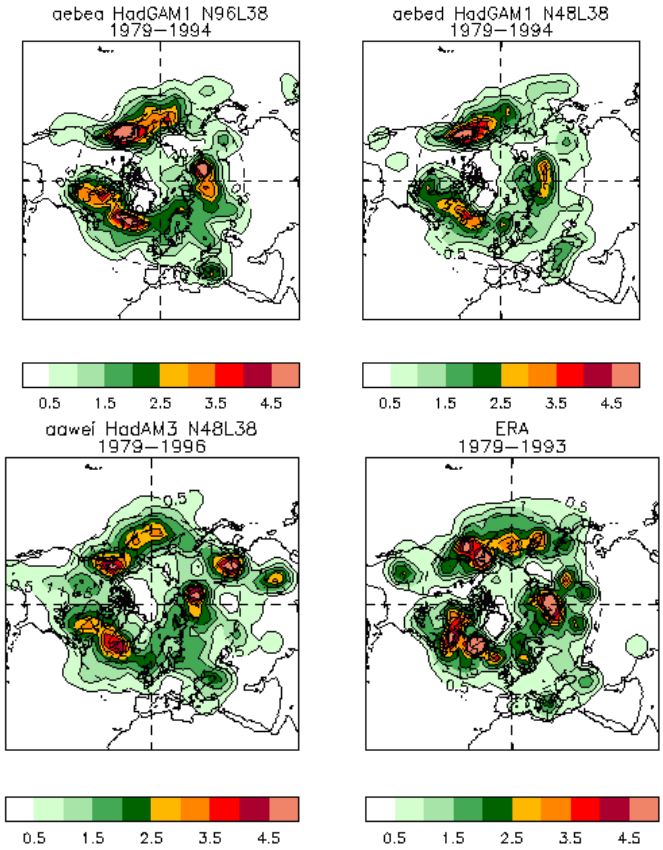

Figure 42: As Fig. 41 but for lysis density

To assess a climate model's ability to reproduce aspects of synoptic-scale variability, an objective method is required. An example of a technique that is frequently used is Empirical Orthogonal Function (EOF) analysis. This yields a set of orthogonal spatial patterns, accounting successively for the maximum possible fractions of the variance in the data. Illustrating this technique, the first 4 area-weighted EOFs of 17-year daily mean PMSL analysis sets for ERA40 and the climate simulations listed above are shown for the winter half-year in Fig. 43. The EOF 1 patterns in HadGAM/GEM1 are similar, showing a single anomaly centre to the west of the British Isles, albeit with some shift in location. This pattern is found in the earlier ERA40 period's EOF 1. However, EOF 1 of the later ERA period is quite different, resembling an North Atlantic Oscillation (NAO)-like pattern. The EOF 4 pattern is rather similar in all cases, but on the whole, the 3 primary modes show significant relative rotation with respect to each other.

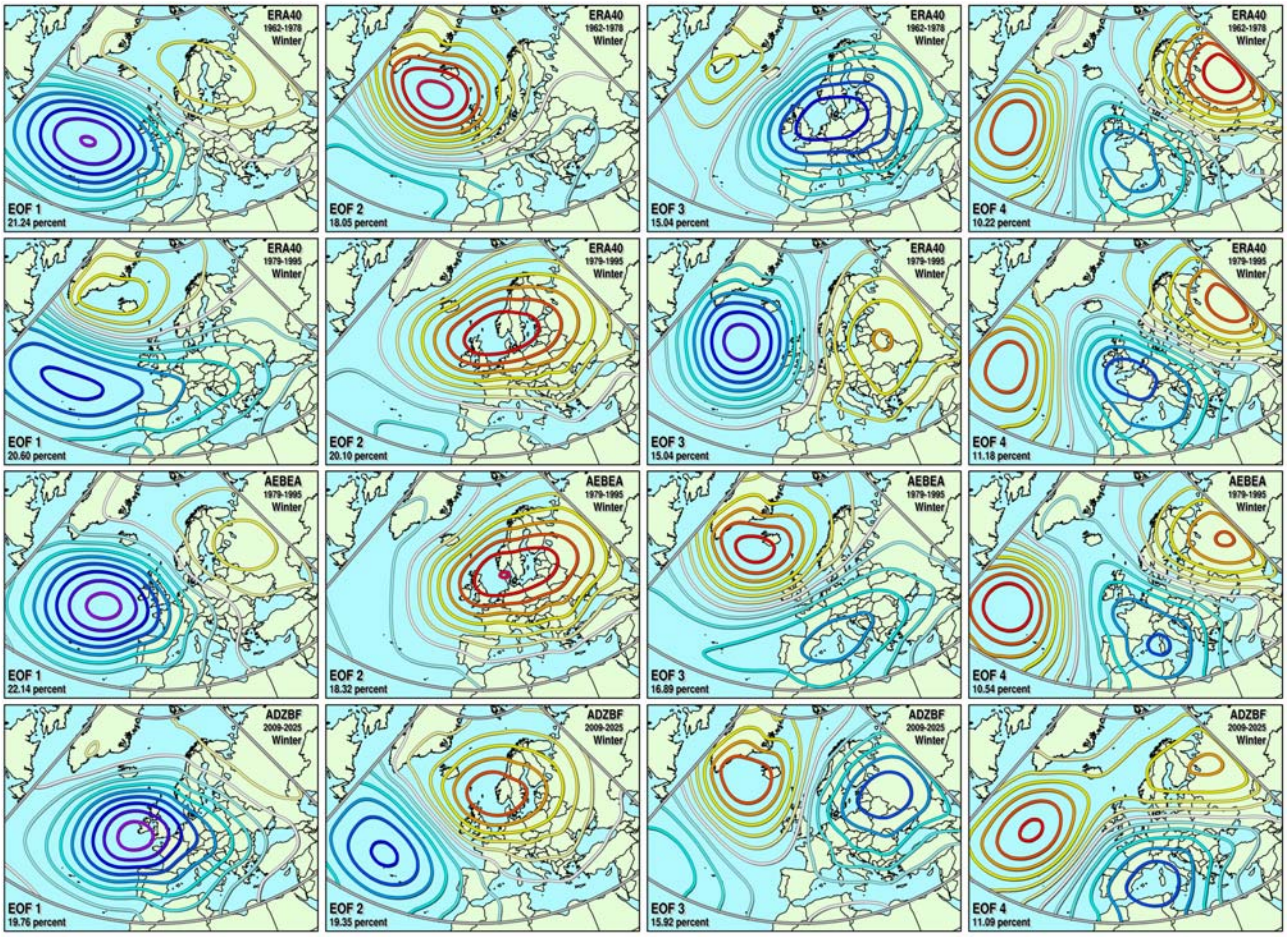

Fig. 43: The first four EOF patterns (left to right) of MSLP in Winter for (top to bottom) ERA40 (1962-1978), ERA40 (1979-1995), HadGAM1 (labelled AEBEA) and HadGEM1 (labelled ADZBF). The respective percentages of the variances accounted for are plotted in the lower left-hand corner.

While they may be mathematically satisfying, the EOF patterns have only limited synoptic meaning. Furthermore, EOFs assume both positive and negative sign, although there is no physical reason for this constraint. EOF analysis and other similar techniques are clearly useful for bringing out aspects of the variability in single datasets, but difficulties clearly arise when different model simulations and/or

re-analysed climate data are to be compared with each other. Principal Component time series can be produced for each dataset and compared, but the patterns which these components refer to are never identical to each other.

Clearly, there would be advantages in having a fixed set of typical weather patterns to classify the actual synoptic situation against, providing a meaningful set can be constructed. Probably the best classification system available is the Grosswetterlagen (GWL) catalogue, originally conceived by Baur et al. (1944), improved upon and later revised by Hess and Brezowsky (1977), recently updated by Gerstengabe et al. (1999) and since maintained by the German Weather Service (DWD). The 29 GWL regimes are readily identifiable large-scale circulation patterns involving the whole of Europe and the N.E. Atlantic, with its primary focus on central Europe. A daily catalogue of subjectively-assessed GWLs has been constructed retrospectively back to 1881. The 29 GWL types are defined in Table 3, noting that the terms anticyclonic and cyclonic refer to the local bias over Central Europe within each clearly-defined large-scale pattern.

GWL	Definition	GWL	Definition
01 WA	Anticyclonic Westerly	16 HB	High over the British Isles
02 WZ	Cyclonic Westerly	17 TRM	Trough over Central Europe
03 WS	South-Shifted Westerly	18 NEA	Anticyclonic North-Easterly
04 WW	Maritime Westerly (Block E. Europe)	19 NEZ	Cyclonic North-Easterly
05 SWA	Anticyclonic South-Westerly	20 HFA	Scandinavian High, Ridge C. Europe
06 SWZ	Cyclonic South-Westerly	21 HFZ	Scandinavian High, Trough C. Europe
07 NWA	Anticyclonic North-Westerly	22 HNFA	High Scandinavia–Iceland, Ridge C. Europe
08 NWZ	Cyclonic North-Westerly	23 HNFZ	High Scandinavia–Iceland, Trough C. Europe
09 HM	High over Central Europe	24 SEA	Anticyclonic South-Easterly
10 BM	Zonal Ridge across Central Europe	25 SEZ	Cyclonic South-Easterly
11 TM	Low over Central Europe	26 SA	Anticyclonic Southerly
12 NA	Anticyclonic Northerly	27 SZ	Cyclonic Southerly
13 NZ	Cyclonic Northerly	28 TB	Low over the British Isles
14 HNA	Icelandic High, Ridge C. Europe	29 TRW	Trough over Western Europe
15 HNZ	Icelandic High, Trough C. Europe		

Table 3: Definition of 29 Grosswetterlagen types

Here, pattern correlation techniques are used to create an objective GWL catalogue from ECMWF ERA40 data based on the synoptic principles of Hess and Brezowsky. The fields used for this are Geopotential Heights at 500 hPa (GH500) and Mean Sea-Level Pressure (PMSL). The first stage is to construct climate mean composites of these fields for each subjectively-determined GWL type, separate for the winter and summer half-years (sinusoidally weighted), following a statistical procedure to enhance these composites by removing spurious signals. Two nested domains are used for the analysis, the smaller domain being a circle of 1500 km radius surrounding central Europe, while the larger domain is determined by

examining the mean pattern variances of the 29 GWLs and encloses most of the north-east Atlantic and European continent. Five-day binomially filtered daily fields of the ERA40 or climate simulation are formed and correlated with the respective GWL composite fields, with the best correlation used to select the GWL for each day. Finally, since each regime must last for at least 3 days, according to the original definitions, events lasting for only 1 or 2 days in the initial correlation calculations are filtered out and systematically replaced by the most appropriate alternatives, respectively, based on comparing relevant correlation values.

The total number of days of occurrence of each GWL in HadGAM1 and HadGEM1 is compared with two 17-year periods of ERA40 in Table 4. Both climate simulations possess a quite realistic distribution of GWLs, with all 29 types occurring with a largely realistic frequency. The totals of each GWL per calendar month for any particular set have been correlated against those from each other set, with the correlation coefficients shown in Table 5.

While HadGEM1 correlates slightly better with either ERA40 set than HadGAM1, both models correlate less well with the earlier ERA40 set. For HadGAM1 this could demonstrate that the modelled response to 1979-1995 external constraints (such as SSTs) is in the correct sense so that the results are closer to the 1979-1995 observed variability than to the observed variability of the earlier period. However, the HadGEM1 run uses pre-industrial forcing from 1860, so one would not expect it to correlate better with either period from ERA40. The statistical significance of the results is currently under investigation. At this stage, it is sufficient to suggest that HadGAM1/GEM1 is capable of reproducing synoptic variability over Europe which is comparable with reality, at least in terms of weather regime distributions.

GWL	ERA40 62-78	ERA40 79-95	HadGAM	HadGEM
WA	513	622	591	618
WZ	671	717	610	616
WS	69	143	124	80
WW	533	609	607	611
SWA	434	554	335	363
SWZ	158	155	185	220
NWA	217	228	300	321
NWZ	268	268	303	233
HM	319	318	243	272
BM	491	456	559	468
TM	65	103	83	38
NA	73	80	49	36
NZ	91	107	151	145
HNA	134	133	202	219
HNZ	131	81	154	99

GWL	ERA40 62-78	ERA40 79-95	HadGAM	HadGEM
HB	171	193	134	145
TRM	248	201	220	172
NEA	173	171	171	136
NEZ	132	70	111	111
HFA	103	138	62	162
HFZ	212	117	171	167
HNFA	61	29	54	61
HNFZ	85	56	43	51
SEA	164	72	110	97
SEZ	95	103	108	99
SA	123	138	123	132
SZ	121	93	65	110
TB	115	110	113	140
TRW	239	144	139	198

Table 4: The total number of days of occurrence of each Grosswetterlagen in HadGAM1 and HadGEM1 compared with two 17-year periods of ERA40

	ERA 62-78	ERA 79-95	HadGAM	HadGEM
ERA 62-78	x	0.729	0.619	0.635
ERA 79-95	0.729	x	0.672	0.706
HadGAM	0.619	0.672	x	0.761
HadGEM	0.635	0.706	0.761	x

Table 5: Correlation coefficients between the totals of each GWL per calendar month in the different datasets

Given that each model has a slightly different GWL distribution from ERA40, it is possible to estimate the expected anomalies of any particular parameter for each model based on their circulation anomalies alone. For example, an easterly surface flow bias in winter over central Europe should result in a cold anomaly in surface temperature there - i.e. this would be the expected GWL-bias in surface temperature due to circulation changes alone. Expected GWL-biases are calculated by multiplying the GWL-frequency anomalies by the respective GWL-composite fields. Note that this method is empirical and does not take into account possible non-linearities in the amplitudes of the various regimes in each model.

The expected GWL-biases of PMSL, 1.5m temperature and precipitation are shown in Fig. 44 for the HadGAM1 and HadGEM1 for winter and summer, respectively. In winter, HadGAM exhibits a cyclonic bias over central Europe, resulting in a small positive surface temperature anomaly over south-eastern Europe (+0.1 K) and a cold anomaly over Scandinavia (-0.2 K), with a precipitation excess over north-western Europe and deficit over western Iberia (neither anomalies exceeding 0.2 mm/day). HadGEM1, on the other hand, has a stronger cyclonic anomaly over the western fringes of Europe which brings a positive surface temperature anomaly over south-western Europe of up to +0.3 K and a weak precipitation excess throughout this region.

In summer, both simulations show an anticyclonic anomaly to the west and north-west of the British Isles with a precipitation deficit there and a precipitation excess over south-western Europe. The anomalous north-westerly flow into Scandinavia results in a cold anomaly there which in HadGEM1 is about -0.2 K.

The actual measured error of such parameters in the model, relative to the observed climate, will be a superposition of these circulation-change effects and other ambient errors in the model physics. The biases in PMSL, 1.5m temperature and precipitation shown in Section 5 are rather different from those in Figure 44, suggesting that the contribution of the errors in synoptic variability is outweighed by systematic errors. However, although the biases indicated by the errors in local circulation pattern are very small, they do need to be taken into account when considering the regional climate responses of the model.

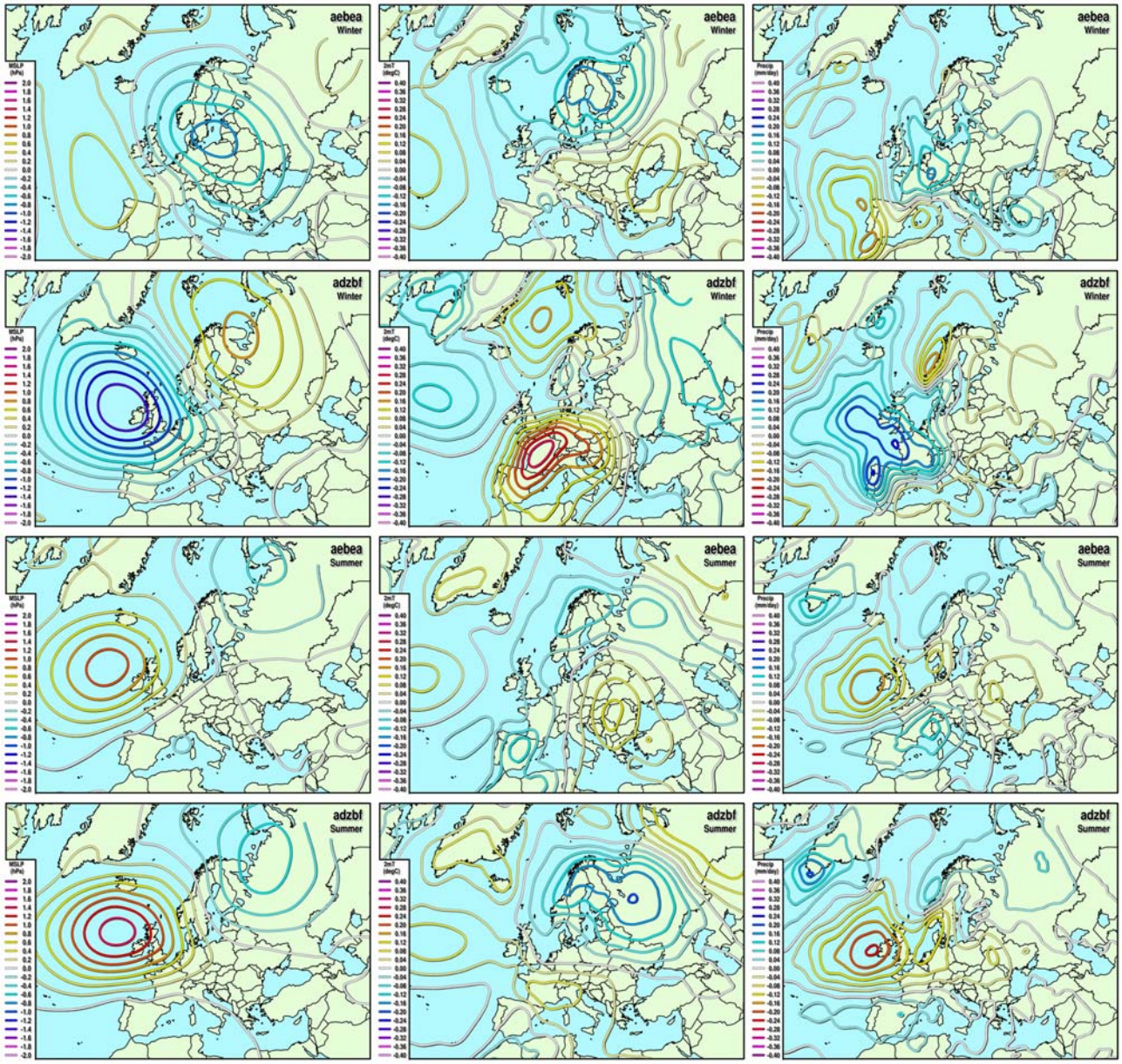

Fig. 44: Expected GWL-biases of MSLP (left), 2m-Temperature (centre) and daily precipitation (right) for HadGAM (labelled AEBEA) and HadGEM (labelled ADZBF) in the winter and summer half-years, respectively.

6.4 Tropical intraseasonal variability

6.4.1 Convectively coupled equatorial waves

(a) Dynamical and convective structures in N96 HadGAM1

Tropical convection and equatorial waves and their coupled behaviours are fundamental components of the tropical climate system. In a previous study, the ability of standard (N48) and high resolution (N144) AMIP-II simulations with HadAM3 to represent convectively coupled equatorial wave modes has been studied and compared with satellite observed brightness temperature (T_b; CLAUS dataset) and ERA-15. In a more recent study (Martin et al., 2004), temporal and spatial

variability of tropical convection in HadGAM1 at N48 resolution has been investigated and compared with AVHRR OLR for 1983 summer season. It was shown that convection in both these models contains very limited variance coincident with equatorial wave modes. Although these models can simulate the dynamical aspects of equatorial waves, the coupling of these waves with convection, particularly in equatorial regions, is deficient.

In this study we will examine the variability of tropical convection and equatorial waves in the higher resolution (N96) run with HadGAM1, in comparison with observations of T_b and ERA15 data for 1992 summer.

Figure 45(a, b) shows the seasonal mean and total standard deviation of observed and modelled convection based on brightness temperature[1]. It shows that the N96 HadGAM1 gives reasonable convective field compared with observations. This is in contrast with the N48 HadGAM1 run reported on earlier, where in non-convective regions, the simulated T_b (i.e. OLR) is generally much higher than observed (Martin et al., 2004). However, Figure 45(b) shows that, similar to the earlier N48 run, the variability of the daily mean T_b is still larger than observed. However, the difference between model and observations is only about 30% of the observational value, whereas in the N48 run the difference was closer to 100%. Thus overall the simulation of the mean and total variance of the convection in HadGAM1 has improved significantly in the later versions of the model run at the higher resolution of N96.

To show the fraction of large scale variability associated with transient, propagating convection, Figures 45(c) and 45(d) show the standard deviation of T_b for westward and eastward moving components in a zonal wave number (k) and frequency (ω domain, for wavenumbers 2 to 10 and periods of 3 to 30 days. It is clear that, for both westward and eastward moving convection, the model shows a larger variability than observations, similar to that for the total standard deviation. For westward moving convection, the model gives a very similar spatial distribution to that observed with the maxima in variance lying off the equator associated with Rossby and mixed Rossby-gravity waves. However, for eastward moving convection, the modelled variability is less confined on the equator, compared with observations where the maxima are largely centred on the equator and associated with the Kelvin wave.

The organisation of convection by equatorial waves is examined further by computing the space-time spectra, averaged between 20°N and 20°S, for observed and modelled T_b (Figure 46). As described by Wheeler and Kiladis (1999) and Yang et al. (2003), once the background red spectrum is removed, it is evident that observed tropical convection is organised on preferred space and time scales which coincide with various theoretical equatorial waves modes (equatorial Rossby (R), mixed Rossby-gravity (MRG), Kelvin and inertio-gravity (IG) waves). However, as was the case with HadAM3 at standard and high resolution, the model contains very limited variability associated with equatorial Kelvin, MRG and IG waves.

Using the methodology of Yang et al. (2003), the equatorial waves in the dynamic fields of HadGAM1 have been isolated and their vertical and horizontal

[1] For quantitative comparison, the model's OLR is converted to T_b using the formula $OLR=\sigma T_f^4$, where $T_f = T_b(a+bT_b)$ is the flux equivalent brightness temperature, and $a=1.228$ and $b=-1.106*10^{-3}\ K^{-1}$ (see Ohring and Gruber 1984)

structure examined. To summarise the overall wave activity at different heights within the troposphere and stratosphere, the vertical cross-section of the standard deviation of the winds associated with the various dynamical wave modes has been plotted in Figure 47 from ERA-15 and HadGAM1.

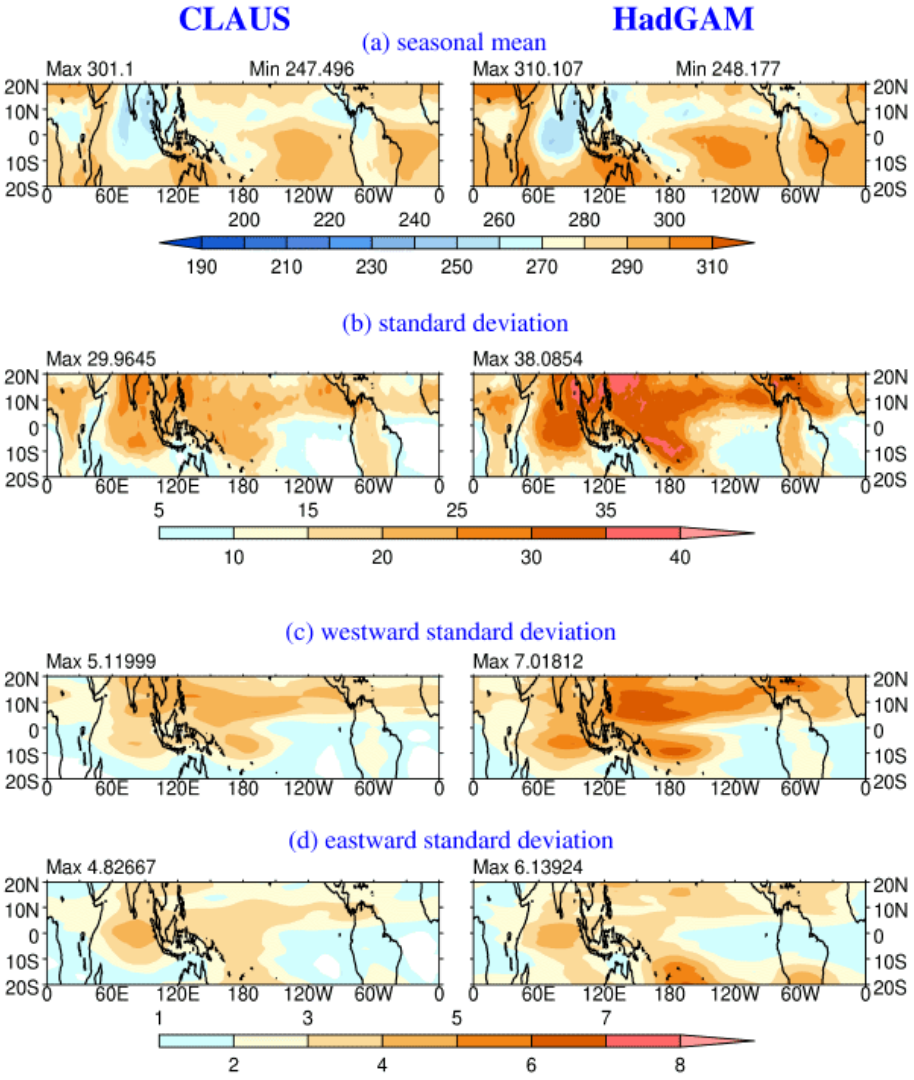

Figure 45. (a) Seasonal mean, (b) total standard deviation, (c) westward and (d) eastward moving standard deviation of observed CLAUS T_b (left panels) and HadGAM T_b (right panels) for 1992 summer (May-October). Unit is K.

The Kelvin wave is characterised by large variations in the equatorial zonal wind field, which, in the troposphere, are greatest around 150-100hPa, near the outflow level for convection (Figure 47(a)). ERA-15 also shows a secondary maximum in the lower stratosphere associated with upward propagating waves, although the vertical resolution of ERA-15 is probably not sufficient to represent these adequately[2]. The results from HadGAM1 show that the model overestimates Kelvin wave activity in the upper troposphere, especially in the Eastern Hemisphere (EH: 0-180°E), over the

[2] A study of the vertical propagation of equatorial waves with the better resolved ERA-40 dataset is currently in progress.

India Ocean. In general, the dynamical signature of the upper tropospheric Kelvin wave is stronger in the model although it appears to have little interaction with or influence on the convection (Figure 46).

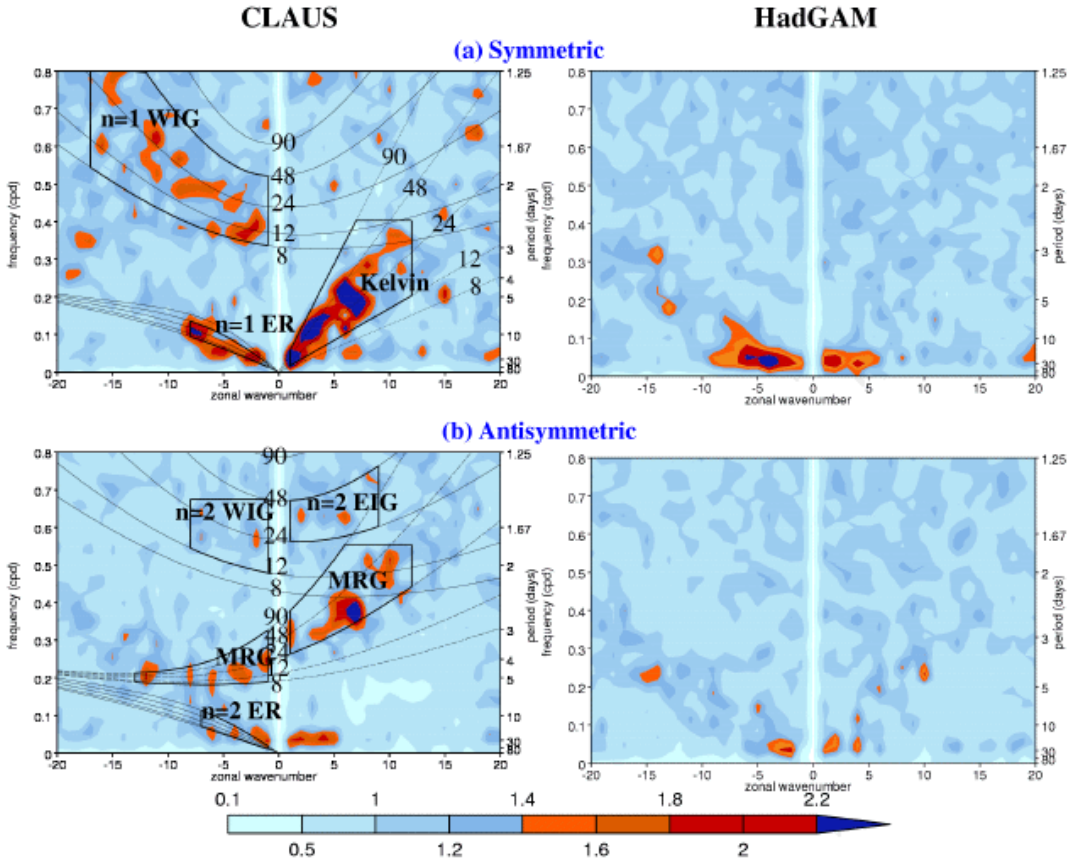

Figure 46. Zonal wavenumber-frequency power spectra divided by background power of the (a) symmetric (the odd meridional mode number *n*) and (b) antisymmetric (even n) components of CLAUS (left panels) and modelled (right panels) T_b for 1992 summer (May-October). The monthly mean has been removed from the field and the power has been averaged over the latitudes 20°N-20°S. Superimposed thin lines in left panels are the dispersion curves of the odd and even *n* equatorial waves for the equivalent depths of h=8, 12, 24, 48 and 90m. The curves have been Doppler-shifted with a 3 ms^{-1} easterly basic state.

However, using the equatorial meridional wind as a measure of WMRG wave activity, Figure 47(b) suggests that the activity of these waves is generally well simulated by HadGAM1 both in terms of geographic and vertical location. Similarly the mode 1 Rossby (R1) wave activity characterised by off-equatorial meridional wind variability (Figure 47(c)), is also reasonably well captured by the model. The enhanced wave activity within the westerly ducts over the East Pacific and Atlantic is clearly present, although, as in the WMRG wave case, the amplitude is too strong. For both the WMRG and the R1 waves, the activity is too strong over the Warm Pool in the model, and as will be shown later, may be a contributory factor in the appearance of westward propagating features at intraseasonal timescales, in the diagnosis of the MJO.

To investigate the convective patterns associated with each wave mode, the brightness temperature (T_b) field is regressed on to the lower tropospheric (850 hPa) equatorial wave modes in the eastern (i.e. convective) hemisphere. Figure 48(a)

shows the regression of T_b on to the equatorial westerly wind of the Kelvin wave. As discussed by Yang et al. (2003), the observed Kelvin wave shows a displacement of the convective maxima away from the region of maximum convergence in the lower troposphere (expected from theory), towards the region of maximum wind. In a westerly basic state this coincides with the westerly wind anomaly of the Kelvin wave (see Figure 48(a). However, in HadGAM1, the convective coupling for the Kelvin wave is not consistent with observations (Fig.48a). The convection is weak and is located near the convergence maximum instead of in phase with the equatorial westerly wind, as shown in observation. Also the spatial structure of the convective field is not well simulated by the model.

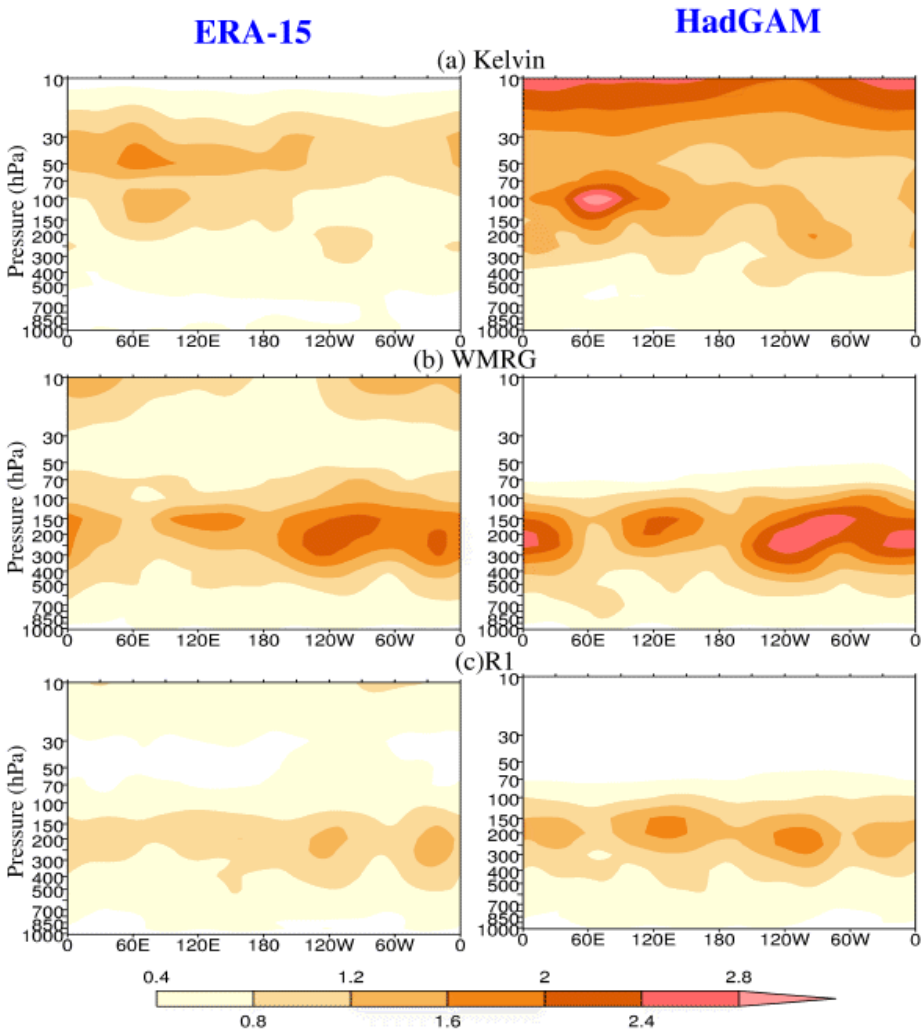

Figure 47. 17-level standard deviation of (a) equatorial zonal wind *u* of the Kelvin wave, (b) equatorial meridional wind *v* of the WMRG wave and (c) *v* at 8.5°N of the R1 wave in 1992 summer. Unit is ms^{-1}.

On the other hand, the off-equatorial convective coupling for the WMRG and R1 waves is much more consistent with the observed coupling, and with that suggested by wave theory, in which the convection is antisymmetric (symmetric) about the equator for the WMRG (R1) wave (Fig. 48 (b, c)). The model tends to have a slightly stronger convective signal in the winter (southern) hemisphere in the model, but the wavelength and downstream development is reasonably well captured, particularly for the R1 wave.

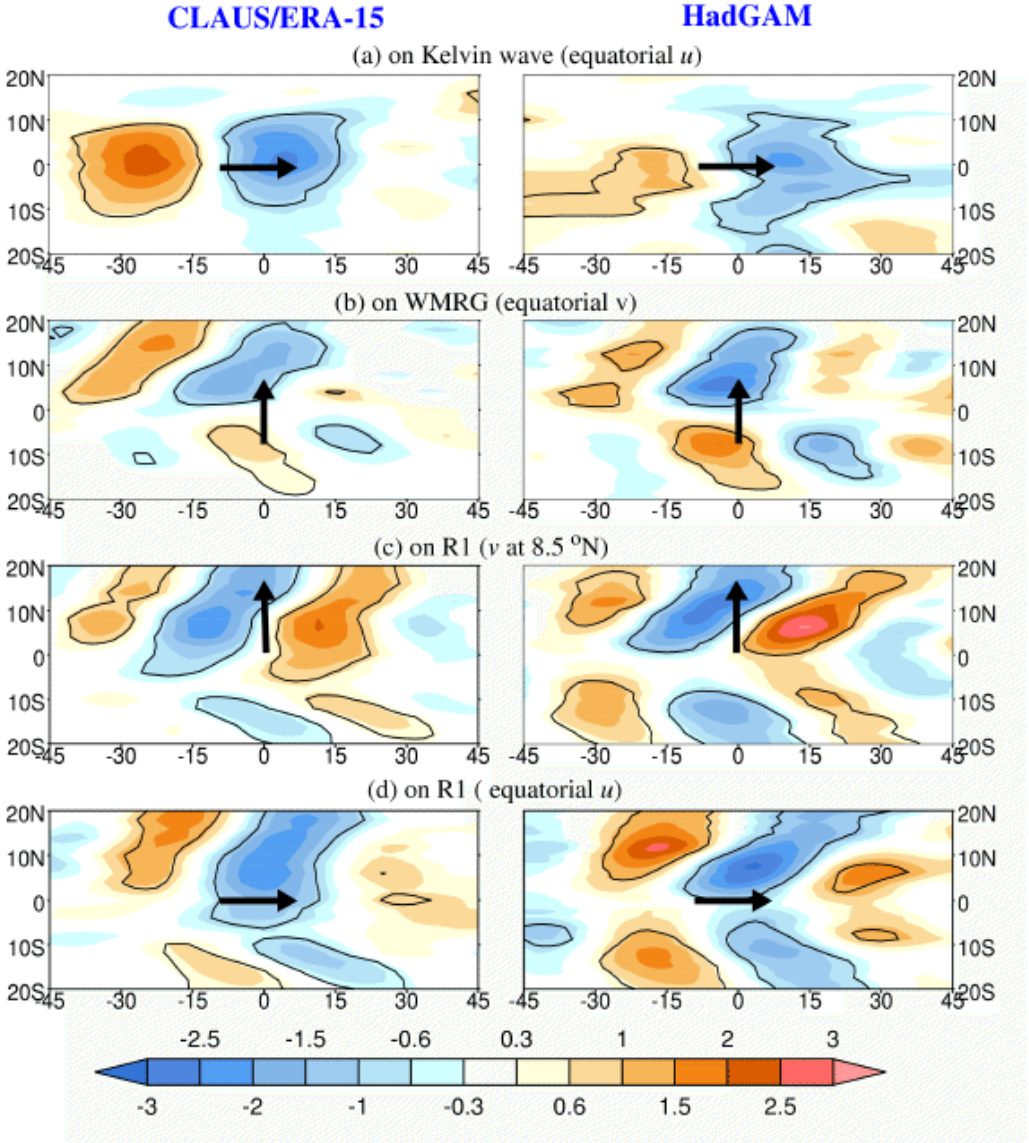

Figure 48. T_b field regressed on 850 hPa waves in the EH for (a) equatorial zonal wind *u* of the Kelvin wave, (b) equatorial meridional wind *v* of the WMRG wave, (c) *v* at 8.5°N of the R1 wave and (d) equatorial *u* of the R1 wave in 1992 summer. Black lines denote T_b exceeding 95% significant level. Arrows schematically show *u* or *v* of waves, with regression value taken to be 1.5 times of the wind standard deviation peak in the hemisphere

A key feature of observed convectively coupled waves, noted by Yang et al. (2003), is the tendency for equatorial convection to be associated with the R1 wave. Yang et al. concluded that this was a positive feedback process between the equatorial zonal winds of the R1 wave, enhanced latent heat fluxes and convection. Figure 48(d) shows the observed relationship between equatorial convection and the R1 wave. As with the Kelvin wave (Figure 48(a)), this association is only weakly evident in the simulated fields, suggesting that the observed mechanism, in which surface energy fluxes play an important role in organizing equatorial convection, is potentially missing in the model. This deserves further investigation and may provide a clue for the difficulties in simulating the coherent eastwards propagation of convection associated with the MJO.

(b) Organised convection in N96 HadGEM1

At the time of writing, no high frequency dynamical fields were available so only a preliminary assessment of the convective variability in HadGEM1 has been performed. Space-time spectral analysis of the modelled OLR in an individual summer (Figure 49) shows that convection associated with the Kelvin wave is still missing. The MJO, characterised by enhanced power at low wave-numbers and frequencies, appears to be stronger in HadGEM1 than HadGAM1 although a sample from a single summer is not sufficient to draw a firm conclusion.

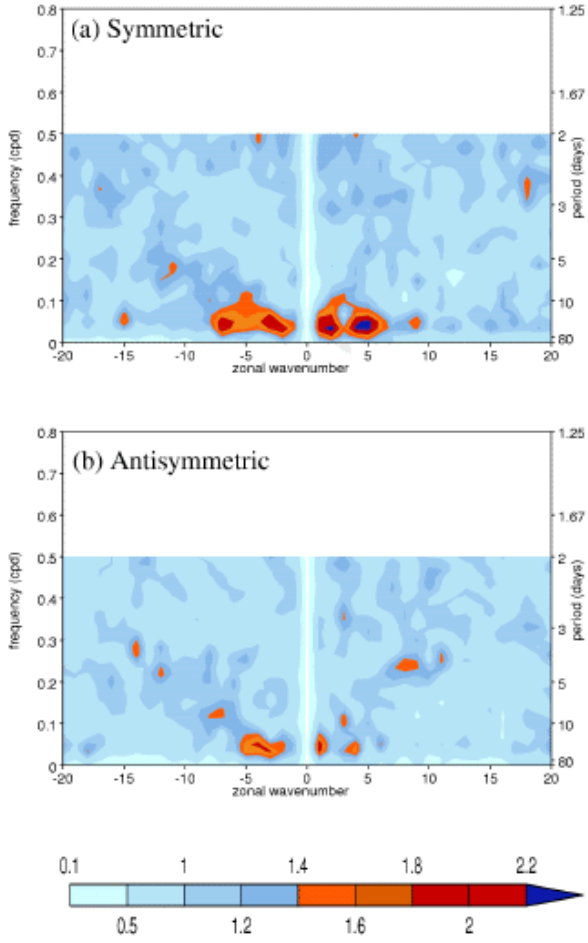

Figure 49. As in Fig.46 but for high resolution (N96) daily OLR in HadGEM run for 1972 summer.

6.4.2 The Madden-Julian Oscillation (MJO) in HadGEM1

Using 20 years of daily data from HadGEM1, a preliminary analysis of the simulated MJO, its propagation characteristics and spatial structure, has been completed. Since daily surface fluxes were not archived it has not been possible to diagnosis the role of coupled ocean-atmosphere processes in HadGEM1.

Figure 50 shows a measure of the activity of the MJO over the 20-year period compared with HadCM3. This is based on the MJO index defined by Slingo et al. (1999) using the 20-100 day filtered zonal mean zonal wind. It is clear from Figure

50 that the MJO is much more active in HadGEM1 than in HadCM3. The mean amplitude is now slightly higher than in the ERA-15 and ERA-40 data, but the model is able to capture the large interannual variability seen in the observations with notable years of strong MJO activity. Furthermore the seasonality of the MJO, being most active during northern winter and spring, is better captured in HadGEM1 than HadCM3.

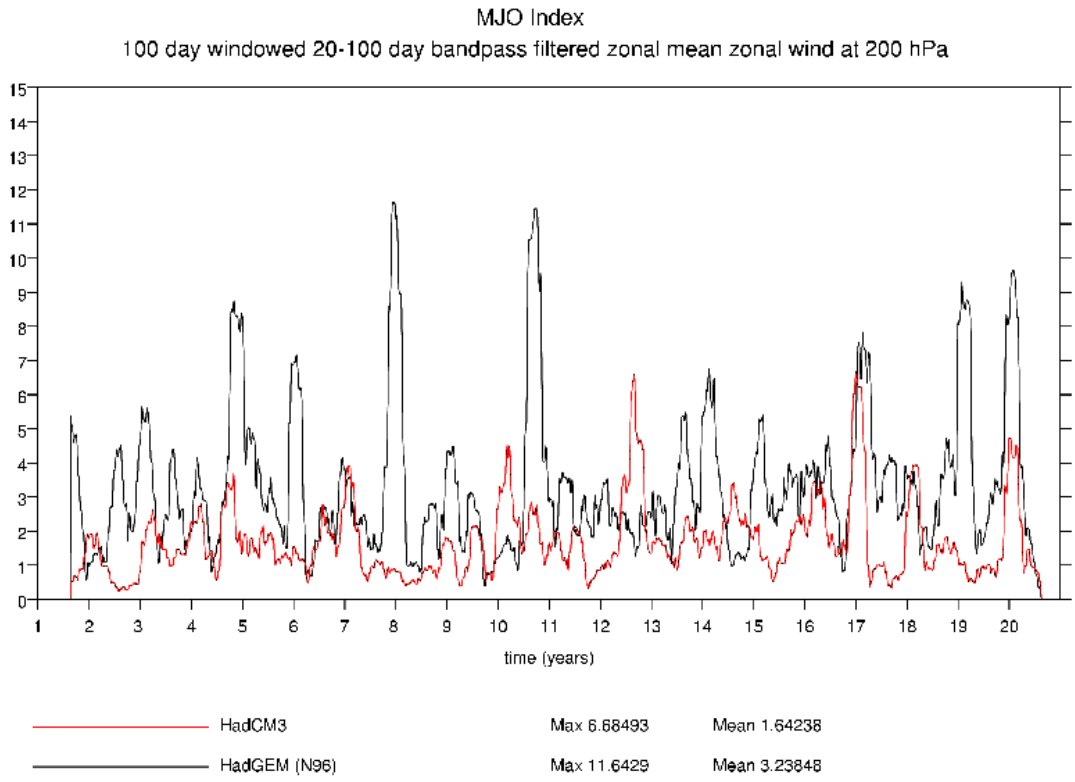

Figure 50: Interannual variability in MJO activity based on an activity index derived from the zonal mean of the upper tropospheric zonal wind.

The eastward propagation of convection associated with the MJO has been notoriously difficult to simulate in earlier versions of the model. Figure 51 shows the lag-lead correlations of OLR, along the equator between 10N and 10S, and an index of the active phase of the MJO at 90E. The observations (Figure 51(a)) show clear evidence of the propagation of convection from the Indian Ocean about 10-15 days prior to the active phase of the MJO at 90E, followed by slightly faster propagation out into the West Pacific in the subsequent 10-20 days. Figure 51(a) also shows the clear signal of suppressed convection over the Indo-Pacific warm pool 20 days before and 20 days after the enhanced convection.

As discussed by Inness and Slingo (2003), this eastward propagation was not well captured by HadCM3 (Figure 51(b)). There was only weak evidence of enhanced convection over the Indian Ocean prior to the active phase of the MJO at 90E, and the suppressed convection prior to and after the MJO is not nearly as marked as in the observations. The results from HadGEM1 (Figure 51(c)) suggest a significant improvement in the simulation of the MJO, consistent with the increased MJO activity seen in Figure 50. Although the signal of enhanced convection over the Indian Ocean is still rather weak in HadGEM1, the propagation out into the West Pacific, albeit slower than in the observations, is better simulated. Furthermore the

suppression of convection before and after the MJO active phase is more pronounced than in HadCM3. Overall, the spatial and temporal structure of the correlations between convection and MJO activity are much better captured in HadGEM1 than in HadCM3.

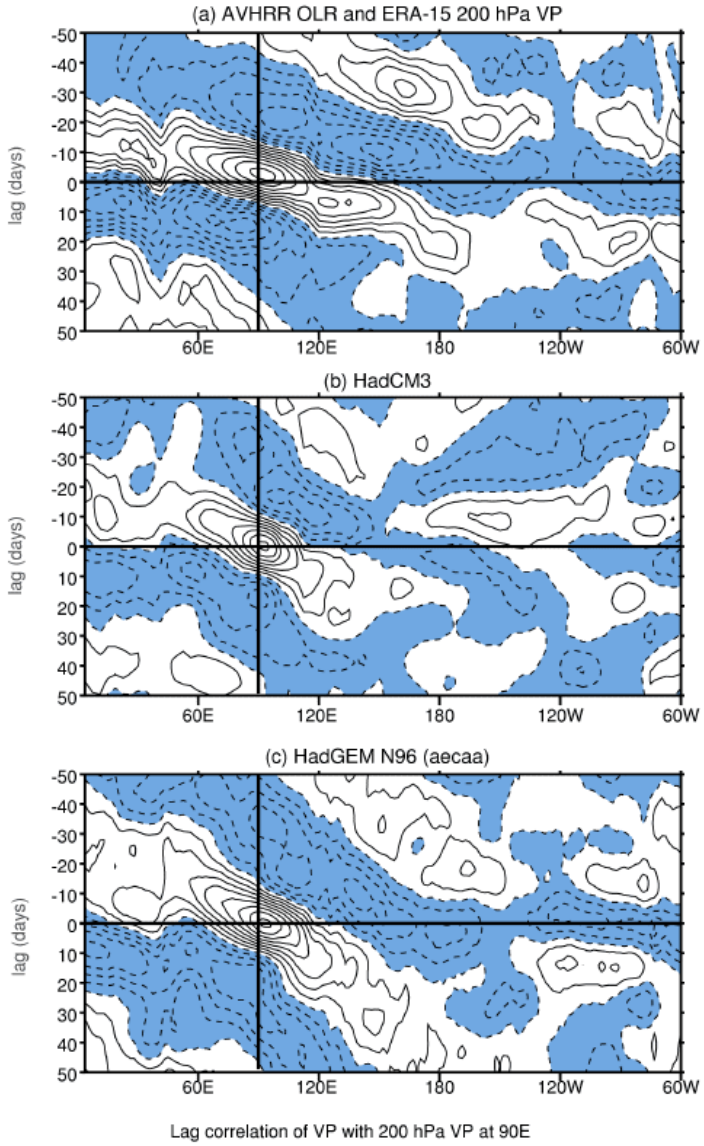

Figure 51: Lag-lead correlations of band pass filtered (20-100 day) OLR with an upper tropospheric velocity potential index defining the active phase of the MJO at 90^0E.

This impression is confirmed by looking at individual events (Fig. 52). The Hovmoller plots of 20-100 day filtered velocity potential, OLR and precipitation for the year 1874-75 are typical of this version of HadGEM1, with a couple of eastward propagating events in the OLR field that take about 60 days to get from Indian Ocean to near the dateline. These events are not particularly well coupled to the 200hPa velocity potential signal. The Hovmoller plots for 1872-73 (lower panel) show another characteristic of HadGEM1, which is westward propagating signals in the West Pacific (from Feb through to June). This type of signal was also sometimes seen in HadCM3, and was more frequent in earlier versions of HadGEM1.

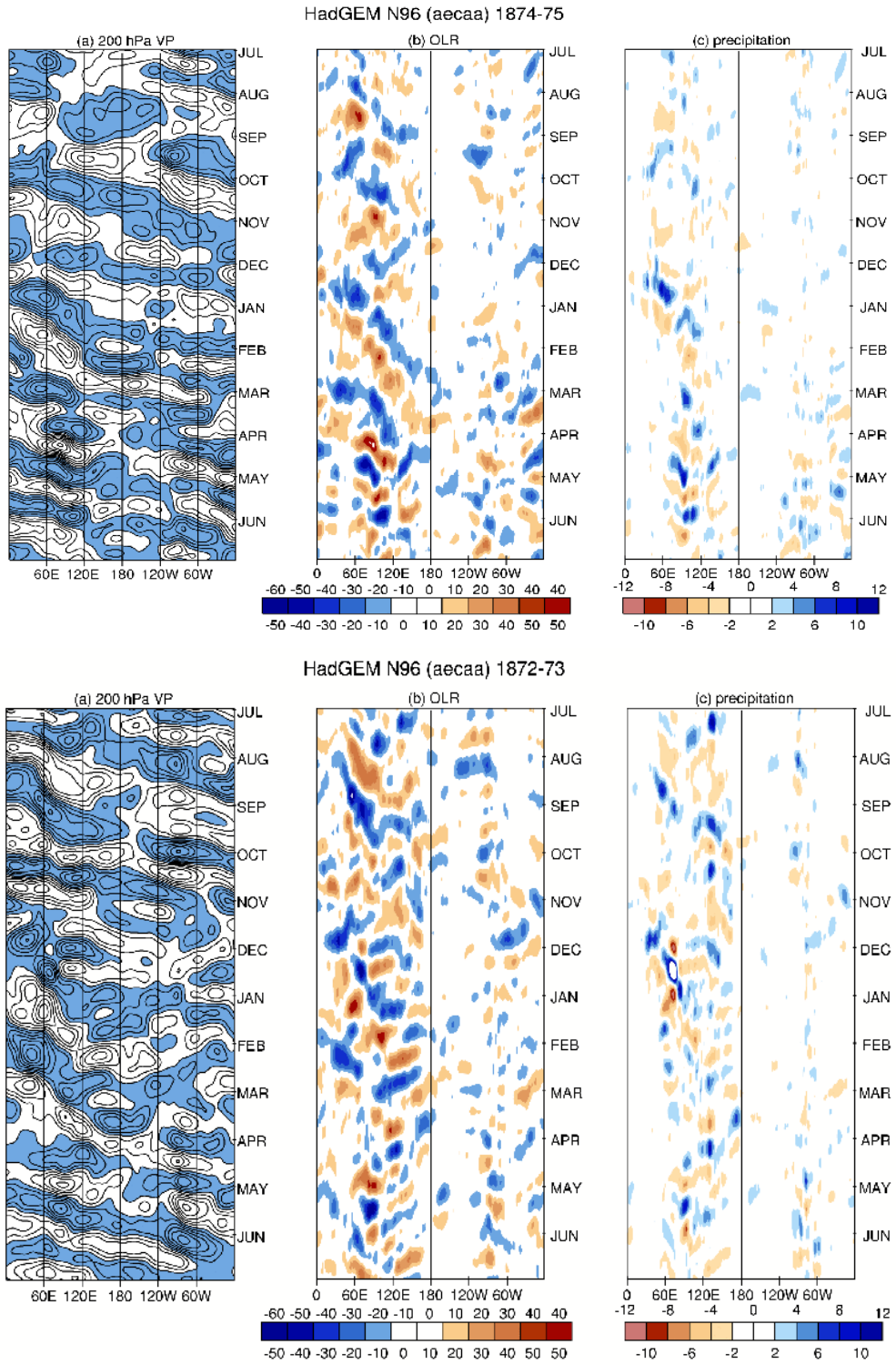

Figure 52: Example of individual MJO events from two years of HaDGEM1.

The lag-regressions of OLR and 850hPa winds on to the 200hPa velocity potential at 0N, 90E also confirm the slightly slow nature of the propagation of the MJO in HadGEM1, in comparison with HadCM3 (Figures 53 and 54). In HadGEM1, the OLR signal seems to slow down over the Maritime Continent and is only just emerging into the West Pacific on days +18 and +24. At this stage the westerly wind

burst extends through the region of enhanced convection, consistent with observations. Overall, the spatial pattern of the convection and wind anomalies associated with the eastward passage of the MJO is captured better in HadGEM1 than in HadCM3. The convective signal shows less tendency to split north and south of the equator than in HadCM3, and is about 25% stronger than in HadCM3. The zonal wind perturbations associated with the MJO are stronger in HadGEM1, particularly along the equator suggesting that there may be more stochastic forcing of El Nino by the MJO in this version of the model.

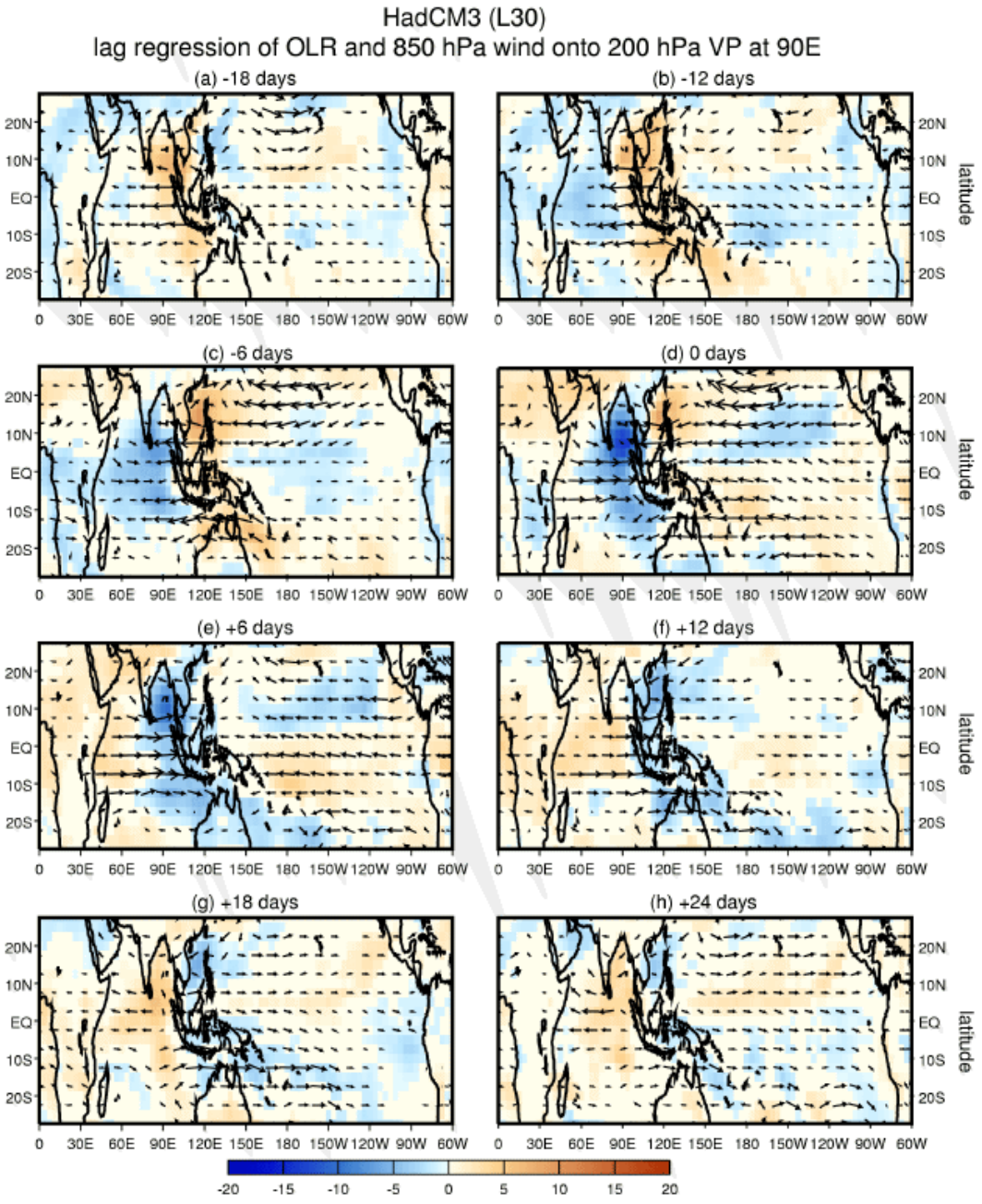

Figure 53: Evolution of the MJO in HadCM3 based on lead/lag regressions of OLR (shading) and 850hPa winds with respect to the active phase of the MJO at 90^{0}E.

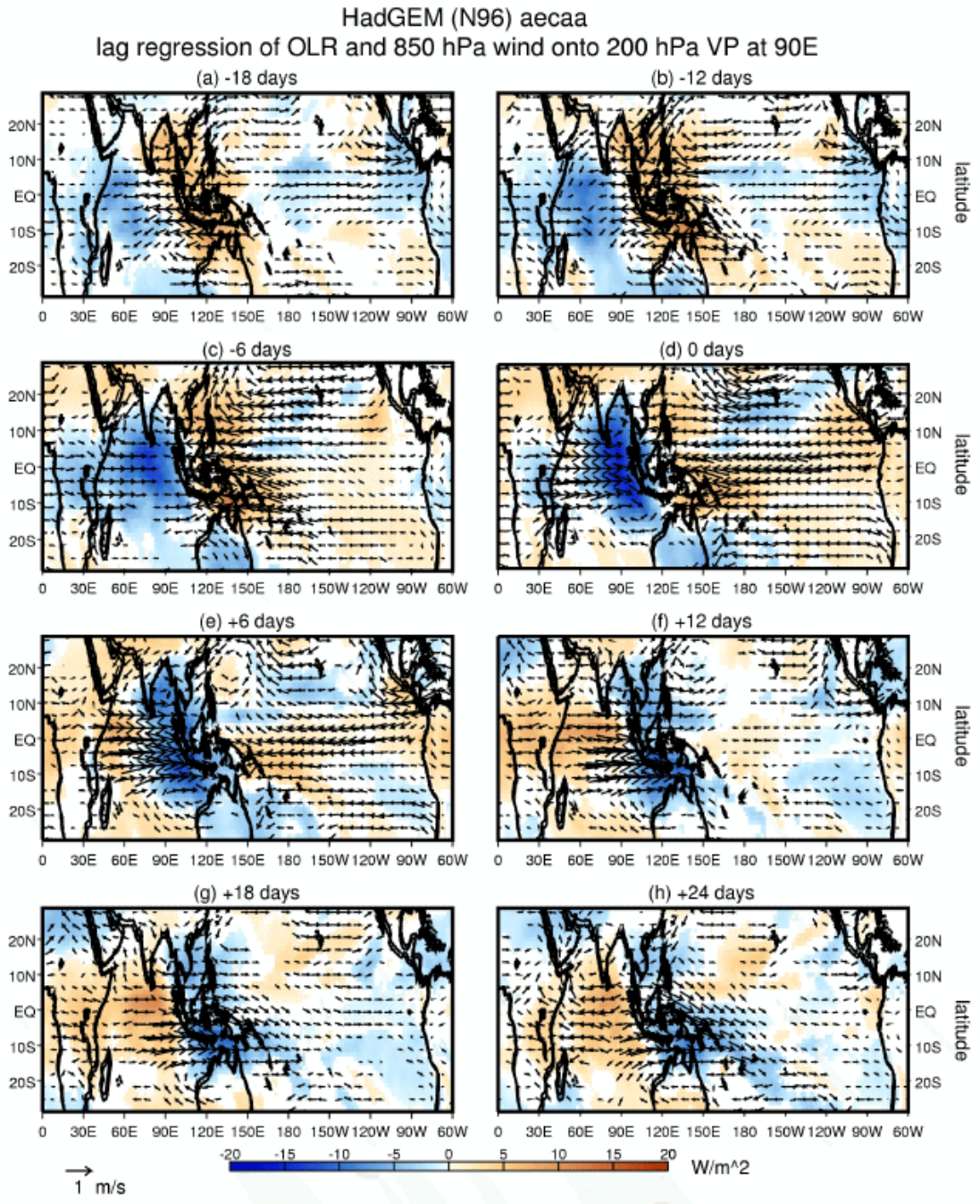

Figure 54: As Figure 53 but for HadGEM1

7. Summary and conclusions

The atmospheric component of the new Hadley Centre climate model has been evaluated against its predecessor, HadAM/CM3, and observed climatologies. The model performs well, and in many aspects it improves upon the previous version. In terms of thermodynamics, the new model is better at upper levels and worse at lower levels. The improvements at upper levels can be attributed to the increased upper-tropospheric vertical resolution and the new dynamics, as well as some of the physical improvements. The detriments at low levels are largely related to problems

in the tropics, particularly around the maritime continent. This is a notoriously difficult region to model and its effects are widespread. Work is already underway to examine the convective process in this region and to address known problems in the model's convection scheme.

In contrast with the thermodynamic variables, the winds (particularly in the tropics) are rather worse at upper levels and generally improved at lower levels. This is associated with the change to the new convection scheme in HadGAM1. The exception at low levels is in the increased bias in near-surface equatorial easterlies, particularly over the Pacific. These are associated with the development of cold equatorial SSTs in the coupled model and with deficiencies in convection over the equatorial Pacific, convection being confined to the Indonesian region. These errors are linked to an original deficiency in convection over Indonesia in the atmosphere-only model.

At N48 resolution, there is less transient eddy activity in the new model. The storm tracks are weaker (except at the surface) and the blocking frequency in the Atlantic region is reduced. This is due to the change to semi-Lagrangian dynamics, which are not designed to work well at such poor resolution. At N96 the transient eddy activity is increased and the storm tracks strengthened. Many other aspects of the simulation are also improved with increased resolution, e.g. the mean and total variance of tropical convection.

Coupling the atmosphere model to an ocean model has a small detrimental impact on the precipitation and mean sea level pressure, but has a broadly neutral impact on the other climatological fields. The impacts on precipitation are related to the development of SST errors in the tropics, particularly around the equatorial Pacific and the maritime continent. The impacts on PMSL are related to a weakening of the north Atlantic storm track, which may be related to changes in the SST distribution in that region. Both of these detriments were seen in HadCM3 compared with HadAM3. Blocking over the Pacific is reduced considerably in HadGEM1 compared with HadGAM1. This is thought to be related to the development of tropical SST and precipitation errors and the related tropical and subtropical wind errors.

Analysis of synoptic variability over Europe indicates that both HadGAM1 and HadGEM1 produce a realistic distribution of weather regimes. Some aspects of tropical intraseasonal variability are also simulated well by HadGAM/GEM1. The structure and activity of several dynamical equatorial wave modes is realistic, although like HadAM3, the new model is unable to simulate the coupling of these waves with equatorial convection. The simulation of the MJO is much improved in HadGEM1 compared with HadCM3.

There are considerable improvements in the representation of cloud in HadGAM1 compared with HadAM3. Perhaps the most significant development is the much greater consistency between the cloud and radiation budget fields in HadGAM1 – comparisons with satellite observations demonstrate that the developments included in the new model lead to a much better representation of the different ISCCP cloud types, while at the same time providing a generally more reliable simulation of the top-of-atmosphere radiation budget and the cloud radiative forcing. This leads to an improved representation of the present day climate and hopefully more reliable climate change simulations.

Acknowledgements

The development of HadGAM1/HadGEM1 represents the work of a large number of people, particularly those working in Tiger Teams, to whom the authors are indebted. Additional thanks go to Terry Davies, Nigel Wood and Adrian Lock for help in preparing this report.

References

Baur, F., Hess, P. and Nagel, H., 1944. Kalendar der Grosswetterlagen Europas 1881-1939. Bad Homburg (DWD).

Bushell, A.C. and G.M. Martin 1999. The impact of vertical resolution upon GCM simulations of marine stratocumulus. Clim. Dyn., **15**, 293-318

Cox P.M., Betts R.A., Bunton C.B., Essery R.L.H., Rowntree P.R. and Smith J., 1999. The impact of new land surface physics on the GCM simulation of climate and climate sensitivity. Clim. Dyn., **15**, 183-203.

Cullen M, 1993, The Unified forecast/climate model. Meteorol. Mag. **122**, 81-94.

Cubasch et al., 2001. Projections of future climate change. Climate Change 2001, the third assessment report of the IPCC, 525-582. Cambridge University Press, Cambridge, U.K.

Cusack, S., J. M. Edwards and J. M. Crowther, 1999a: Investigating k-distribution methods for parametrizing gaseous absorption in the Hadley Centre climate model. J. Geophys. Res., **104**, 2051-2057.

Cusack, S., J.M. Edwards and R. Kershaw 1999b: Estimating the subgrid variance of saturation, and its parametrization for use in a GCM cloud scheme. Q J R Meteorol Soc. **125**: 3057-3076

D'Andrea, F., Tibaldi, S., Blackburn, M., Boer, G., Déqué, M., Dix, M.R., Dugas, B., Ferranti, L., Iwasaki, T., Kitoh, a., Pope, V., Randall,D., Roeckner, E., Straus, D., Stern, W., den Dool, H. V., and Williamson, D. (1998). Northern Hemisphere atmospheric blocking assimulated by 15 atmospheric general circulation models in the period1979-1988. Clim. Dyn., **14:** 385-407.

Davies, T., Cullen, M.J.P., Malcolm, A.J., Mawson, M.H., Staniforth, A., White, A.A. and Wood, N. 2004. A new dynamical core for the Met Office's global and regional modelling of the atmosphere. Submitted to Q J R Meterorol Soc.

Dubal, M., Wood, N. and Staniforth, A. 2004. Analysis of parallel versus sequential splittings for time-stepping physical parameterizations. Mon. Weath. Rev., **132**, 121-132.

Edwards J M , Slingo A, 1996, Studies with a flexible new radiation code. I: choosing a configuration for a large-scale model. Q J R Meteorol Soc, **122**, 689-719.

Essery, R., M. Best and P. Cox 2001. MOSES 2.2 Technical Documentation. Hadley Centre Technical Note No. 30. Available at http://www.hadleycentre.com/research/hadleycentre/pubs/HCTN/index.html.

Gates W L, Boyle J, Covey C, Dease C, Doutriaux C, Drach R, Fiorino M, Gleckler P, Hnilo, Marlais S, Phillips T, Potter G, Santer B D, Sperber K R, Taylor K and Williams D, 1999, An overview of the results of the Atmospheric Model Intercomparison Project (AMIP). Bull. Am. Met. Soc. **80**:29-55

Gerstengabe, F.-W., Werner, P.C. and Rüge, U., 1999. Katalog der Grosswetterlagen Europas 1881-1998 nach P. Hess und H. Brezowsky. 5. Aufl. – Potsdam-Inst. F. Klimafolgenforschung, Potsdam, Germany, 138pp.

Gibson J K, Kallberg P, Uppala S, Hernandez A, Nomura A, Serrano E, 1997, ERA description. ECMWF Re-Analysis Project Series, 1.

Gordon C, Cooper C, Senior C, Banks H, Gregory J, Johns T, Mitchell J and Wood R, 2000, The simulation of SST, sea ice extents and ocean heat transports in a coupled model without flux adjustments. Clim. Dyn. **16**:147-168

Grant, A.L.M. and A.R. Brown 1999: A similarity hypothesis for shallow-cumulus transports. Q. J. Royal Meteorol. Soc., **125**: 1913-1936

Grant, A.L.M. 2001: Cloud-base fluxes in the cumulus-capped boundary layer. Q. J. Royal Meteorol. Soc., **127**: 407-421

Gregory D and Rowntree P R, 1990, A mass flux convection scheme with representation of cloud ensemble characteristics and stability dependent closure. Mon Weather Rev. **118**, 1483-1506.

Gregory D and Allen S, 1991, The effect of convective scale downdrafts upon NWP and climate simulations. Ninth conference on numerical weather prediction. Denver, Colorado, Amer Met Soc, 122-123.

Gregory D, 1995, A consistent treatment of the evaporation of rain and snow for use in large-scale models. Mon. Weath. Rev., **123**, 2716-2732.

Gregory D, Kershaw R, Inness P M , 1997, Parametrization of momentum transport by convection. II: Tests in single-column and general circulation models. Q J R Meteorol Soc **123**: 1153-1183.

Gregory D, Shutts G J and Mitchell J R, 1998, A new gravity-wave-drag scheme incorporating anisotropic orography and low-level wave breaking: Impact upon the climate of the UK Meteorological Office Unified Model. Q J R Meteorol Soc **124**, 463-494.

Gregory, J. 1999. Representation of the radiative effects of convective anvils. Hadley Centre Technical Note No. 7. Available at http://www.hadleycentre.com/research/hadleycentre/pubs/HCTN/index.html

Harrison, E.P., Minnis, P., Barkstrom B.R., Ramanathan, V., Cess, R.D. and Gibson, G.G., 1990. Seasonal variation of cloud radiative forcing derived from the Earth Radiation Budget Experiment. J. Geophys. Res., **95,** 18687-18703.

Hess, P. and Brezowsky, H., 1977. Katalog der Grosswetterlagen Europas 1881-1976, 3. verbesserte und ergänzte Aufl. Berichte des Deutschen Wetterdienstes **113**. Offenbach am Main.

Hoskins, B. and K. Hodges 2002: New perspectives on the Northern Hemisphere winter storm tracks. J. Atmos. Sci. **59**: 1041-1061

Inness, P.M. and J.M. Slingo 2003: Simulation of the Madden-Julian Oscillation in a coupled general circulation model. Part I: Comparison with observations and an atmosphere-only GCM. J. Climate **16:** 345-364

Inness P. M., J. M. Slingo, E. Guilyardi and J. Cole 2003: Simulation of the MJO in a coupled GCM. II: The role of the basic state. J. Climate, **16,** 365-382.

Johns, Tim, Chris Durman, Helene Banks, Malcolm Roberts, Alison McLaren, Jeff Ridley, Catherine Senior, Keith Williams, Ann Keen, Buwen Dong, Mark Ringer, Graham Rickard, Richard Hill, Anne Pardaens, Jason Lowe, Alejandro Bodas-Salcedo, Hilary Spencer, Sheila Stark, Yvonne Searl, 2004. HadGEM1 – Model description and analysis of preliminary experiments for the IPCC Fourth Assessment Report. Hadley Centre Technical Note No. 55. Available at http://www.hadleycentre.com/research/hadleycentre/pubs/HCTN/index.html.

Jones, A., Roberts, D. L., Woodage, M. J. and Johnson, C. E., 2001. Indirect sulphate aerosol forcing in a climate model with an interactive sulphur cycle. J. Geophys. Res., **106**, 20293-20310

Jones, A. and Roberts, D. L., 2004. An interactive DMS emissions scheme for the Unified Model. Hadley Centre Technical Note No.47, Met Office, Exeter. Available at http://www.hadleycentre.com/research/hadleycentre/pubs/HCTN/index.html

Kiehl, J.T. and, 1994. On the observed near cancellation between longwave and shortwave cloud forcing in tropical regions. J. Climate, **7,** 559-565.

Klein, S.A. and Jacob, C., 1999. Validation and sensitivities of frontal clouds simulated by the ECMWF model. Mon. Weath. Rev., **127,** 2514-2531.

Lawrence, D.M. and Slingo, J.M. 2004. An annual cycle of vegetation in a GCM. Part I: Implementation and impact on evaporation. Clim. Dyn. **22**: 87-106

Lin, W. Y., Zhang, M. H., 2004. Evaluation of clouds and their radiative effects simulated by the NCAR Community Atmospheric Model against satellite observations. J. Climate, **17,** 3302-3318.

Lock, A.P., A.R. Brown, M.R. Bush, G.M. Martin and R.N.B. Smith 2000. A new boundary layer mixing scheme. Part I: Scheme description and SCM tests. Mon. Weath. Rev., **128**: 3187-3199

Martin, G.M. and M.K. Soman 2000. Effects of changing physical parametrisation on the simulation of the Asian summer monsoon in the UK Meteorological Office Unified Model. Hadley Centre Technical Note No. 17. Available at http://www.hadleycentre.com/research/hadleycentre/pubs/HCTN/index.html.

Martin, G.M., M.R. Bush, A.R. Brown, A.P. Lock and R.N.B. Smith 2000. A new boundary layer mixing scheme. Part II: Tests in climate and mesoscale models. Mon. Weath. Rev., **128**, 3200-3217

Martin, G.M., P.M. Inness, G.-Y. Yang, B.J. Hoskins and J.M Slingo, 2004. Tropical performance of HadGAM1. Hadley Centre Technical Note No. 51. Available at http://www.hadleycentre.com/research/hadleycentre/pubs/HCTN/index.html.

Oki, T. and Y. C. Sud, 1998: Design of Total Runoff Integrating Pathways (TRIP) - A global river channel network. Earth Interactions, 2.

Pelly, J. L. (2001). The predictability of atmospheric blocking. PhD Thesis, Reading University

Pelly, J. L., Hoskins, B. J. (2003). A new perspective on blocking. J. Atmos. Sci., 60: 643-755.

Pope VD, Gallani ML, Rowntree PR and Stratton RA (2000) The impact of new physical parametrizations in the Hadley Centre climate model: HadAM3. Clim Dyn **16**: 123-146.

Pope VD, Pamment JA, Jackson DR, Slingo A (2001) The representation of water vapour and its dependence on vertical resolution in the Hadley Centre climate model. J Clim **14:** 3065-3085.

Pope, V.D. and R.A Stratton 2002: The processes governing horizontal resolution sensitivity in a climate model. Clim. Dyn. **19**: 211-236

Ringer, M.A. and Allan, R.P., 2004. Evaluating climate model simulations of tropical cloud. Tellus, 56A, 308-327.

Roberts, D. L. and Jones, A., 2004. Climate sensitivity to black carbon aerosol from fossil fuel combustion. J. Geophys. Res., 109, doi: 10.1029/2004JD004676

Rossow, W.B. and Schiffer, R.A., 1999. Advances in understanding clouds form ISCCP. Bull. Amer. Meteor. Soc., **80,** 2261-2287.

Senior C and Mitchell J F B, 1993, CO2 and climate: The impact of cloud parametrization. J. Clim. **6**: 393-418.

Smith R N B, 1990, A scheme for predicting layer clouds and their water content in a general circulation model. Q J R Meteorol Soc **116:** 435-460.

Smith R N B, 1993, Experience and developments with the layer cloud and boundary layer mixing schemes in the UK Meteorological Office Unified Model. In Proceedings of the ECMWF/GCSS workshop on parametrization of the cloud-topped boundary layer, 8-11 June 1993, ECMWF, Reading, England.

Smith, R.N.B., Gregory, D., Wilson, C.A., Bushell, A.C. and Cusack, S. 1999. Calculation of saturated specific humidity and large-scale cloud. UM Documentation Paper No. 29.

Staniforth, A., A. White, N.Wood, J. Thuburn, M.Zerroukat and E. Cordero, 2003. Joy of UM5.4 – Model Formulation. Unified Model Documentation Paper No 15.

Stratton, R.A. 1999. The impact of increasing horizontal resolution on the HadAM3 climate simulation. Hadley Centre Technical Note No. 13. Available at http://www.hadleycentre.com/research/hadleycentre/pubs/HCTN/index.html

Stratton, R.A. 2004a. The energetics of a semi-Lagrangian dynamical core. Hadley Centre Technical Note No. 52. Available at http://www.hadleycentre.com/research/hadleycentre/pubs/HCTN/index.html

Stratton, R.A. 2004b. Report on aspects of variability in high-resolution version of HadAM3. Hadley Centre Technical Note No. 53. Available at http://www.hadleycentre.com/research/hadleycentre/pubs/HCTN/index.html

Taylor, K.E., 2001: Summarizing multiple aspects of model performance in a single diagram, J. Geophys. Res., **106**, 7183--7192.

Tibaldi, S and Molteni, F, 1990, On the operational predictability of blocking. Tellus **42A:** 343-365.

Webb, M.J., Senior, C.A., Bony, S. and Morcrette, J.-J., 2001. Combining ERBE and ISCCP data to assess clouds in the Hadley Centre, ECMWF and LMD atmospheric models. Clim. Dyn., **17,** 905-922.

Webster, S., Brown, A.R., Cameron, D.R., Jones, C.P., 2003. Improvements to the representation of orography in the Met Office Unified Model. Q. J. R. Meteorol. Soc. **129**: 1989-2010

Wilson, D.R. and S.P. Ballard, 1999: A microphysically based precipitation scheme for the Met Office Unified Model. Q. J. R. Meteorol. Soc., **125,** 1607-1636

Woodage, M., Davison, P. and Roberts, D. L., 2003. Aerosol processes. Unified Model documentation paper No. 20.

Yang, G. Y, B. Hoskins, and J. Slingo, 2003: Convectively coupled equatorial waves: A new methodology for identifying wave structures in observational data. J. Atmos. Sci., **60**, 1637-1654.

Yang, G. Y, B. Hoskins, and J. Slingo, 2004: Convectively coupled equatorial waves. Part I: Horizontal structure. To be submitted to J. Atmos. Sci.

Yang, G. Y, B. Hoskins, and J. Slingo, 2004: Convectively coupled equatorial waves. Part II: Zonal propagation. To be submitted to J. Atmos. Sci.

Yang, G. Y, B. Hoskins, and J. Slingo, 2004: Convectively coupled equatorial waves. Part III: Vertical structure. To be submitted to J. Atmos. Sci.